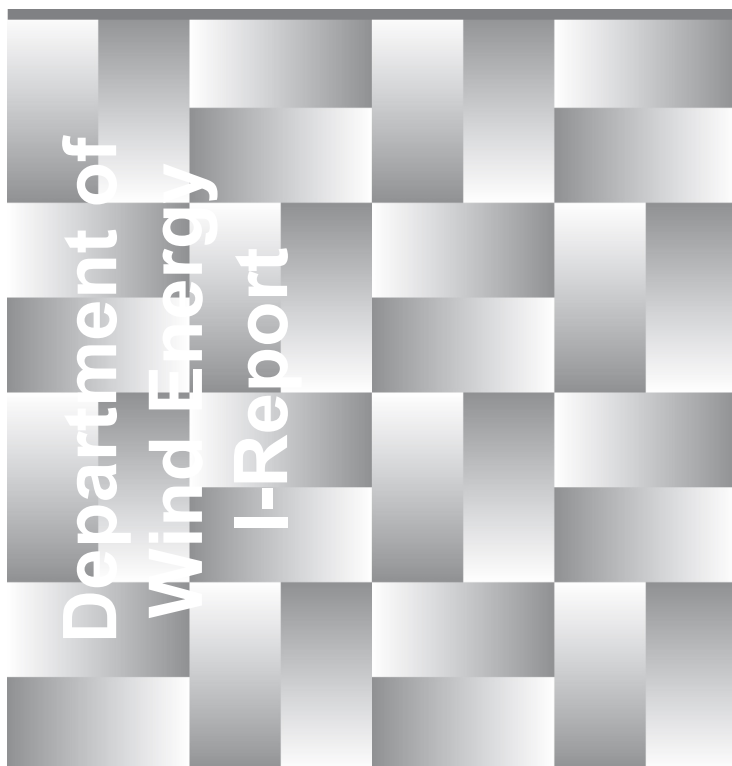


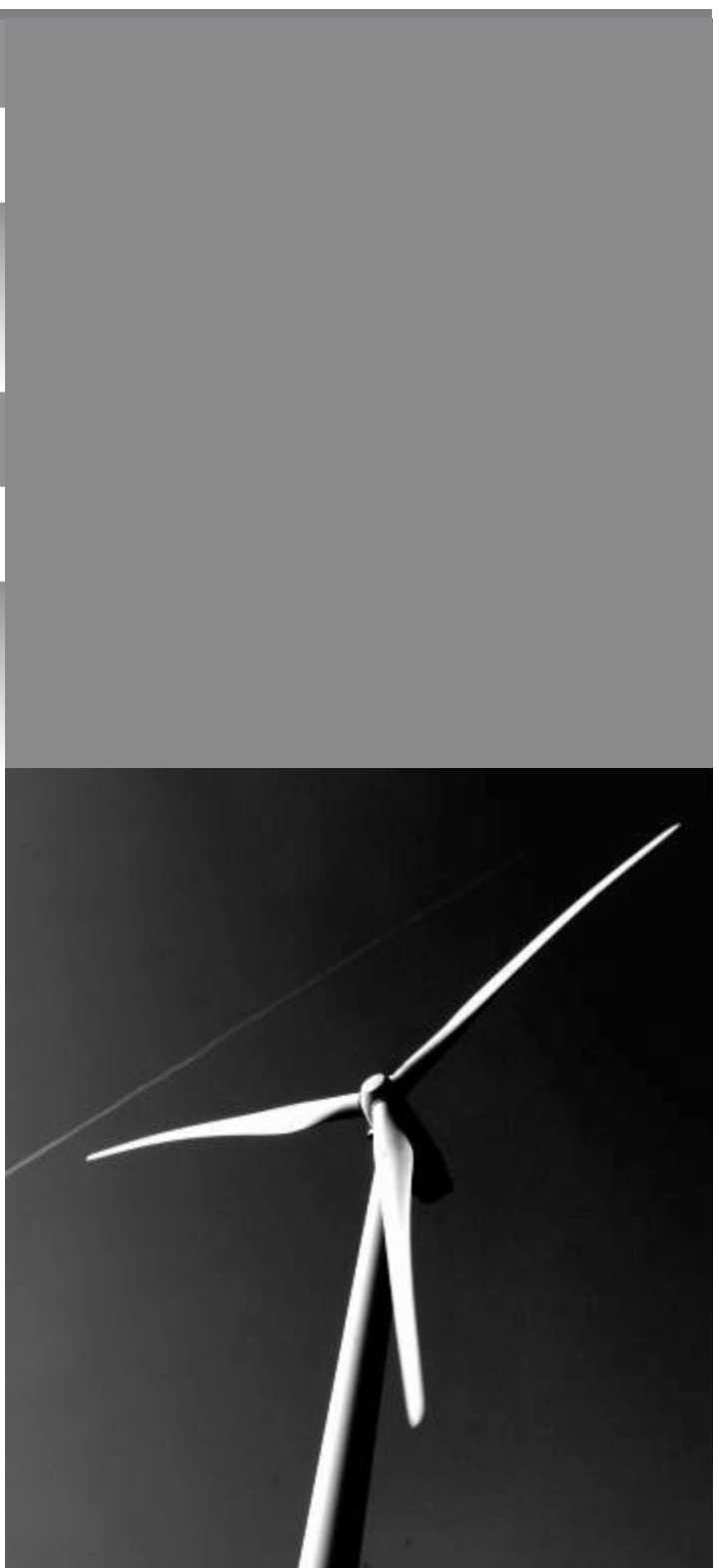
# Description of the DTU 10 MW Reference Wind Turbine



Christian Bak, Frederik Zahle, Robert Bitsche, Taeseong Kim, Anders Yde, Lars Christian Henriksen, Anand Natarajan, Morten Hartvig Hansen

DTU Wind Energy Report-I-0092

July 2013





**Author(s):** Christian Bak, Frederik Zahle, Robert Bitsche, Taeseong Kim, Anders Yde, Lars C. Henriksen, Anand Natarajan, Morten Hansen  
**Title:** Description of the DTU 10 MW Reference Wind Turbine  
**Institute:** DTU Wind Energy

**Summary (max. 2000 char.):**

This report describes the DTU 10-MW Reference Wind Turbine. The aerodynamics, the structural layout, the control and the aeroelastic characteristics are described in detail. All data required to reproduce the computations are also available in electronic form.

**Report Number:** DTU Wind Energy Report-I-0092  
**Publication Date:** July 2013

**Sponsorship:** EUDP 2010-I

**Pages:** 138  
**Tables:** 69  
**Figures:** 62  
**References:** 41

Technical University of Denmark  
DTU Wind Energy  
Frederiksborgvej 399  
4000 Roskilde  
Denmark  
Telephone +45 4677 5085



# Contents

<b>1. Introduction</b>	<b>7</b>
1.1. How to Refer to the DTU 10MW RWT . . . . .	9
1.2. Data Repository . . . . .	9
1.3. Version Handling . . . . .	10
<b>2. Overall Dimensions</b>	<b>11</b>
2.1. Upscaling Procedure . . . . .	11
2.2. The DTU 10MW RWT Key Parameters . . . . .	12
<b>3. Aerodynamic Design</b>	<b>15</b>
3.1. Airfoil Selection . . . . .	15
3.1.1. Airfoil Geometry . . . . .	15
3.1.2. Airfoil Aerodynamic Characteristics . . . . .	15
3.2. Rotor Design . . . . .	20
3.3. Aerodynamic Performance of the Rotor Using BEM . . . . .	23
3.4. 3D Blade Geometry . . . . .	23
3.5. Aerodynamic Steady State Performance . . . . .	29
3.5.1. HAWCStab2 Simulation Setup . . . . .	30
3.5.2. 3D CFD Simulation Setup . . . . .	30
3.5.3. Operational Parameters . . . . .	30
3.5.4. Results . . . . .	32
<b>4. Structural Design</b>	<b>37</b>
4.1. Structural Design of the Blade . . . . .	37
4.1.1. Material Parameters . . . . .	37
4.1.2. Blade Internal Structure and Composite Layup Definition . . . . .	42
4.1.3. Cross Section Stiffness and Mass Properties . . . . .	47
4.1.4. Strength Analysis . . . . .	53
4.1.5. Buckling Analysis . . . . .	55
4.2. Structural Design of the Tower . . . . .	57
4.2.1. Material Parameters . . . . .	57
4.2.2. Geometry and Material Thickness . . . . .	59
4.2.3. Cross Section Stiffness and Mass Properties . . . . .	59
4.2.4. Loads and Boundary Conditions . . . . .	60
4.2.5. Strength Analysis . . . . .	61
4.2.6. Buckling Analysis . . . . .	62
<b>5. Control</b>	<b>63</b>

<b>6. Aero-Servo-Elastic Design</b>	<b>65</b>
6.1. Introduction . . . . .	65
6.2. Description and Characteristics of the Components . . . . .	65
6.2.1. Nacelle and Hub . . . . .	65
6.2.2. Drivetrain Properties . . . . .	66
6.2.3. Tower . . . . .	67
6.3. Description of Design Load Cases . . . . .	67
6.4. Aeroelastic Results . . . . .	68
6.4.1. Eigenvalue Analyses . . . . .	68
6.4.2. Statistic Analyses . . . . .	68
6.4.3. Ultimate Load Analyses . . . . .	71
6.4.4. Fatigue Load Analyses . . . . .	71
6.4.5. Tower Clearance . . . . .	74
6.4.6. Vibration Issue . . . . .	76
6.4.7. Stability Investigation for Run-Away Situation . . . . .	82
<b>7. Conclusions</b>	<b>85</b>
<b>A. Cubic Splines Defining Blade Properties</b>	<b>93</b>
<b>B. Geometry</b>	<b>101</b>
<b>C. CFD Data</b>	<b>103</b>
C.1. 2D CFD Data . . . . .	103
C.2. 3D CFD Data . . . . .	103
<b>D. Load Cases</b>	<b>107</b>
<b>E. Extreme loads</b>	<b>111</b>

# 1. Introduction

From the late 1970's until now there has been a continuous upscaling of wind turbines. Upscaling causes a challenge because the mass of the turbine increases with the cube of the rotor radius with linear upscaling. The largest wind turbines on the market or on the way to the market are in the order of 7 MW. However, increasing the size further will be even more challenging.

To address this challenge, the Light Rotor project has been initiated as a cooperation between DTU Wind Energy and Vestas, where the main objective is to optimize the design of the blades to increase the stiffness and overall performance of the rotor taking into account both aerodynamic, aero-servo-elastic and structural considerations. Thus, new airfoils and new aero-servo-elastic and structural methods are developed in the project. A very important activity in the project is to use a system approach in the overall design process, which includes further development of the existing tools within numerical optimization to establish an advanced design complex.

As part of the Light Rotor project a 10-MW reference rotor is designed, so that future designs can be compared to the rotor, also called the DTU 10-MW Reference Rotor. Even though the focus in the project is the rotor design, the existence of the entire wind turbine is needed to understand the rotor performance in its interaction with the entire system including the structural dynamics of the blades, the tower and the drive train. That is the reason to establish an entirely new wind turbine, the DTU 10-MW Reference Wind Turbine (DTU 10MW RWT). This turbine is used to reveal the performance of the blade and is inspired by the artificial NREL 5 MW reference wind turbine [1]. Even though new methods are developed in the Light Rotor project the methods used for designing the DTU 10MW RWT were the existing ones following a sequential workflow to also reveal the effect of using updated methods in the rotor design process later in the project. Thus, the blade weight was minimized using existing methods, but no new concepts or materials were used. Therefore, a significant reduction in rotor mass was not expected compared to existing upscaled rotors.

At the kick-off meeting for the big EU project INNWIND.EU it was clear that a 10 MW wind turbine was needed to test simulation models. Therefore, it was decided to use the DTU 10MW RWT as the initial reference in this project, because it was an offshore wind turbine and had a rather traditional design.

This report contains a description of the complete aerodynamic and aeroelastic model for the DTU 10MW RWT. An upscaling to obtain a light weight rotor is managed by increasing the thickness to chord ratio of airfoils along the blade span and adjusting the thickness of load carrying structural elements in the blade, rather than just keeping relative thicknesses and adjusting the thickness of load carrying elements. The impact of increasing the thickness ratio along the blade is that the weight and edgewise loads scale better with

the flapwise loads while considering the negative impact from higher thickness ratio on power and thrust.

In the design process there were several iterations. In general the process was as follows:

- Aerodynamic design
- Structural design
- Load calculations using an aeroelastic tool

This procedure was run through at least three times, where e.g. the entire aerodynamic planform was changed, the aerodynamic characteristics were adjusted, the structural layup was changed or the aeroelastic setup was adjusted.

The objectives of the DTU 10MW RWT are to:

- have a basis for design of new and optimized rotors,
- show the result of a traditional, sequential design process,
- have access to a traditionally designed rotor with fairly low weight,
- design the entire wind turbine with components that are publically available so that the wind turbine model can be used also by persons, institutions and companies outside the Light Rotor project,
- be able to know the decisions and assumptions in the design process such as maximum allowable strain and stress level in the blades and which load cases that were used to design the wind turbine,
- have a wind turbine description in such a detail that aerodynamic, aeroelastic and structural simulation tools can be compared.

The objectives of the DTU 10MW RWT are not to:

- design a rotor with the lowest possible weight,
- push the safety factors, material properties and manufacturing processes as much as possible to decrease the weight,
- design a wind turbine where every detail in the wind turbine is well defined, e.g. the drive train and the tower holds a very coarse description and grid codes are not defined,
- design a wind turbine that is able to be manufactured, i.e. the manufacturing processes are not considered.

Five chapters describe the entire wind turbine:

- Chapter 2 describe the overall dimensions of the wind turbine and the considerations made in the upscaling process.
- Chapter 3 describe the aerodynamic design, where the information is sufficient to create aerodynamic models based on, e.g. the Blade Element Momentum (BEM) model and Computational Fluid Dynamics (CFD).

- Chapter 4 describe the structural design, where the information is sufficient to create structural models based on, e.g. sectional descriptions and full Finite Element Models (FEM).
- Chapter 5 describes the controller, i.e. how the rotational speed and blade pitch were handled.
- Finally, Chapter 6 describe the aeroelastic design, where information is sufficient to create a full aeroelastic model including the control of the entire wind turbine.

In the end of the report there are appendices with data with a detailed description of the wind turbine.

## 1.1. How to Refer to the DTU 10MW RWT

The DTU 10MW RWT is free to use e.g. for investigations of new blade designs. When results of such investigations are published it requires a reference to a description of the DTU 10MW RWT. In this case please refer to:

*C. Bak; F. Zahle; R. Bitsche; T. Kim; A. Yde; L.C. Henriksen; P.B. Andersen; A. Natarajan, M.H. Hansen; “Design and performance of a 10 MW wind turbine”, J. Wind Energy, To be accepted.*

## 1.2. Data Repository

A comprehensive data repository accompanies this report, which contains all necessary data for modeling the DTU 10MW RWT using a variety of simulation tools. The repository contains separate packages relating to the reference geometry, aero-elastic modeling, CFD modeling, and structural modeling. The repository is accessible via the webpage <http://dtu-10mw-rwt.vindenergi.dtu.dk>. Table 1.1 provides an overview of the directories in the repository.

Directory	Description
docs	Documentation.
excel	Excel spreadsheet with general description of the turbine.
geometry	Planform and 3D surface reference geometry for the turbine.
aeroelastic_models	Data relating to aeroelastic modeling of the turbine and selected HAWC2 simulation results.
structural_models	Data for cross-sectional and 3D FEM analysis of turbine and selected simulation results.
CFD	2D airfoil and 3D surface and volume meshes for the turbine and selected simulation results.

Table 1.1.: List of the data directories in the repository.

### **1.3. Version Handling**

This report is included along with the current version of the DTU 10MW RWT. Although the fundamental design of the RWT will not be altered, should amendments or corrections be made to the design, this report will be updated such that it always reflects the current version of the DTU 10MW RWT. Table 1.2 shows the revision history of the DTU 10MW RWT starting at Version 1.0.

Version	Revision	Date	Author	Comments
1.0	-	03.07.2013	chba@dtu.dk	Version 1.0 of the DTU 10MW RWT released.

Table 1.2.: Revision history of the DTU 10 MW Reference Wind Turbine.

## 2. Overall Dimensions

Even though the Light Rotor project was focusing on the rotor design, it was important to establish a platform, where new rotor designs could be simulated and tested. Therefore, the structural design besides the blades had to be established in order to do the full aeroelastic computations to validate the design. As no existing turbine was in the size range of the DTU 10MW RWT, it was not possible to base the design on data from existing turbines as, e.g. in the description of the NREL 5MW reference turbine [1]. Though a detailed design of all of the structural components could be performed it was out of the scope of this work. Therefore it was decided to design the DTU 10MW RWT by upscaling the NREL 5MW reference turbine. The upscaling procedure was reviewed and compared to the next generation of large wind turbines that will soon enter the market. In this process it was decided to redesign some components and scale some values based on more recent turbine data.

### 2.1. Upscaling Procedure

The structural definition of DTU 10MW RWT except of the blades was obtained by upscaling the NREL 5MW reference turbine [1] applying the classical similarity rules [2]. This was based on assumptions of geometrical similarities. It means that in order to achieve twice as much power output the rotor area was doubled.

The mass,  $m$ , was scaled by:

$$sf^3 \quad (2.1)$$

and the power,  $P$ , is scaled by:

$$sf^2 \quad (2.2)$$

the length,  $L$ , is scaled linear by:

$$sf^1 \quad (2.3)$$

the 1<sup>st</sup> Mass Moment of Inertia,  $I_1$ , is scaled by:

$$sf^4 \quad (2.4)$$

the 2<sup>nd</sup> Mass Moment of Inertia,  $I_2$ , is scaled by:

$$sf^5 \quad (2.5)$$

where  $sf$  in equation 2.1 - 2.5 is the geometric scaling factor obtained by:

$$sf = \sqrt{10/5} \quad (2.6)$$

The method neglected second-order aerodynamic effects and assumed linear structural behavior, and was based on the idea that the stresses due to aerodynamic loading was invariant during upscaling, whereas loading due to weight was linearly increasing with the scaling factor. One of the weaknesses by this method was that it might lead to a higher nacelle mass than expected for very large wind turbine designs, depending on the scaled turbine. Therefore, the nacelle and hub masses and inertias were reduced in the design of the upscaled DTU 10MW RWT. This is described in detail in section 6.2.1

## 2.2. The DTU 10MW RWT Key Parameters

The wind turbine had a rated power of 10MW, was designed for offshore siting for an IEC class 1A wind climate and was in general a traditional three-bladed, upwind wind turbine. The offshore wind climate was chosen, because it was the assumptions that the very large turbines in general will be dedicated offshore sites, since transport of these constructions are a major issue.

An overall description of the wind turbine is seen in Table 2.1. In this table also data from a direct upscale of the NREL 5MW RWT is seen. Many parameters are identical, but some are not such as:

- The IEC class changed, because the DTU 10MW RWT is made for an offshore wind climate
- The hub height is lower, because a shorter tower is possible offshore
- The drivetrain concept changed from a high speed to a medium speed
- The DTU 10MW blades have prebend to ensure tower clearance

A detailed description of the complete DTU 10MW RWT can be found in the data repository in the `excel` directory.

Parameter	DTU 10MW RWT	Upscaled 5MW	NREL 5MW
Wind Regime	IEC Class 1A	I	IEC Class 1B
Rotor Orientation	Clockwise rotation - Upwind	S	S
Control	V	S	S
Cut in wind speed	4 m/s	S	S
Cut out wind speed	25 m/s	S	S
Rated wind speed	11.4 m/s	S	S
Rated power	10 MW	S	S
Number of blades	3	S	S
Rotor Diameter	178.3 m	S	S
Hub Diameter	5.6 m	4.24 m	
Hub Height	119.0 m	127.0	
Drivetrain	M	H	S
Medium Rotor Speed	6.0 rpm	4.9 rpm	
Maximum Rotor Speed	9.6 rpm	8.6 rpm	
Maximum Generator Speed	480.0 rpm	1173.7 rpm	
Gearbox Ratio	50	97	
Maximum Tip Speed	90.0 m/s	79.9 m/s	
Hub Overhang	7.1 m	S	
Shaft Tilt Angle	5.0 deg.	S	
Rotor Precone Angle	-2.5 deg.	S	
Blade Prebend	3.332 m	0.000 m	
Rotor Mass	227,962 kg	311,127 kg	
Nacelle Mass	446,036 kg	678,823 kg	
Tower Mass	628,442 kg	982,765 kg	

Table 2.1.: Key parameters of the DTU 10 MW Reference Wind Turbine compared to a direct upscale of the NREL 5 MW Reference Wind Turbine.



## 3. Aerodynamic Design

This chapter describes the aerodynamic design of the rotor for the DTU 10MW RWT. The design is based on the Blade Element Momentum (BEM) theory, where numerical optimization is used to include certain constraints. The rotor design is also evaluated using Computational Fluid Dynamics (CFD).

### 3.1. Airfoil Selection

It was decided to design a rotor that was relatively light weight. To enable this, airfoils with high relative thickness were selected to increase the moment of inertia and thereby increase the stiffness. Since the DTU 10MW RWT were to become a publically available design the airfoils also had to be publically available. Only a few thick airfoils are publically available and based on the fact that the FFA-W3-xxx airfoils [3] are frequently used in modern Mega Watt wind turbine designs and dedicated wind turbine use, this airfoil series was selected for the present design. The FFA airfoils exist in relative thickness range between 21.1% and 36.0%. To challenge the aerodynamics and increase stiffness it was decided that the minimum relative thickness should be 24.1%. Because 36.0% relative thickness is the thickest available, two more airfoils were used between 36.0% thickness and the cylinder part of the rotor. An airfoil with relative thickness of 48.0% was created as a simple multiplication of the coordinates normal to the chord of the 36.0% thick airfoil. Also, an airfoil with relative thickness of 60.0% was created as an interpolation between the 48.0% airfoil and the cylinder part.

#### 3.1.1. Airfoil Geometry

Figure 3.1 shows the FFA-W3 airfoil series. Analysis showed that the aerodynamic performance at the inner part of the blade increased significantly when using Gurney flaps. Therefore, wedge shaped Gurney flaps were added on the inner part of the blade in the range  $r/R=[0.05:0.4]$ . Airfoils with thicknesses 36.0%, 48.0% and 60.0% with Gurney flap heights of 1.27%, 2.5% and 3.5%, respectively, were thus defined based on which airfoil data was created. Refer to Appendix B for the location of the airfoil section coordinates in the repository.

#### 3.1.2. Airfoil Aerodynamic Characteristics

Although wind tunnel measurements exist for the FFA-W3 airfoil series, only data for FFA-W3-301 and FFA-W3-360 at Reynolds number,  $Re=1.6 \times 10^6$  are publically available [4]. The data needed for this rotor size was, however, at Reynolds numbers between  $Re=6 \times 10^6$

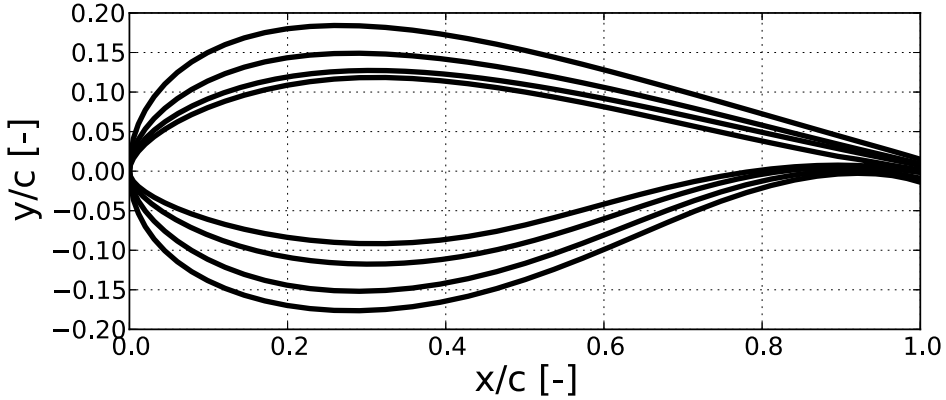


Figure 3.1.: The FFA-W3-xxx airfoil series with airfoils of relative thickness of 21.1%, 24.1%, 30.1%, and 36%.

and  $12 \times 10^6$  and therefore, it was decided to base the aerodynamic characteristics on computations.

The 2D aerodynamic airfoil characteristics were calculated using EllipSys2D [5, 6, 7] using steady state simulations. Two polars were calculated for each airfoil: one set assuming either a fully developed turbulent boundary layer on the airfoil surface with the  $k-\omega$  SST model by Menter [8], and a second set where the boundary layers were allowed to transition freely from laminar to turbulent flow using the  $\gamma-Re_\theta$  correlation based transition model of Menter et al. [9], for the present implementation see [10]. For the latter set of simulations, the turbulence intensity at the airfoil was set to 0.1%. The meshes were generated using the hyperbolic mesh generator HypGrid [11]. The meshes were O-type meshes with 512 cells around the airfoil surface and 256 cells in the normal direction. This very fine resolution was used to ensure mesh independence in the simulations assuming transition from laminar to turbulent flow, which can be more sensitive to mesh resolution than fully turbulent simulations. The height of the first cell in the boundary layer was  $5 \times 10^{-7}$  and the outer boundary was placed 40 chord length from the airfoil surface.

The Reynolds numbers were chosen with representative values for each airfoil, ranging from  $Re = 6 \times 10^6$  for the 60% chord airfoil to  $Re = 12 \times 10^6$  for the thinnest 24% chord airfoil. Figures 3.3 to 3.7 show the 2D lift and drag polars for the FFA-W3 series airfoils. The results showed a fairly small difference between the fully turbulent flow and

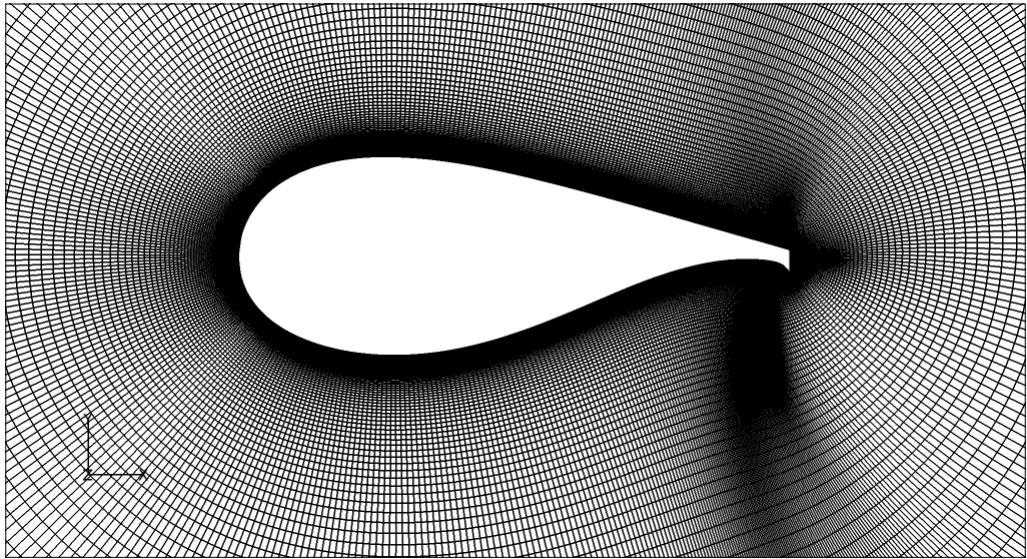


Figure 3.2.: 2D mesh around the FFA-W3-336 airfoil fitted with a Gurney flap.

flow assuming transition from laminar to turbulent flow . This stands in contrast to what was predicted by XFOIL, where a greater difference was seen between turbulent and simulations assuming transition from laminar to turbulent flow . Since no measurement data is available for this airfoil series at high Reynolds numbers, it was not possible to judge which transition model was most correct, and as such remains an open question needing further investigations. The Navier-Stokes results were chosen for the final data since this also seemed to be the most conservative choice.

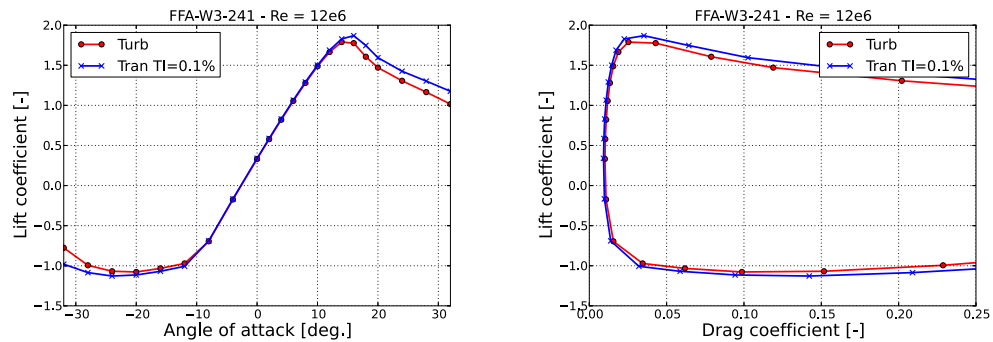


Figure 3.3.: Lift and drag polars for the FFA-W3-241 airfoil, computed using EllipSys2D assuming fully turbulent flow and transition from laminar to turbulent flow (TI=0.1%) .

For high angles of attack (AOA), i.e. for AOA in the range [-180:-45] deg and [45:180] deg, it was assumed that the airfoils respond as flat plates and therefore could be described by the following functions irrespectively of clean or contaminated surfaces:

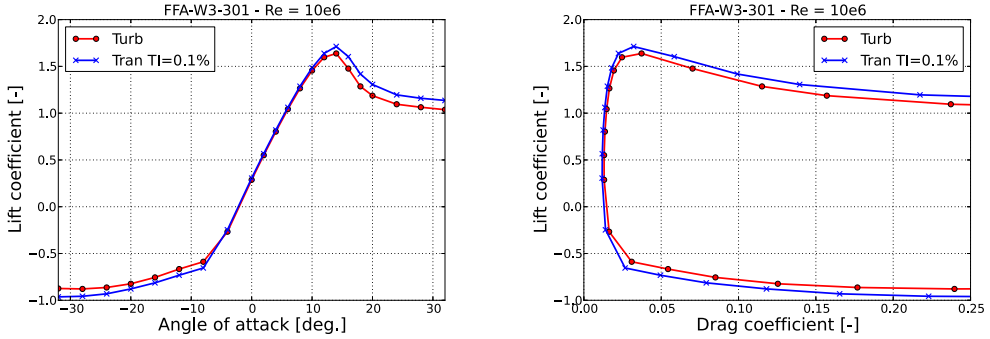


Figure 3.4.: Lift and drag polars for the FFA-W3-301 airfoil, computed using EllipSys2D assuming fully turbulent flow and transition from laminar to turbulent flow (TI=0.1%).

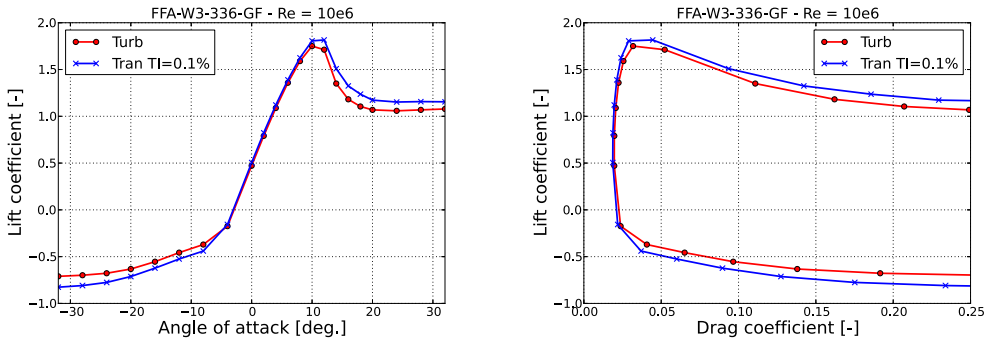


Figure 3.5.: Lift and drag polars for the FFA-W3-360 airfoil fitted with a 1.27% Gurney flap, computed using EllipSys2D assuming fully turbulent flow and transition from laminar to turbulent flow (TI=0.1%).

$$C_l = 2 \cdot \cos(AOA) \cdot \sin(AOA) \quad (3.1)$$

$$C_d = c_{d,max} \sin^2(AOA) \quad (3.2)$$

$$C_m = -\sin(AOA)/4 \quad (3.3)$$

where  $C_{d,max}$  is 1.5 at the outer part of the rotor according to [12], i.e. for the airfoil with 24% relative thickness, and 1.3 for the mid and inner part of the rotor i.e. for all other airfoils except the cylinder part.

For AOA in the range [-45:-32] and [32:45] the data was interpolated between the values at AOA=+/-32 deg that was a result of the CFD computations and the values at AOA=+/-45 deg that was a result of the flat plate assumption. This way a set of 2D airfoil characteristics were established.

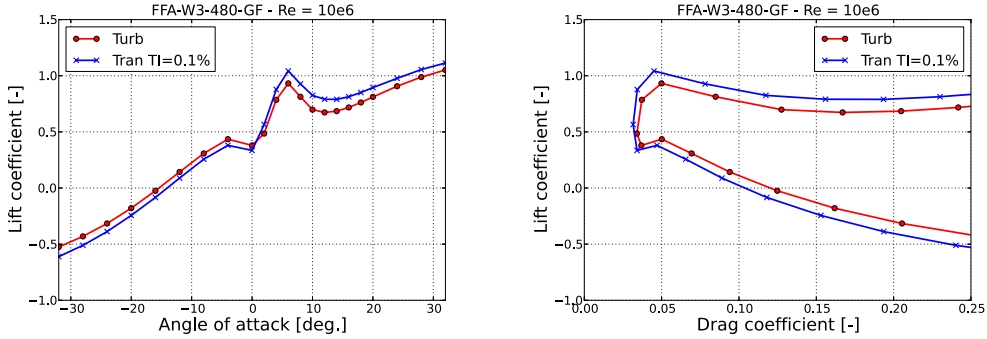


Figure 3.6.: Lift and drag polars for the FFA-W3-480 airfoil fitted with a 2.50% Gurney flap, computed using EllipSys2D assuming fully turbulent flow and transition from laminar to turbulent flow (TI=0.1%).

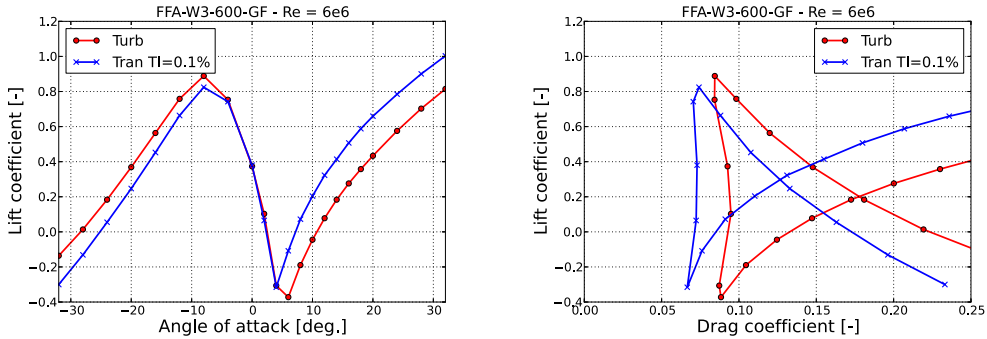


Figure 3.7.: Lift and drag polars for the FFA-W3-600 airfoil fitted with a 3.50% Gurney flap, computed using EllipSys2D assuming fully turbulent flow and transition from laminar to turbulent flow (TI=0.1%).

Based on the above 2D airfoil characteristics the data (except for the cylinder part) were 3D corrected according to Bak et al. [13]. The 3D correction was carried out in the range [0;45] deg, so to connect data in this range to the range [45;180] deg, the data points for AOA slightly larger than 45 deg were changed to avoid abrupt changes in the airfoil characteristics. Furthermore, due to the risk of instabilities [14] and based on the observations from measurements on full scale rotors [15] the airfoil characteristics from maximum lift to AOA=45 deg and from AOA=-45 deg to minimum lift were inspected for sudden changes, i.e. high values of  $d(C_l)/d(AOA)$ ,  $d(C_d)/d(AOA)$ ,  $d^2(C_l)/d(AOA)^2$  and  $d^2(C_d)/d(AOA)^2$ . This lead to small manual adjustments in both  $C_l$  and  $C_d$  for almost all the airfoil thicknesses.

The final set of airfoil characteristics is shown in Figures 3.8 to 3.10. The airfoil data can be found in Appendix C.1.

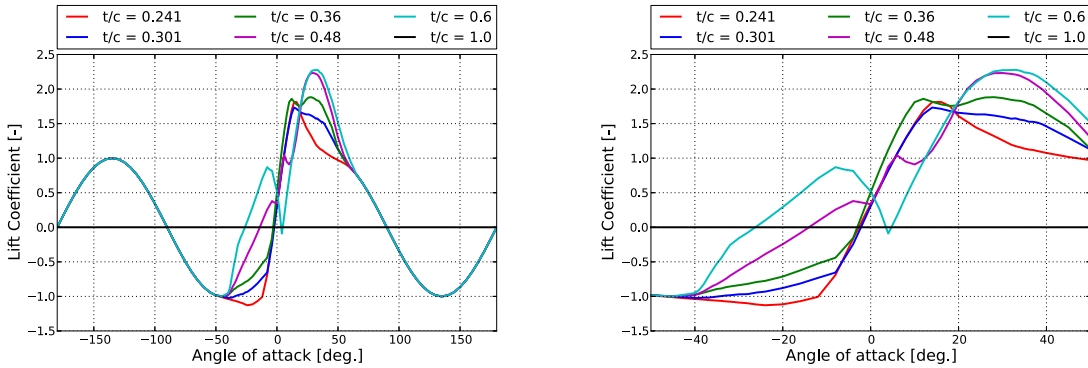


Figure 3.8.: 3D corrected lift coefficient as function of angle of attack for the six airfoil thicknesses defined for the DTU 10MW RWT.

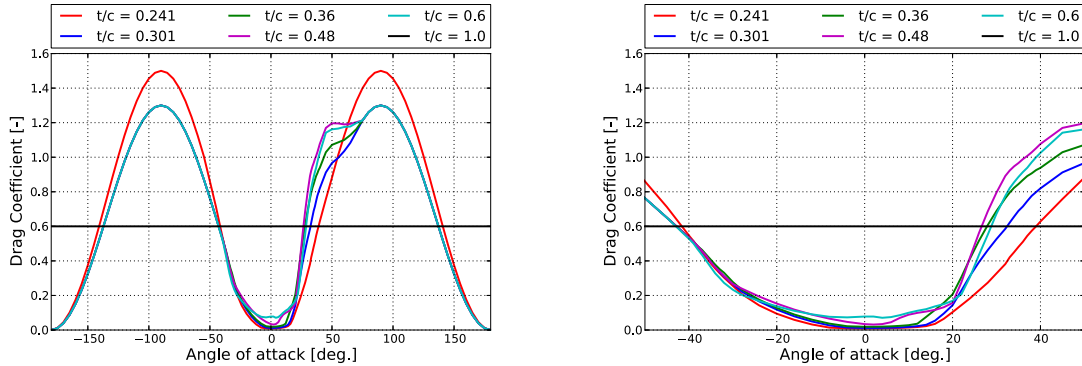


Figure 3.9.: 3D corrected drag coefficient as function of angle of attack for the six airfoil thicknesses defined for the DTU 10MW RWT.

### 3.2. Rotor Design

To carry out the rotor design, several decisions need to be taken to set up constraints in the process. The basis for the wind turbine design in general was a direct upscale of the NREL-5MW-RWT [1]. However, many dimensions changed for the final DTU 10MW RWT design. In the design process the aerodynamic design of the rotor was carried out using HAWTOPT[16]. This computational tool is based on the BEM model and numerical optimization, where the optimizer minimize an objective function with respect to certain constraints by moving chosen design variables.

The constraints were:

- The rotor radius was 89.166 m. This was an upscale of the NREL-5MW-RWT.

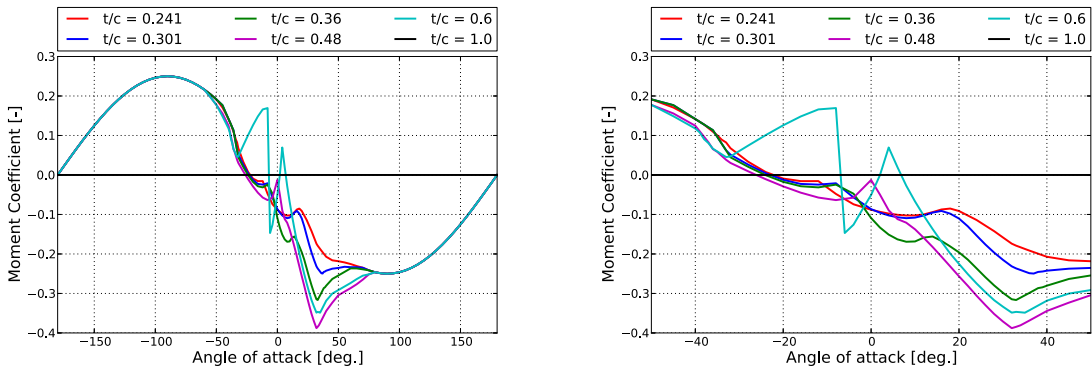


Figure 3.10.: 3D corrected moment coefficient as function of angle of attack for the six airfoil thicknesses defined for the DTU 10MW RWT.

- The relative thickness was minimum 24.1%. This thickness was rather high, but was chosen to challenge the aerodynamics, because high stiffness is needed for the large rotors.
- The absolute thickness of the root part up to radius of 10m was 5.38m. This was slightly larger than an upscale from the NREL-5MW-RWT and was chosen to add stiffness to the blade.
- The absolute thickness for the rest of the blade relative to the blade size was also larger than the NREL-5MW-RWT to add stiffness to the blade. The absolute thickness distribution was smoother than for the NREL-5MW-RWT, so at some radial positions the thickness was similar and at others it was much thicker (greater than 20%).
- The curvature of the twist should not change sign. This was to decrease the structural complexity.
- The mean thrust force at 11m/s at normal operation was maximum 1500kN, which was chosen to reduce the loads in normal operation.
- The mean thrust force at stand still at a wind speed of 50 m/s was maximum 2080kN to reduce the loads. This corresponded to a maximum chord of approximately 6 m and this chord was also chosen to challenge the aerodynamics.

The design variables were:

- chord at 14 different radii
- twist at 13 different radii
- relative thickness at 13 different radii

where Bezier curves were used as shape functions.

The objective function was the power coefficient,  $C_P$ , that with negative sign was minimized at the design tip speed ratios, TSR's, 7.00, 7.50 and 8.06. An analysis of the three designs showed that maximum  $C_P$  was found at TSR=7.5. Many issues need to be considered when choosing TSR such as power efficiency, shaft torque, noise and how slender the blade was allowed to be according to the structural stiffness. Since each of these issues points towards either low, medium or high TSR, the final design was a compromise between the different issues.

It was chosen to proceed with a blade based on TSR=7.5, which also correspond to the maximum power coefficient.

The resulting planform is shown in Figure 3.11. The plots shows that the planform was rather conventional with a traditional chord distribution with the maximum chord around a normalized radius of  $r/R=0.27$ . Less traditional was the rather large relative thickness of minimum 24.1% also at the very tip of the blade and the twist that commonly will go to zero at the tip.

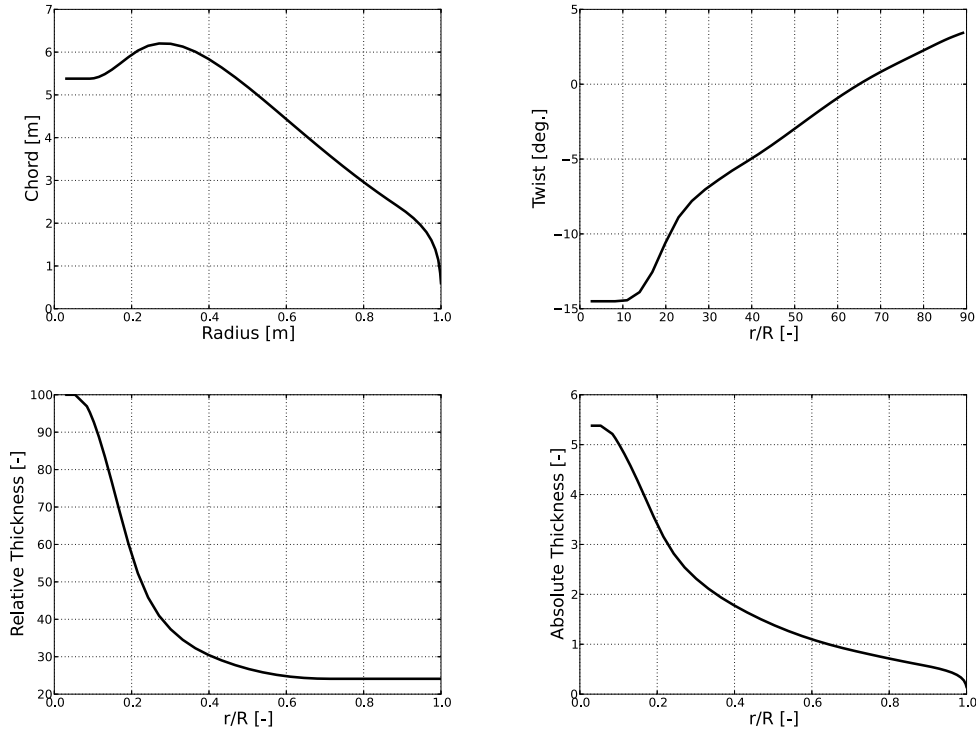


Figure 3.11.: The DTU 10 MW RWT blade planform parameters vs normalized blade span. Note that the twist is defined positive nose up in order to conform to the right-handed coordinate system used to build the 3D blade shape.

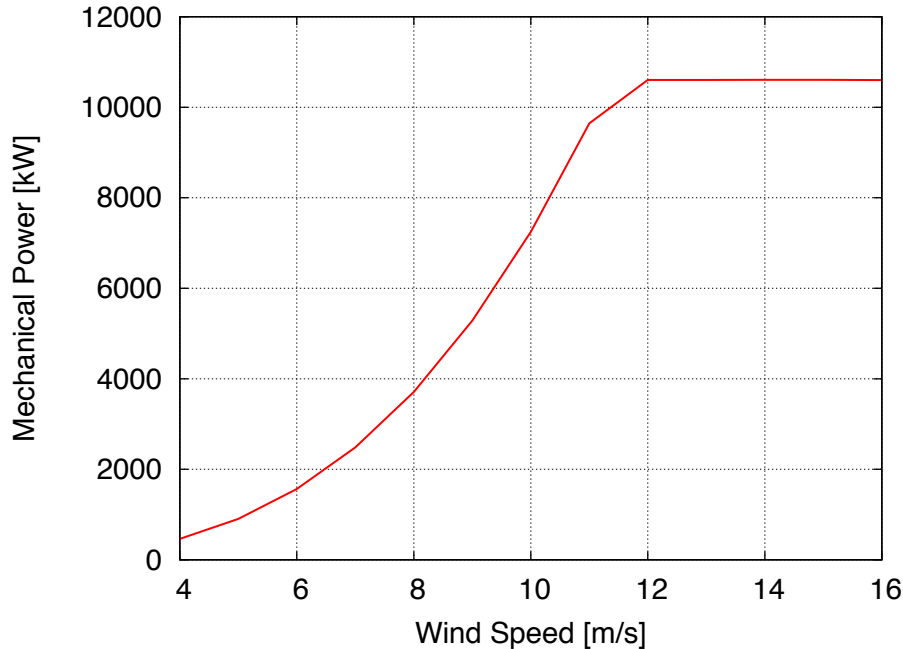


Figure 3.12.: Mechanical power based on the BEM based tool HAWTOPT

### 3.3. Aerodynamic Performance of the Rotor Using BEM

Figures 3.12 to 3.15 show the overall rotor performance in terms of power, thrust and the power and thrust coefficients using the computational BEM based tool HAWTOPT. Figure 3.16 and Figure 3.17 show the local power and thrust coefficients along the blade at the design TSR. The control of the rotor is chosen so that it operates at  $\text{TSR}=7.5$  and  $\text{pitch}=0 \text{ deg}$  up to a rotational speed of 9.6RPM. At 9.6RPM the power was very close to rated power and at rated power the blades were pitched to obtain rated power. In the optimization process the controller was not considered, but tuned after the structural lay out of the rotor was carried out.

### 3.4. 3D Blade Geometry

The cross-sectional shape along the blade was based on the FFA-W3-xxx airfoil family as described in Section 3.1. The root of the blade was defined using a circular shape. In the tip region of the blade,  $r/R > 0.99$ , the blade was blended into a symmetric NACA0015 airfoil in order to more easily close the tip.

Interpolation between the base airfoils was done according to a similar procedure as used in XFOIL [17]<sup>1</sup>. The points defining the base airfoils were splined and re-distributed according to the same distribution function based on their normalized accumulated curve length.

---

<sup>1</sup>see [http://web.mit.edu/drela/Public/web/xfoil/xfoil\\_doc.txt](http://web.mit.edu/drela/Public/web/xfoil/xfoil_doc.txt).

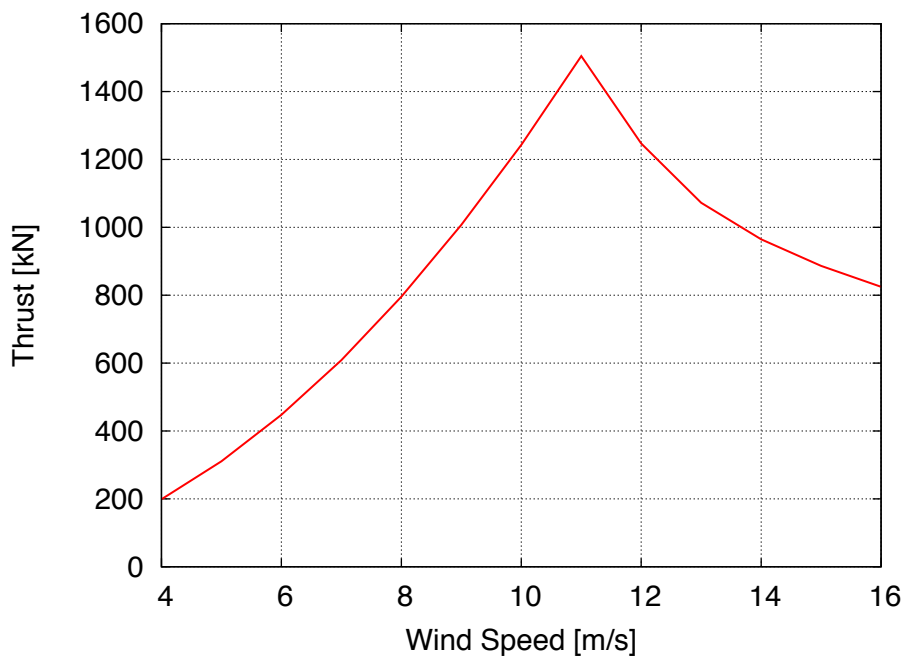


Figure 3.13.: Thrust based on the BEM based tool HAWTOPT

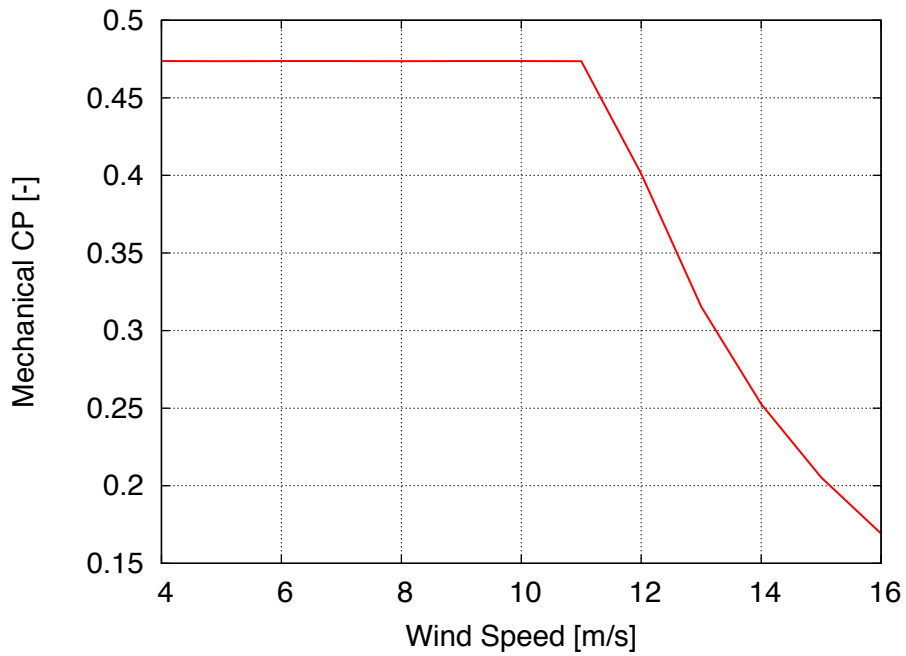


Figure 3.14.: Mechanical power coefficient based on the BEM based tool HAWTOPT

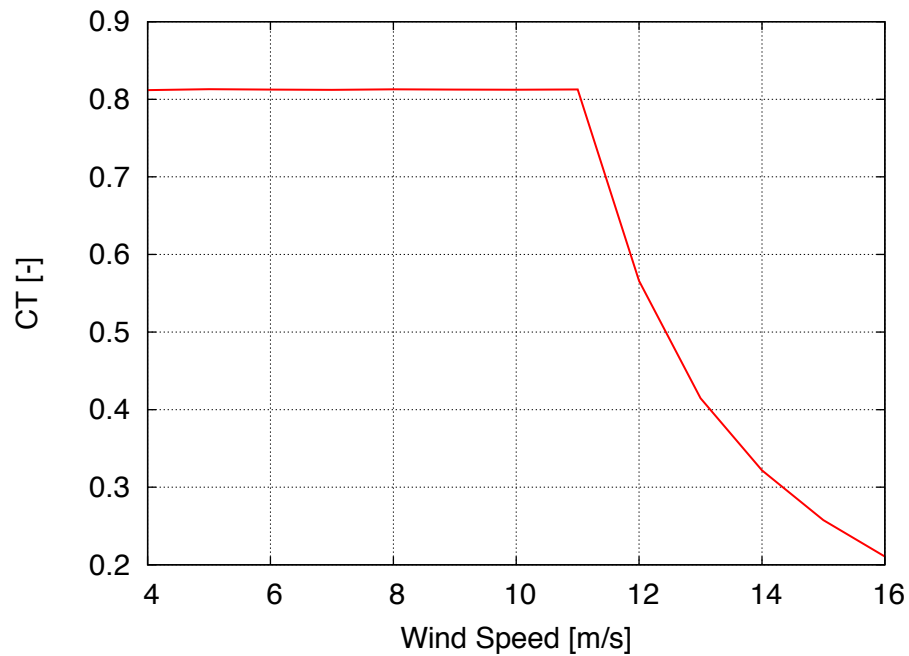


Figure 3.15.: Thrust coefficient based on the BEM based tool HAWTOPT

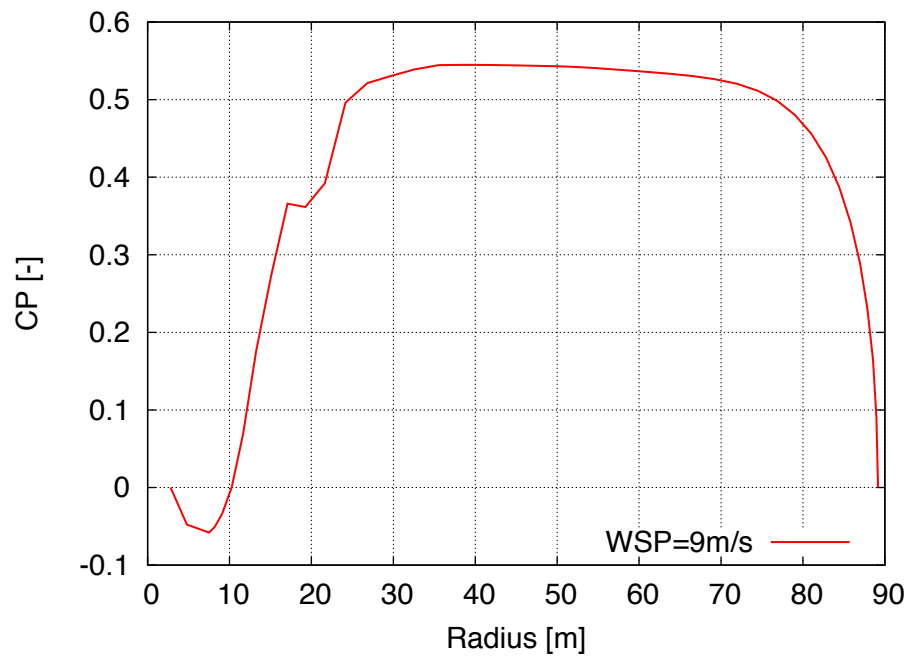


Figure 3.16.: Local mechanical power coefficient at maximum global power coefficient based on the BEM based tool HAWTOPT

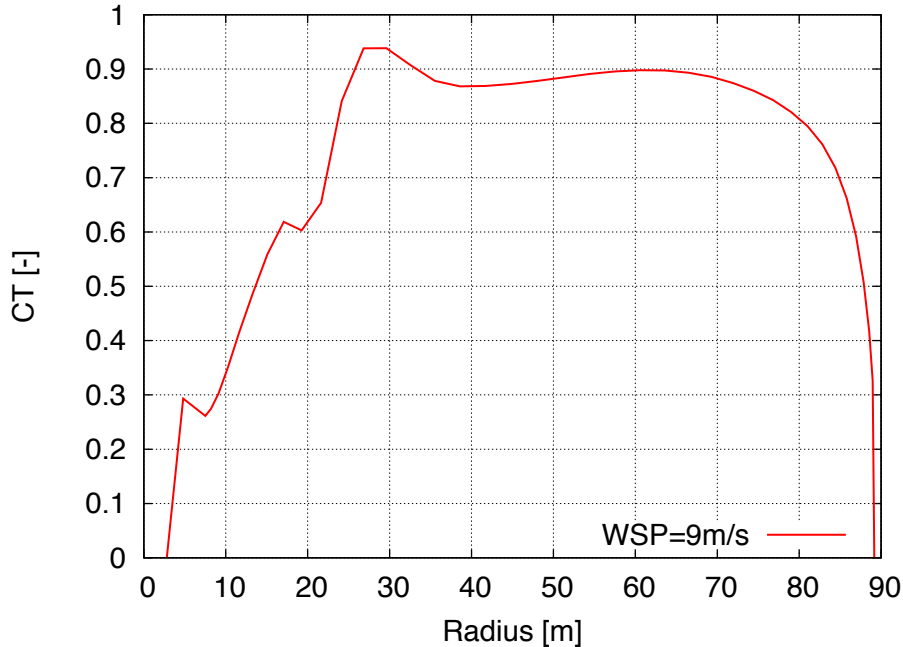


Figure 3.17.: Local thrust coefficient at maximum global power coefficient based on the BEM based tool HAWTOPT

The new airfoil shape was calculated by cubically interpolating between the corresponding points along the contour of the airfoils for a given relative thickness.

The Gurney flaps added to the root part of the blade were smooth wedge shapes. An example of an airfoil cross-section fitted with a Gurney flap with a height to chord ratio  $h_{gf}/c = 0.025$  is shown in Figure 3.18. Table 3.1 lists the Gurney flap height and length factor as function of span for the blade. At the blade root the Gurney flaps needed to be very large due to the thick airfoils and thick boundary layers in this region. Further outwards, the flap heights were chosen smaller, to ensure no deterioration of the lift to drag ratio of the airfoils. In Appendix B, the airfoil properties, and locations in the database are summarized.

The 3D blade shape was parameterized using the following parameters: A 3D curve in space containing the  $x$ -,  $y$ -, and  $z$ -coordinates of the blade pitch axis,  $x$ -,  $y$ -, and  $z$ -rotations for each section along this axis relative to the blade root reference coordinate system (where the rotation around the  $z$ -axis represents the twist angle), the chord and relative thickness distributions and finally the normalized distance from the leading edge to the blade axis,  $x/c_{pitch}$ ,  $y/c_{pitch}$ . Refer to Figure 3.11 for the planform of the blade. In order to close the tip, the chord distribution along the blade was modified slightly in the tip region compared to the distribution shown in Figure 3.11. In the present blade definition, the hub region was included ( $r/R=[0:2.8]$  m) to ease the task of mesh generation.

The parameters  $(x/c)_{pitch}$  and  $(y/c)_{pitch}$  were chosen such that the blade planform would smoothly transition from  $(x/c)_{pitch}, (y/c)_{pitch} = (0.5, 0)$  to  $(0.35, 0)$  at approximately  $r/R$

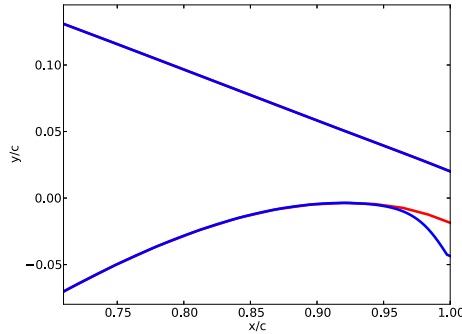


Figure 3.18.: The FFA-W3-480 airfoil fitted with a 2.5% chord Gurney flap with a base length factor of 3.

$r/R [-]$	$h_{gf}/c [-]$	$l_{gf}/h_{gf} [-]$
0.0300	0.0000	1.0
0.0600	0.0500	1.0
0.0800	0.1000	1.0
0.1000	0.1600	1.0
0.1250	0.1400	1.0
0.1500	0.1000	1.5
0.2000	0.0300	2.0
0.2327	0.0250	3.0
0.3148	0.0127	3.0
0.3300	0.0100	3.0
0.4000	0.0000	3.0

Table 3.1.: Gurney flap height to chord ratio ( $h_{gf}/c$ ) and length to height factor ( $l_{gf}/h_{gf}$ ) as function of normalized radius.

$= 0.4$ . Figure 3.19 shows the normalized offset,  $(x/c)_{pitch}$ , of the leading edge relative to the blade axis.

Two blade shapes were created, a straight blade with no pre-bending and another blade with pre-bending, which was based on the steady state deflection of the blades for the turbine operating at 5 m/s. Figure 3.20 shows the blade axis shape including pre-bending. Note that the pre-bended blade shape does not include coning. Note also that the  $x$ - and  $y$ -rotation angles for each section are set to zero, that is, the sections along the blade were simply shifted in the  $y$ -direction according to the local blade axis. This is referred to as a *sheared blade shape* as opposed to a *rotated blade shape*, where the  $x$ - and  $y$ -rotation angles are chosen such that each section will locally remain normal to the blade axis.

The blade properties are provided both as cubic spline representations and as tabulated data. See Appendix A and B for details. Figure 3.21 shows the final blade shape, and Figure 3.22 shows a detailed view of the root part of the blade where the Gurney flap

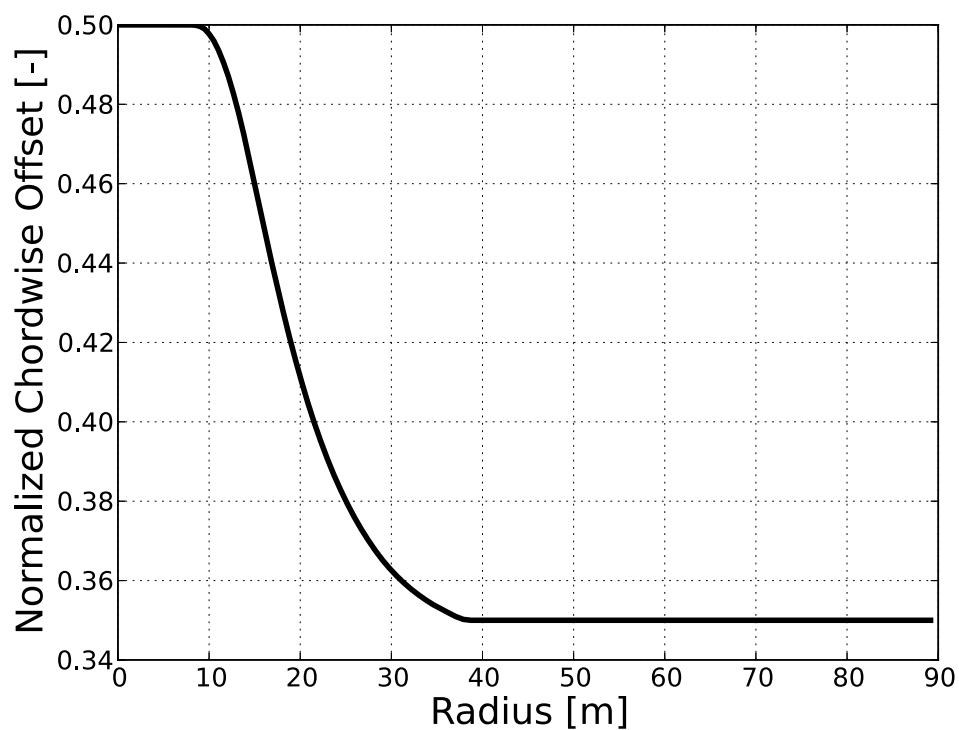


Figure 3.19.: The normalized leading edge offset  $(x/c)_{pitch}$  relative to the blade axis vs normalized blade span.

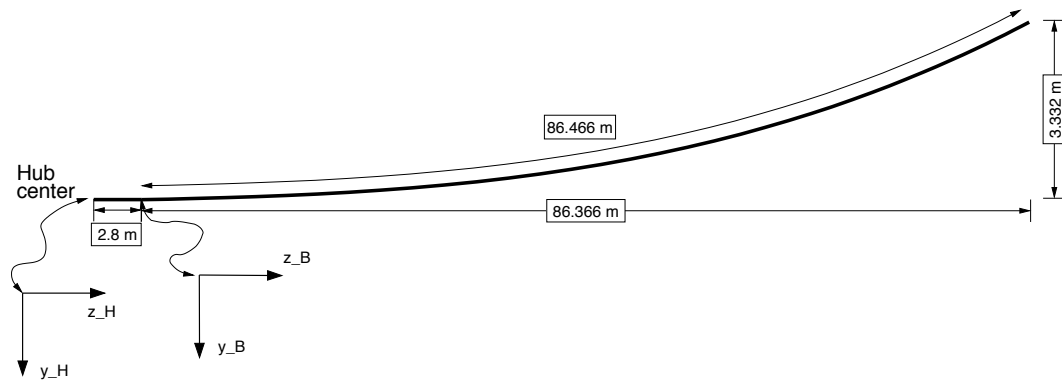


Figure 3.20.: The prebend shape of the DTU 10MW RWT blade.

added to the trailing edge is visible.

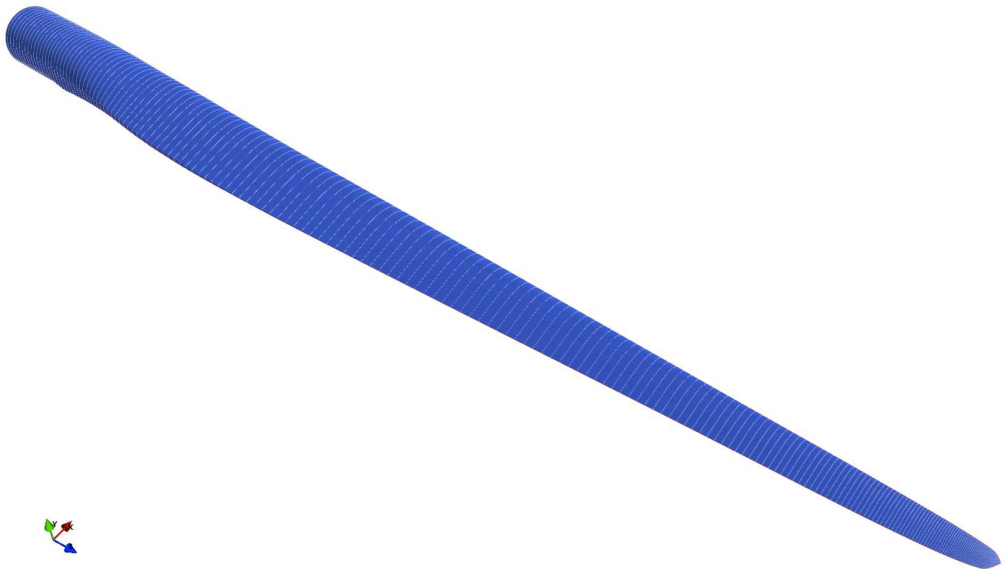


Figure 3.21.: 3D blade shape for the straight blade.

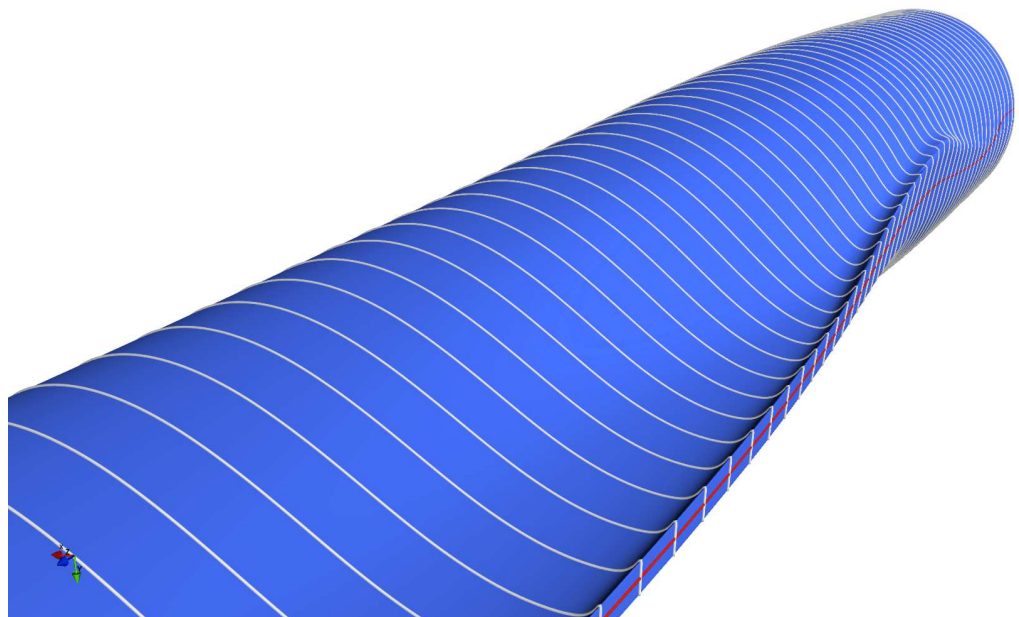


Figure 3.22.: Detailed view of the root of the blade showing the Gurney flaps.

### 3.5. Aerodynamic Steady State Performance

In this section 3D CFD simulations carried out on the rotor using EllipSys3D are described and compared to BEM-based results computed using HAWCStab2.

### 3.5.1. HAWCStab2 Simulation Setup

In addition to the BEM simulations presented in Section 3.2, simulations were performed on the rotor using HAWCStab2 [18]. HAWCStab2 is a tool for computing and analyzing modal properties of a wind turbine in open- or closed-loop operation. In this section, however, only the aerodynamic performance predictions are included.

### 3.5.2. 3D CFD Simulation Setup

All simulations were carried out using the pressure-based incompressible Reynolds averaged Navier-Stokes flow solver EllipSys3D [5, 6, 7], using the steady state moving mesh option in EllipSys3D [19]. Two sets of simulations were carried out: one set assuming either a fully developed turbulent boundary layer on the blade surface using the  $k - \omega$  SST model by Menter [8], and a second set where the boundary layers were allowed to transition freely using the  $\gamma - Re_\theta$  correlation based transition model of Menter et al. [9], for the present implementation see [10]. For the latter set of simulations, the turbulence intensity at the rotor was set to 0.1%.

The blade geometry used in the simulations was the straight blade with no pre-bending. All three blades were included in the mesh, and the rotor was modelled without coning or tilt. The tower and ground boundary were omitted from the simulations. Two mesh configurations were made: One where the rotor was modelled as one watertight surface without the nacelle and spinner, and another where the spinner and nacelle were included as one single water tight surface. The rotor was simulated as a stiff structure, with the blade shape kept in its un-deflected shape.

The surface mesh was generated using an automated procedure that uses an in-house set of Python [20] scripts combined with Pointwise [21]. The rotor surface mesh consisted of 256 cells in the chord-wise direction and 128 cells in the span-wise direction with a  $64 \times 64$  tip cap on each blade tip. The volume mesh was of the O-O type and was generated using HypGrid, a hyperbolic mesh generator written by Sørensen [11]. To obtain a  $y+$  of less than 2 the height of the first cell in the boundary layer was set to  $2 \times 10^{-6}$  m. The nacelle surface mesh consisted of a total of 42 blocks of  $32 \times 32$  cells. The rotor-only mesh consisted of a total of 108 blocks of  $32 \times 32$  cells, whereas the rotor-nacelle mesh had a total of 150 blocks of  $32 \times 32$  cells. The volume mesh was grown away from the surface using 128 cells in the normal direction to form a sphere with a diameter of approximately 1800 m totaling  $14.1 \times 10^6$  and  $21.3 \times 10^6$  cells, respectively. Note that both the chord-wise and normal distributions used for the 3D rotor mesh were coarser than those used for the 2D simulations. This choice was made primarily to ensure a reasonable computation cost of the 3D simulations. Figures 3.23 to 3.25 show the mesh cut along a constant  $y$ -plane at 60 m radius, and views of the rotor and nacelle surface mesh.

### 3.5.3. Operational Parameters

Table 3.2 summarises the steady state operational parameters computed using HAWC-Stab2 [18] using the controller described in Section 5. Two sets of data were computed;

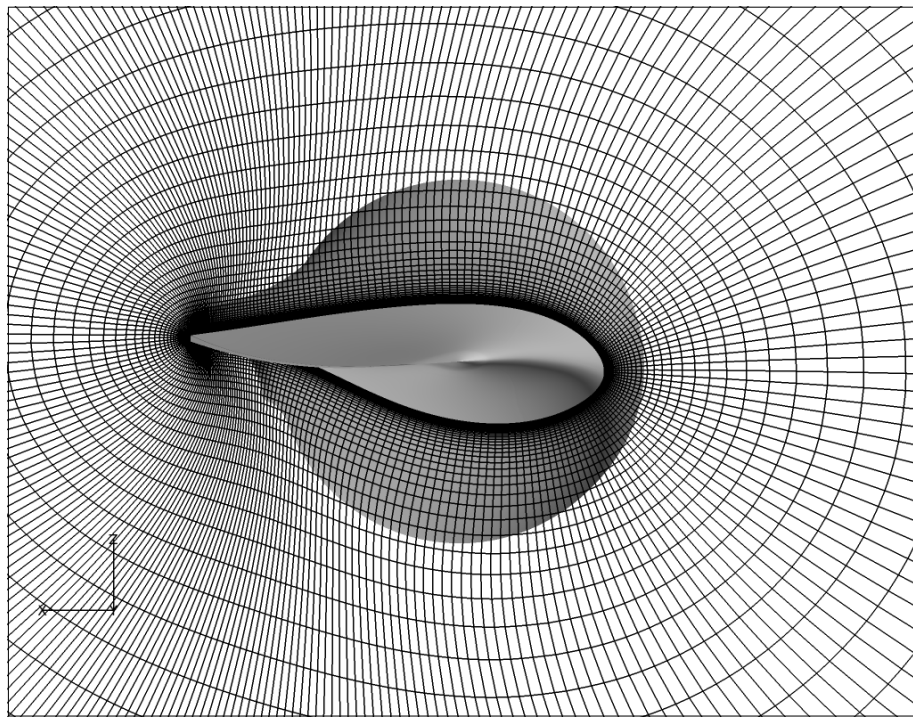


Figure 3.23.: Volume mesh around the rotor cut along a constant  $y$ -plane at 60 m radius.

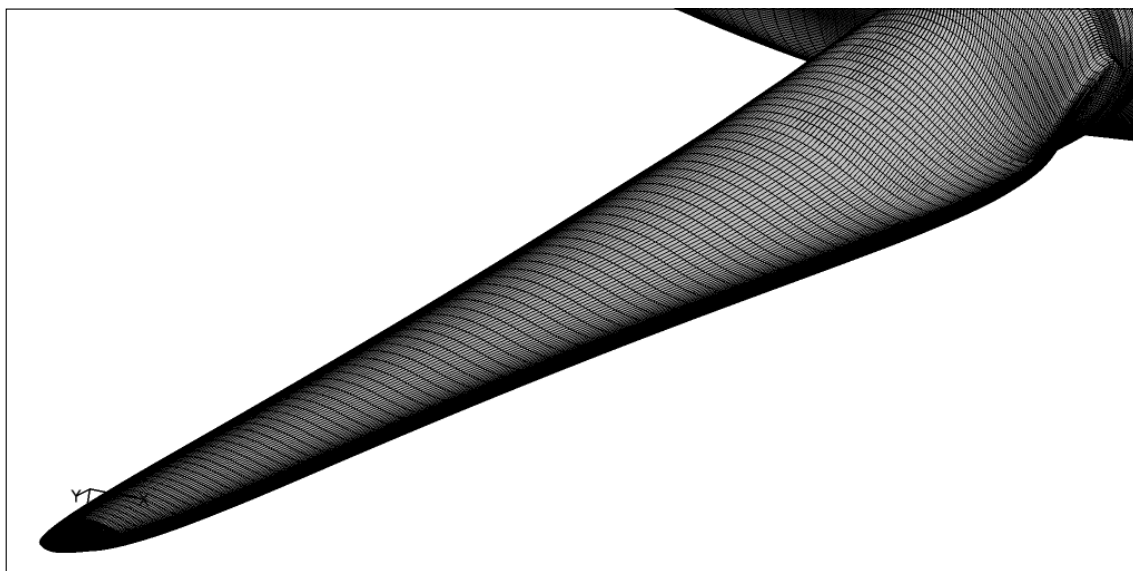


Figure 3.24.: Surface mesh on the rotor.

one set with a stiff structure, where the rotor tilt and cone were set to zero, and the blade prebend was removed, corresponding to the blade layout used in the CFD simulations, and another set based on simulations with both tilt, cone, prebend and structural deflections.

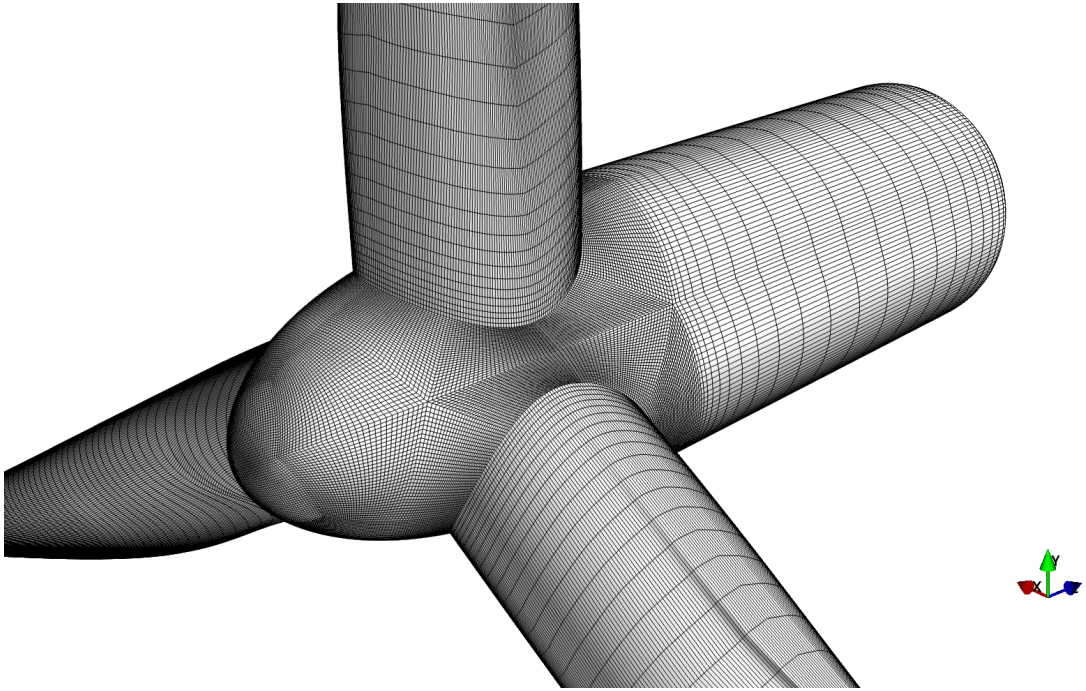


Figure 3.25.: Surface mesh on the rotor and nacelle configuration.

In the comparison presented in the following section, the data based on simulations with a stiff structure were used (i.e. Table 3.2 (b)). All simulations were carried out with a density of  $\rho=1.225 \text{ kg/m}^3$  and a dynamic viscosity of  $\mu=1.78406\text{e-}5 \text{ kg/(m}\cdot\text{s)}$ .

### 3.5.4. Results

Tables 3.3 to 3.5 list the integrated power, thrust, and power and thrust coefficients as function of wind speed for the fully turbulent CFD simulations and simulations taking into account transition from laminar to turbulent flow as well as the BEM-based HAWCStab2 simulations. The integrated power and thrust are plotted against wind speed in Figure 3.26 and corresponding power and thrust coefficients in 3.27 for the CFD simulations in comparison to the steady state BEM-based simulations using HAWCStab2. As expected the fully turbulent simulations and simulations assuming transition from laminar to turbulent flow predict very similar results, corresponding well with the 2D airfoil simulations presented in Section 3.1.2. The CFD simulations predict a 4.5% higher power production below rated power than HAWCStab2, and an approximately 3% higher thrust. This difference primarily stems from the difference in the BEM airfoil data for the thick airfoil sections in the root region of the blade compared to the 3D CFD predictions. Although the BEM airfoil data is based on CFD, 2D simulations of flow over thick airfoils, with a subsequent correction for stall delay, do not fully account for the 3D flow which is observed in the 3D CFD simulations.

Wind speed [m/s]	Pitch [deg.]	RPM	Wind speed [m/s]	Pitch [deg.]	RPM
4.0	2.581	6.000	4.0	2.751	6.000
5.0	1.800	6.000	5.0	1.966	6.000
6.0	0.789	6.000	6.0	0.896	6.000
7.0	0.000	6.000	7.0	0.000	6.000
8.0	0.000	6.423	8.0	0.000	6.426
9.0	0.000	7.225	9.0	0.000	7.229
10.0	0.000	8.029	10.0	0.000	8.032
11.0	0.000	8.837	11.0	0.000	8.836
12.0	4.507	9.600	12.0	4.502	9.600
13.0	7.088	9.600	13.0	7.266	9.600
14.0	8.991	9.600	14.0	9.292	9.600
15.0	10.598	9.600	15.0	10.958	9.600
16.0	12.042	9.600	16.0	12.499	9.600
17.0	13.376	9.600	17.0	13.896	9.600
18.0	14.630	9.600	18.0	15.200	9.600
19.0	15.824	9.600	19.0	16.432	9.600
20.0	16.968	9.600	20.0	17.618	9.600
21.0	18.071	9.600	21.0	18.758	9.600
22.0	19.141	9.600	22.0	19.860	9.600
23.0	20.181	9.600	23.0	20.927	9.600
24.0	21.192	9.600	24.0	21.963	9.600
25.0	22.175	9.600	25.0	22.975	9.600

(a) Elastic structure

(b) Stiff structure

Table 3.2.: Operational parameters based on HAWCStab2 computations for the rotor simulated (a) *with* and (b) *without* prebend, cone, tilt and structural deflections, respectively. The pitch setting is defined positive for nose down.

Wind speed [m/s]	Mech. Power [kW]	Thrust [kN]	$C_P$ [-]	$C_T$ [-]
5.0	809.1	356.2	0.423	0.931
6.0	1558.0	506.2	0.471	0.919
8.0	3848.2	817.0	0.491	0.834
9.0	5496.6	1036.6	0.493	0.837
10.0	7561.0	1282.6	0.494	0.838
11.0	10088.5	1555.0	0.495	0.840
12.0	11170.2	1325.1	0.423	0.602
16.0	10875.8	853.6	0.174	0.218
20.0	10678.5	687.7	0.087	0.112
25.0	10192.8	577.4	0.043	0.060

Table 3.3.: Integrated rotor thrust, power and thrust and power coefficients as function of wind speed for the fully turbulent CFD simulations.

Wind speed [m/s]	Mech. Power [kW]	Thrust [kN]	$C_P$ [-]	$C_T$ [-]
5.0	824.9	358.5	0.431	0.937
6.0	1576.6	509.2	0.477	0.924
8.0	3887.9	822.9	0.496	0.840
9.0	5543.0	1042.7	0.497	0.841
10.0	7610.7	1288.3	0.497	0.842
11.0	10140.8	1560.4	0.498	0.843
12.0	11228.8	1329.1	0.425	0.603
16.0	10961.1	857.6	0.175	0.219
20.0	10798.4	692.8	0.088	0.113
25.0	10320.4	581.7	0.043	0.061

Table 3.4.: Integrated rotor thrust, power and thrust and power coefficients as function of wind speed for the CFD simulations taking into account transition from laminar to turbulent flow.

Wind speed [m/s]	Mech. Power [kW]	Thrust [kN]	$C_P$ [-]	$C_T$ [-]
4.0	280.2	225.9	0.286	0.923
5.0	799.1	351.5	0.418	0.919
6.0	1532.7	498.1	0.464	0.904
7.0	2506.1	643.4	0.478	0.858
8.0	3730.7	797.3	0.476	0.814
9.0	5311.8	1009.1	0.476	0.814
10.0	7286.5	1245.8	0.476	0.814
11.0	9698.3	1507.4	0.476	0.814
12.0	10639.1	1270.8	0.402	0.577
13.0	10648.5	1082.0	0.317	0.419
14.0	10639.3	967.9	0.253	0.323
15.0	10683.7	890.8	0.207	0.259
16.0	10642.0	824.8	0.170	0.211
17.0	10640.0	774.0	0.142	0.175
18.0	10639.9	732.5	0.119	0.148
19.0	10652.8	698.4	0.102	0.126
20.0	10646.2	668.1	0.087	0.109
21.0	10644.0	642.1	0.075	0.095
22.0	10641.2	619.5	0.065	0.084
23.0	10639.5	599.8	0.057	0.074
24.0	10643.6	582.7	0.050	0.066
25.0	10635.7	567.2	0.044	0.059

Table 3.5.: Integrated rotor thrust, power and thrust and power coefficients as function of wind speed for the BEM-based HAWCStab2 simulations.

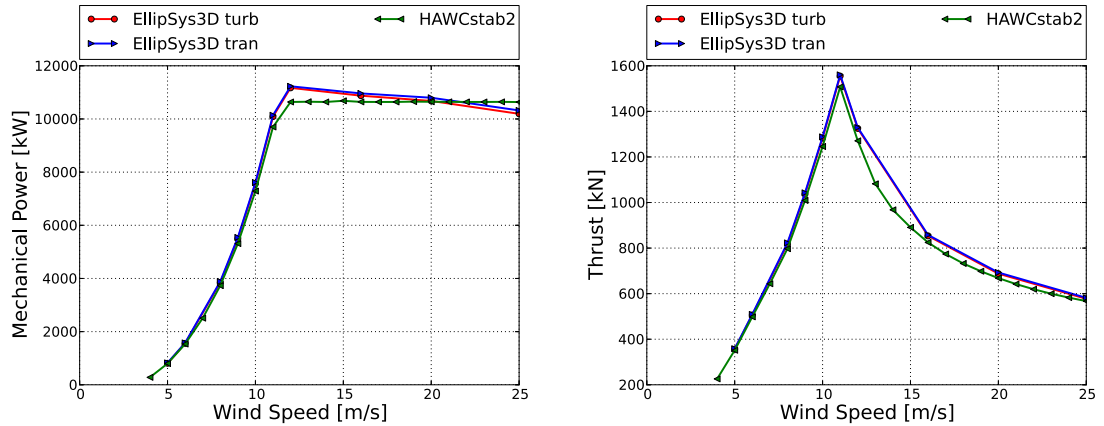


Figure 3.26.: Power and thrust as function of wind speed for the rotor computed using EllipSys3D compared to HAWCStab2 simulations.

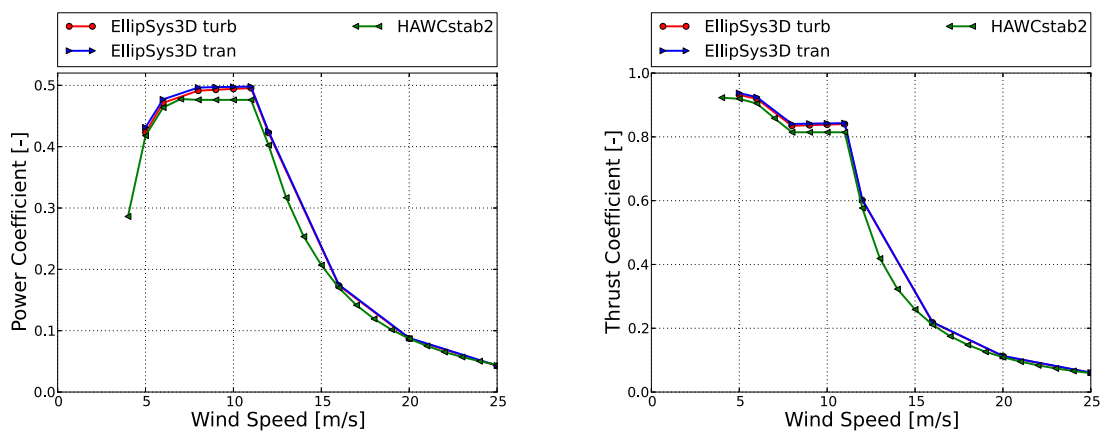


Figure 3.27.: Power and thrust coefficients as function of wind speed for the rotor computed using EllipSys3D compared to HAWCStab2 simulations.

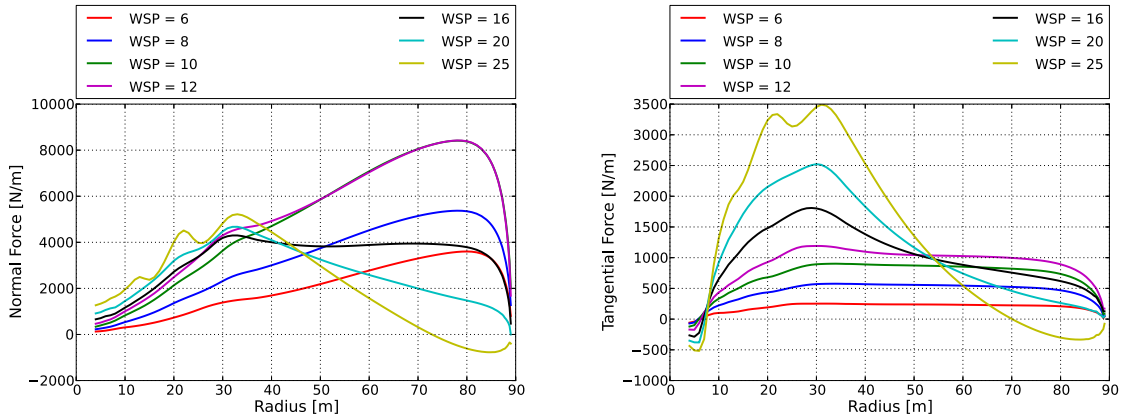


Figure 3.28.: Normal and tangential forces as function of radius for a range of wind speeds computed using EllipSys3D taking into account transition from laminar to turbulent flow.

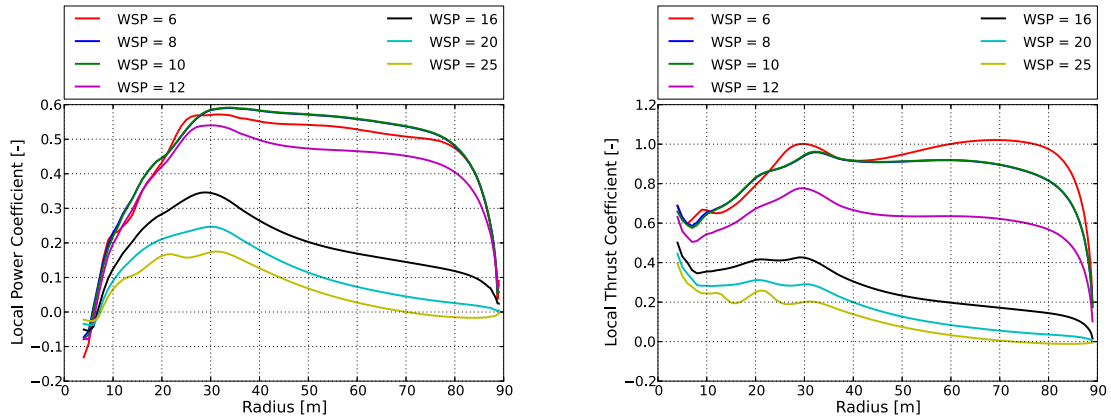


Figure 3.29.: Local power and thrust coefficients as function of radius for a range of wind speeds computed using EllipSys3D taking into account transition from laminar to turbulent flow.

## 4. Structural Design

### 4.1. Structural Design of the Blade

#### 4.1.1. Material Parameters

##### Introduction

The reference blade is made from glass fiber reinforced composites and balsa wood, which is used as sandwich core material. The composite layup of the reference blade was defined in terms of a stacking-sequence of layers representing multidirectional plies. That is, each ply has fibers at multiple orientation angles.

In this section the apparent elastic properties of these multidirectional plies are estimated based on the properties of the constituent materials using simple micromechanics equations and classical lamination theory.

This approach facilitates the investigation of the effect of different material choices on turbine behavior. If, for example, the Young's modulus of the fibers is changed, a new set of elastic properties of the multidirectional plies is immediately obtained.

Measured elastic properties of commercially available, multidirectional materials are very similar to the ones derived in this section.

Elastic properties of balsa wood are also listed in this section.

##### Elastic Properties of Unidirectional Laminae

Two unidirectional laminae made of E-glass fibers in an epoxy matrix were considered to be the basic building blocks for the multidirectional plies. The two unidirectional laminae differ in fiber volume fraction. The apparent material properties of the laminae were derived based on typical properties of the constituent materials using simple micromechanics equations from [22].

The apparent Young's modulus of the unidirectional laminae in the direction of the fibers was computed as

$$E_1 = E_{f1}V_f + E_mV_m, \quad (4.1)$$

where  $E_{f1}$  is the longitudinal Young's modulus of the fibers,  $E_m$  is the Young's modulus of the matrix,  $V_f$  is the volume fraction of fibers, and  $V_m$  is the volume fraction of the matrix.

The apparent Young's modulus of the unidirectional laminae in the direction transverse to the fibers was computed as

$$E_2 = \frac{E_m}{1 - \sqrt{V_f} \left( 1 - \frac{E_m}{E_{f2}} \right)}, \quad (4.2)$$

where  $E_{f2}$  is the transverse Young's modulus of the fibers.

The apparent in-plane shear modulus of the unidirectional laminae was computed as

$$G_{12} = \frac{G_m}{1 - \sqrt{V_f} \left( 1 - \frac{G_m}{G_{f12}} \right)}, \quad (4.3)$$

where  $G_{f12}$  is the in-plane shear modulus of the fibers and  $G_m$  is the shear modulus of the matrix.

The apparent out-of-plane shear modulus  $G_{23}$  of the unidirectional laminae was computed as

$$G_{23} = \frac{G_m}{1 - \sqrt{V_f} \left( 1 - \frac{G_m}{G_{f23}} \right)}, \quad (4.4)$$

where  $G_{f23}$  is the transverse shear modulus of the fibers.

The apparent in-plane Poisson's ratio  $\nu_{12}$  of the unidirectional laminae was computed as

$$\nu_{12} = \nu_{f12} V_f + \nu_m V_m, \quad (4.5)$$

where  $\nu_{f12}$  is the major Poisson's ratio of the fibers, and  $\nu_m$  is the Poisson's ratio of the matrix.

The apparent out-of-plane Poisson's ratio  $\nu_{23}$  of the unidirectional laminae was computed as

$$\nu_{23} = \frac{E_2}{2G_{23}}, \quad (4.6)$$

where  $E_2$  and  $G_{23}$  are given by equations (4.2) and (4.4), respectively.

The apparent mass density of the unidirectional laminae was computed as

$$\rho = \rho_f V_f + \rho_m V_m, \quad (4.7)$$

where  $\rho_f$  is the mass density of the fibers, and  $\rho_m$  is the mass density of the matrix.

Finally, the remaining elastic properties of the unidirectional laminae are determined by symmetry considerations:

$$E_3 = E_2 \quad (4.8)$$

$$G_{13} = G_{12} \quad (4.9)$$

$$\nu_{13} = \nu_{12}. \quad (4.10)$$

The mechanical properties of the epoxy matrix and the E-glass fibers used in this report are given in Table 4.1 and 4.2, respectively [23]. The apparent mechanical properties of the unidirectional laminae computed using Equations (4.1) to (4.10) are given in Table 4.3.

Property	Value	Unit
Young's modulus $E_m$	4.0	GPa
Poisson's ratio $\nu_m$	0.35	—
Shear modulus $G_m^{(a)}$	1.4815	GPa
Mass density $\rho_m$	1140.0	kg/m <sup>3</sup>

(a)  $G_m = E_m/(2(1 + \nu_m))$

Table 4.1.: Mechanical properties of the epoxy matrix [23].

Property	Value	Unit
Longitudinal Young's modulus $E_{f1}$	75.0	GPa
Transverse Young's modulus $E_{f2}$	75.0	GPa
Major Poisson's ratio $\nu_{f12}$	0.2	—
In-plane shear modulus $G_{f12}^{(a)}$	31.25	GPa
Transverse shear modulus $G_{f23}^{(b)}$	31.25	GPa
Mass density $\rho_f$	2550.0	kg/m <sup>3</sup>

(a) chosen as  $G_{f12} = E_{f1}/(2(1 + \nu_{f12}))$

(b) chosen as  $G_{f23} = G_{f12}$

Table 4.2.: Mechanical properties of E-glass fibers [23].

### Elastic Properties of Multidirectional Plies

The apparent in-plane properties  $E_1$ ,  $E_2$ ,  $G_{12}$  and  $\nu_{12}$  of the multidirectional plies were derived using classical lamination theory. That is, for the sake of simplicity the multidirectional plies are represented by a single orthotropic material.<sup>1</sup> As a consequence neither a specific number of laminae nor a specific stacking sequence are specified, when defining the composite layup of the blade. Table 4.4 lists the fiber orientations and apparent mechanical properties of the multidirectional plies.

### Elastic Properties of Sandwich Core Materials

The elastic properties of balsa wood, which is used as sandwich core material, are listed in Table 4.5. Note that the tensile modulus and compression modulus of balsa wood are different in reality.

---

<sup>1</sup>Bend-twist coupling terms that exist even for balanced and symmetric plies are ignored.

Property	Lamina 1	Lamina 2	Unit
Fiber volume fraction $V_f$	0.5	0.55	—
Young's modulus in fiber direction $E_1$	39.5	43.05	GPa
Young's modulus transv. to fiber dir. $E_2$	12.099 01	13.425 83	GPa
In-plane shear modulus $G_{12}$	4.538 64	5.046 98	GPa
Out-of-plane shear modulus $G_{23}$	4.538 64	5.046 98	GPa
In-plane Poisson's ratio $\nu_{12}$	0.2750	0.2675	—
Out-of-plane Poisson's ratio $\nu_{23}$	0.3329	0.3301	—
Mass density $\rho$	1845.0	1915.5	kg/m <sup>3</sup>

Table 4.3.: Apparent mechanical properties of two unidirectional laminae.

Multidirectional Ply	Uniax	Biax	Triax	
Fiber volume fraction $V_f$	0.55	0.5	0.5	—
Unidirectional lamina	Lamina 2	Lamina 1	Lamina 1	
0° fibers	95	0	30	%
90° fibers	5	0	0	%
+45° fibers	0	50	35	%
-45° fibers	0	50	35	%
Young's modulus $E_1$	41.63	13.92	21.79	GPa
Young's modulus $E_2$	14.93	13.92	14.67	GPa
Shear modulus $G_{12}$	5.047	11.50	9.413	GPa
Poisson's ratio $\nu_{12}$	0.241	0.533	0.478	—
Shear modulus $G_{13} = G_{23}^{(a)}$	5.046 98	4.538 64	4.538 64	GPa
Mass density $\rho$	1915.5	1845.0	1845.0	kg/m <sup>3</sup>

(a) not computed but chosen identical to the values of the respective laminae in Table 4.3.

Table 4.4.: Fiber orientation and apparent mechanical properties of the multidirectional plies.

Property	Balsa direction	Value	Unit
Young's modulus $E_1$	radial	0.050	GPa
Young's modulus $E_2$	tangential	0.050	GPa
Young's modulus $E_3$	axial	2.730	GPa
Shear modulus $G_{12}$ <sup>(a)</sup>	radial-tangential	0.016 67	GPa
Shear modulus $G_{13}$	radial-axial	0.150	GPa
Shear modulus $G_{23}$	tangential-axial	0.150	GPa
Poisson's ratio $\nu_{12}$	radial-tangential	0.5	—
Poisson's ratio $\nu_{13}$	radial-axial	0.013	—
Poisson's ratio $\nu_{23}$	tangential-axial	0.013	—
Mass density $\rho$		110	kg/m <sup>3</sup>

<sup>(a)</sup> Computed assuming trans. isotropy:  $G_{12} = E_1 / (2(1 + \nu_{12}))$ .

Table 4.5.: Mechanical properties of balsa wood [24] [25]. The indices 1, 2 and 3 refer to the blade's longitudinal, transverse and out-of-plane direction, respectively.

Multidirectional Ply	Uniax	Biax	Triax	
Longitudinal tensile failure strain $\varepsilon_1^T$	2.10	1.60	2.20	%
Longitudinal compressive failure strain $\varepsilon_1^C$	1.50	1.50	1.80	%

Table 4.6.: Characteristic values of the longitudinal tensile and compressive strain to failure of the multidirectional plies (5% fractile values with a confidence level of 95%).

## Strength Properties

After reviewing the information available in the OptiDAT database [26] and the DOE / MSU Composite Material Fatigue Database [27], typical values of the tensile and compressive strain to failure were assumed for the multidirectional plies. The values given in Table 4.6 are assumed to be characteristic values. That is, they are assumed to be 5% fractile values with a confidence level of 95%.

### 4.1.2. Blade Internal Structure and Composite Layup Definition

A complete description of the blade's external and internal geometry and composite layup was generated in the form of an ABAQUS [28] finite element shell model. 8-node layered shell elements (ABAQUS element type S8R) were used. The outer surface of the blade was used as reference surface, containing the finite element nodes ("node offset option"), except for the shear webs, where the midsurface was used as reference surface.

Solid 20-node hexahedral elements (ABAQUS element type C3D20) were used to represent the adhesive connecting the suction side shell to the pressure side shell at the trailing edge. This was done to obtain a more realistic prediction of the trailing edge buckling behavior. No other adhesive connections were modeled in any way. The whole blade is represented by approximately 35.000 elements corresponding to 104.000 nodes or 616.000 degrees of freedom. Figure 4.2 shows the entire model, while Figure 4.12 shows a representative section of the model.

The model does not include the blade prebend described in Chapter 3.

For the purpose of composite layup definition the blade was partitioned into 11 regions circumferentially and 100 regions radially, see Figures 4.1 and 4.2. The airfoil shape includes the Gurney Flaps described in Chapter 3.

The structural design is based on a classical approach using a load carrying box girder with two shear webs. A third shear web is present close to the trailing edge from  $r = 21.8$  m to the tip.

The cap width  $a$  is also the distance between the shear webs as shown in Figure 4.3. The cap width varies along the length of the blade, as shown in Figure 4.4. The curve in Figure 4.4 is a cubic spline defined in Table A.6 in Appendix A. The authors are aware that a constant cap width would be beneficial from a manufacturing perspective.

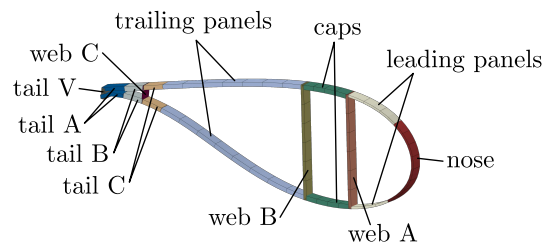


Figure 4.1.: For composite layup definition the blade was partitioned into 11 regions circumferentially.

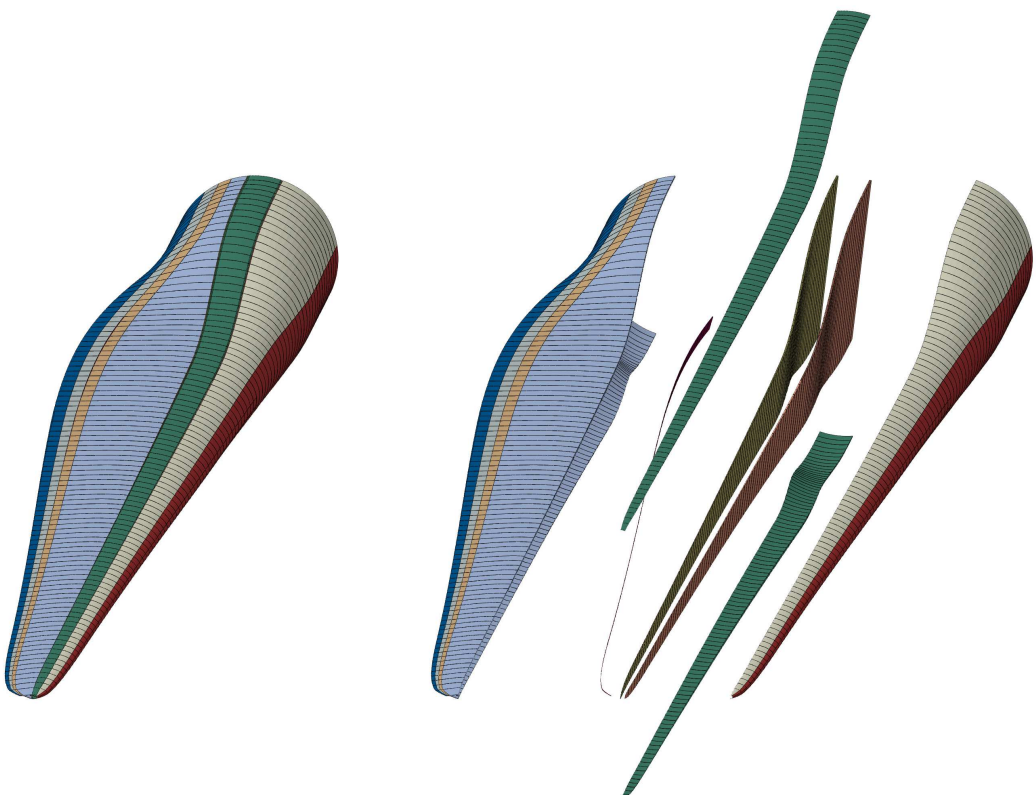


Figure 4.2.: For composite layup definition the blade was partitioned into 11 regions circumferentially and 100 regions radially.

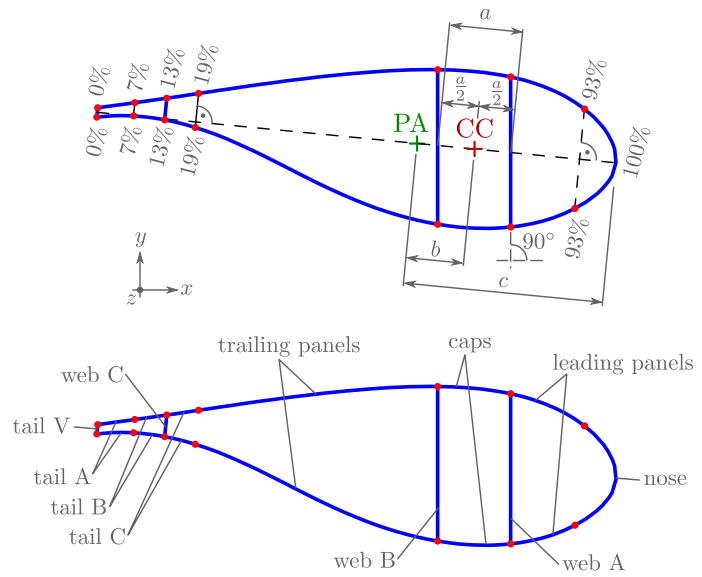


Figure 4.3.: Internal geometry and regions for layup definition.

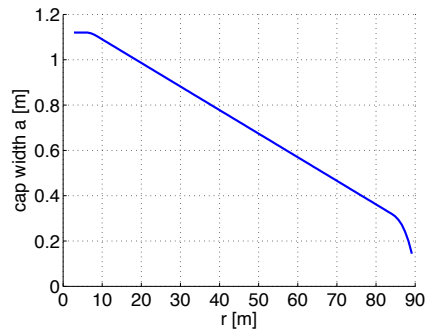


Figure 4.4.: Cap width  $a$  along radial position  $r$ .

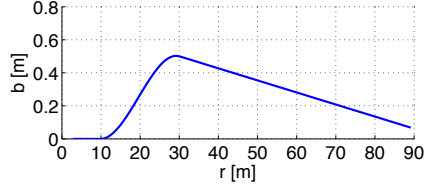


Figure 4.5.: Distance  $b$  between the pitch axis (PA) and the cap center (CC) along radial position  $r$ .

Region	Layup identical to
Web B	Web A
Tail C	Trailing Panels
Tail V	Tail A

Table 4.7.: Regions with identical layup definition.

The caps were approximately placed at the maximum thickness of the airfoil in order to obtain maximum flapwise bending stiffness. Figure 4.5 shows the distance  $b$  between the pitch axis (PA) and the cap center (CC). The curve in Figure 4.5 is a cubic spline defined in Table A.5 in Appendix A.

The caps are limited by the intersection of the shear webs with the airfoil, where the shear webs make an angle of 90° with the global x-axis, as shown in Figure 4.3. The regions Tail A, Tail B and Tail C extend from 0 % to 7 % of the chord length, from 7 % to 13 % of the chord length and from 13 % to 19 % of the chord length, respectively. The region nose extends from 97 % to 100 % of the chord length, as shown in Figure 4.3. The blue lines in Figure 4.3 represent the outer surface of the airfoil and the mid-surface of the three shear webs.

The composite layup of the reference blade is defined in terms of a stacking-sequence of layers representing multidirectional plies. A stacking sequence is assigned to each of the  $11 \cdot 100 = 1100$  regions. One table defines the layup for each of the 11 circumferential regions shown in Figure 4.1. Table 4.8 shows an example layup definition. The stacking sequence is defined from the outer surface (first column) to the inner surface (last column). Some circumferential regions have identical layup definitions as shown in Figure 4.7. The complete layup description can be found in the data repository: `structural_models/composite_layup`.

The layup of important regions is visualized in Figure 4.6. For manufacturing the layup definition would have to be interpreted as a stacking of larger, continuous plies. This question is not further examined here.

The layup definition exhibits relatively large and abrupt thickness changes at the boundaries between neighboring regions. In reality, individual plies would be terminated (dropped off) at slightly different locations in order to avoid stress concentrations. For computational purposes the approach followed is suitable.

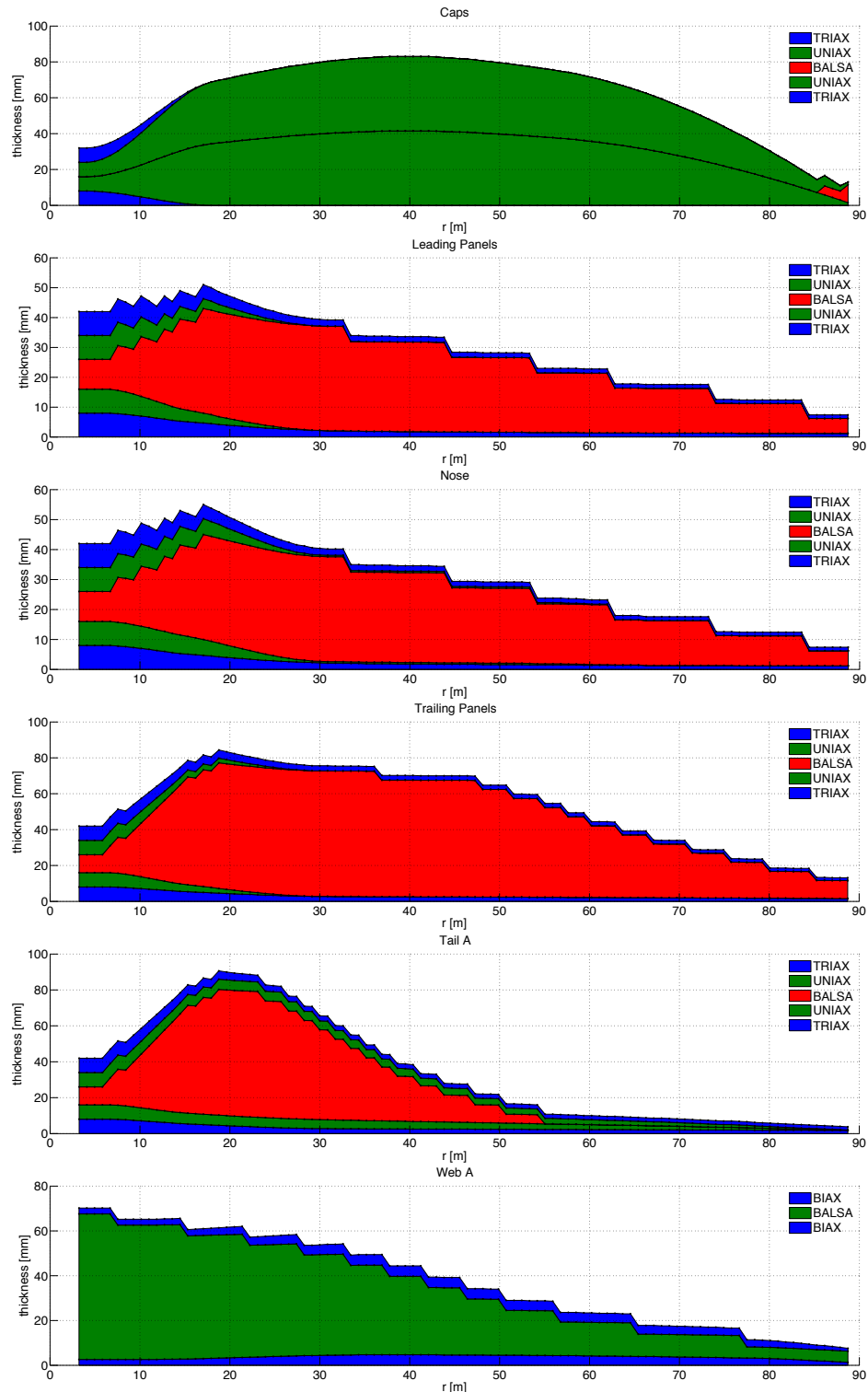


Figure 4.6.: Composite layup of the regions: Caps, leading panels, nose, trailing panels, tail A and web A.

Number	$r_{\text{start}}$ [m]	$r_{\text{end}}$ [m]	TRIAX [mm]	UNIAX [mm]	BALSA [mm]	UNIAX [mm]	TRIAX [mm]
...							
007	7.982	8.846		20.0	5.0	20.0	
008	8.846	9.709		20.0	10.0	20.0	
009	9.709	10.573		20.0	10.0	20.0	
010	10.573	11.437		19.8	15.0	19.8	
011	11.437	12.300	0.1	19.2	15.0	19.2	0.1
012	12.300	13.164	0.3	18.4	20.0	18.4	0.3
013	13.164	14.028	0.4	17.4	25.0	17.4	0.4
...							

Table 4.8.: Example layup definition table for one circumferential region.

#### 4.1.3. Cross Section Stiffness and Mass Properties

The cross section stiffness and mass properties of the blade were computed using BECAS, the **B**Eam **C**ross section **A**nalysis **S**oftware. BECAS determines cross section stiffness and mass properties using a finite element based approach. It handles arbitrary cross section geometries, any number of arbitrarily oriented anisotropic materials, and correctly accounts for all geometrical and material induced couplings. Further information is available in [29, 30] and at <http://www.becas.dtu.dk>.

BECAS requires a 2D finite element mesh of the blade cross section with corresponding material and orientation assignments as input. The required input was generated based on the information contained in the 3D finite element shell model using an automatic procedure (BECAS element type: Q8). Figure 4.7 shows an example 2D finite element mesh together with the elastic center, shear center, mass center and elastic axes orientation computed by BECAS.

Tables 4.9 and 4.10 list the cross section stiffness and mass properties obtained, which served as input to the aero-elastic analysis in Chapter 6. The structural twist angle is the angle between the first elastic axis (or principal axis) and the chord line. A positive structural twist angle corresponds to a counterclockwise rotation in Figure 4.7. The structural twist angle was set to zero for  $r < 10$  m, where the bending stiffnesses about the two axes are very similar.

For the properties defined in Tables 4.9 and 4.10 the terms “flapwise” and “edgewise” refer to the first and second elastic axis (or “principal axis”), respectively. That is, the flapwise bending stiffness is the bending stiffness about the first elastic axis, the flapwise shear stiffness is the shear stiffness in the direction of the first elastic axis, etc.

All centers in Table 4.10 are given in a coordinate system which has its origin at the half-chord point, x-axis parallel to the chord-line pointing toward the leading edge, and y-axis pointing from the pressure to the suction side.

Figure 4.8 shows how the different materials (multiaxial plies) contribute to the blade mass.

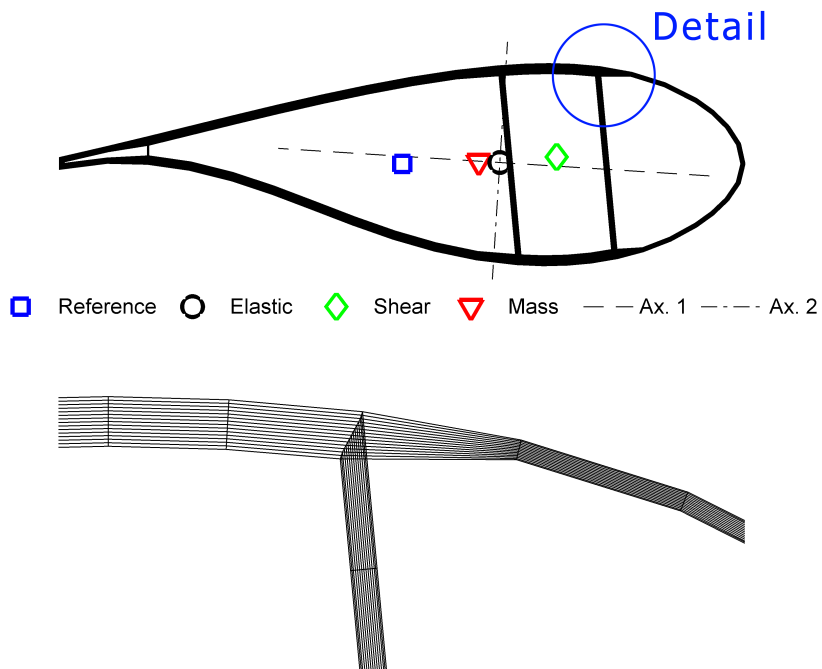


Figure 4.7.: BECAS input: Example 2D finite element mesh together with the elastic center, shear center, mass center and elastic axes orientation computed by BECAS.

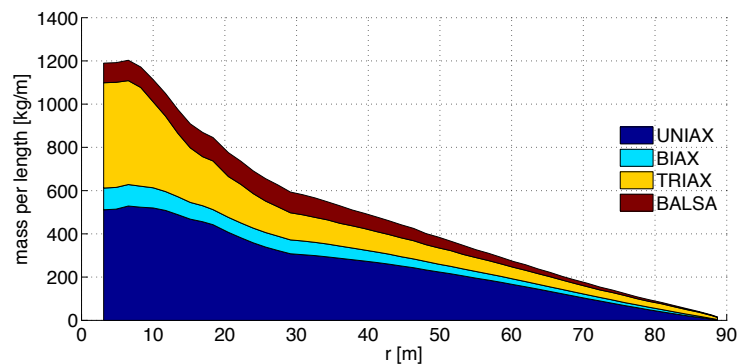


Figure 4.8.: Blade mass: Contribution of the different materials.

### **Remark on shear stiffness**

In the theory of shear flexible beams the rotation of a cross-section  $\theta$  is  $-dw/dx$  due to rotation of the beam axis plus an additional rotation  $\gamma$  due to shear straining:

$$\theta = -\frac{dw}{dx} + \gamma \quad (4.11)$$

The “average shear strain”  $\gamma$  is proportional to the shear force  $Q$ :

$$Q = S \gamma , \quad (4.12)$$

where  $S$  is the *shear stiffness* given in Table 4.9.

Radius m	Structural Twist degree	Flapwise Bending Stiff. N m <sup>2</sup>	Edgewise Bending Stiff. N m <sup>2</sup>	Flapwise Shear Stiff. N	Edgewise Shear Stiff. N	Torsional Stiff. N m <sup>2</sup>	Extensional Stiff. N
2.800	0.000	6.18725E+10	6.10115E+10	2.50824E+09	1.94278E+09	2.74558E+10	1.77862E+10
4.815	0.000	6.21762E+10	6.11168E+10	2.50777E+09	1.94662E+09	2.74780E+10	1.78421E+10
6.542	0.000	6.29962E+10	6.11280E+10	2.48659E+09	1.97301E+09	2.73239E+10	1.80823E+10
8.269	0.000	6.01470E+10	5.80854E+10	2.34480E+09	1.95352E+09	2.55957E+10	1.76558E+10
9.996	0.000	5.45560E+10	5.30459E+10	2.08251E+09	1.85385E+09	2.21409E+10	1.68486E+10
11.724	-42.804	4.41034E+10	5.08642E+10	1.77813E+09	1.78112E+09	1.83903E+10	1.59612E+10
13.450	-35.909	3.57932E+10	4.39376E+10	1.45588E+09	1.64835E+09	1.39696E+10	1.48286E+10
15.176	-25.737	2.83899E+10	3.78679E+10	1.17463E+09	1.51044E+09	1.01006E+10	1.38507E+10
16.904	-18.927	2.26907E+10	3.37672E+10	9.87891E+08	1.44507E+09	7.44770E+09	1.32546E+10
18.344	-14.276	1.91244E+10	3.17664E+10	8.70111E+08	1.46609E+09	6.02823E+09	1.28963E+10
20.498	-10.974	1.47868E+10	2.75020E+10	7.25240E+08	1.24506E+09	4.05189E+09	1.16858E+10
22.232	-8.868	1.26547E+10	2.53839E+10	6.79697E+08	1.10706E+09	3.35076E+09	1.10112E+10
23.959	-7.622	1.08079E+10	2.29327E+10	6.16349E+08	9.45730E+08	2.63788E+09	1.02689E+10
25.686	-6.790	9.33271E+09	2.06461E+10	5.70040E+08	8.14261E+08	2.11902E+09	9.65883E+09
27.413	-6.090	8.13856E+09	1.87714E+10	5.36634E+08	7.17667E+08	1.74369E+09	9.18510E+09
29.141	-4.893	6.88290E+09	1.87537E+10	5.01728E+08	6.13038E+08	1.41867E+09	8.71213E+09
30.868	-4.530	6.09324E+09	1.76630E+10	4.86058E+08	6.01692E+08	1.24251E+09	8.55730E+09
32.595	-4.252	5.39730E+09	1.65096E+10	4.65596E+08	5.74650E+08	1.08953E+09	8.38322E+09
34.323	-4.103	4.79796E+09	1.50449E+10	4.45718E+08	5.64692E+08	9.61883E+08	8.19207E+09
36.050	-3.926	4.26081E+09	1.35375E+10	4.20064E+08	5.36743E+08	8.33476E+08	7.95316E+09
37.778	-3.651	3.79054E+09	1.24279E+10	3.98514E+08	5.25806E+08	7.44524E+08	7.76397E+09
39.505	-3.350	3.35012E+09	1.14783E+10	3.76533E+08	5.12586E+08	6.54383E+08	7.55514E+09
41.233	-3.092	2.95524E+09	1.04400E+10	3.56451E+08	4.84342E+08	5.70807E+08	7.32778E+09
42.873	-2.886	2.61810E+09	9.46806E+09	3.37613E+08	4.71450E+08	5.02898E+08	7.10845E+09
44.601	-2.646	2.29631E+09	8.50260E+09	3.14753E+08	4.59389E+08	4.43186E+08	6.85305E+09
46.328	-2.411	2.01437E+09	7.70395E+09	2.98755E+08	4.46571E+08	3.91844E+08	6.62376E+09
48.055	-2.255	1.75660E+09	6.64424E+09	2.82327E+08	4.17871E+08	3.37858E+08	6.30815E+09
49.783	-2.047	1.53489E+09	5.97308E+09	2.63675E+08	4.05095E+08	2.97084E+08	6.05849E+09
51.510	-1.855	1.34558E+09	5.32893E+09	2.51635E+08	3.92555E+08	2.63998E+08	5.82418E+09
53.237	-1.696	1.16892E+09	4.66924E+09	2.33438E+08	3.65159E+08	2.25158E+08	5.52959E+09
55.051	-1.563	1.01512E+09	3.99141E+09	2.21808E+08	3.51108E+08	1.98463E+08	5.25179E+09
56.779	-1.417	8.85389E+08	3.53974E+09	2.08679E+08	3.38907E+08	1.74822E+08	5.00724E+09
58.506	-1.289	7.71509E+08	3.04985E+09	1.98834E+08	3.13670E+08	1.52364E+08	4.73786E+09
60.233	-1.187	6.68362E+08	2.61588E+09	1.85593E+08	2.99341E+08	1.32571E+08	4.45066E+09
61.961	-1.095	5.78103E+08	2.27123E+09	1.74101E+08	2.87791E+08	1.16517E+08	4.18450E+09
63.688	-0.995	4.99512E+08	1.92187E+09	1.63097E+08	2.64946E+08	1.01385E+08	3.90198E+09
65.354	-0.922	4.29167E+08	1.66656E+09	1.53130E+08	2.54049E+08	8.91635E+07	3.63473E+09
67.081	-0.865	3.63223E+08	1.39311E+09	1.45336E+08	2.40108E+08	7.70090E+07	3.33659E+09
68.808	-0.782	3.04756E+08	1.18456E+09	1.35486E+08	2.20012E+08	6.56225E+07	3.04974E+09
70.535	-0.741	2.53941E+08	9.97633E+08	1.26316E+08	2.09432E+08	5.67279E+07	2.77644E+09
72.324	-0.672	2.08212E+08	8.15025E+08	1.17166E+08	1.90429E+08	4.79912E+07	2.48857E+09
74.052	-0.649	1.71028E+08	6.85021E+08	1.09077E+08	1.81272E+08	4.14719E+07	2.24347E+09
75.779	-0.599	1.38112E+08	5.53974E+08	9.88451E+07	1.74860E+08	3.56780E+07	1.98122E+09
77.459	-0.574	1.08707E+08	4.60660E+08	9.09441E+07	1.53558E+08	2.89875E+07	1.72044E+09
79.186	-0.539	8.39391E+07	3.59048E+08	8.32025E+07	1.42945E+08	2.39023E+07	1.46713E+09
80.961	-0.572	6.30619E+07	2.96049E+08	7.43227E+07	1.39482E+08	2.02493E+07	1.24959E+09
82.688	-0.547	4.42760E+07	2.17147E+08	6.27766E+07	1.23199E+08	1.55370E+07	1.00649E+09
84.377	-0.593	2.83398E+07	1.55000E+08	4.96109E+07	1.10416E+08	1.13923E+07	7.79107E+08
86.143	-0.688	1.44813E+07	1.00370E+08	3.75804E+07	9.39498E+07	7.21379E+06	5.53866E+08
87.871	-0.793	4.49695E+06	4.17163E+07	2.30147E+07	6.46572E+07	2.93572E+06	3.07403E+08
89.166	-0.955	1.02747E+06	1.27145E+07	1.22510E+07	3.86194E+07	7.93304E+05	1.72203E+08

Table 4.9.: Reference blade cross section stiffness properties.

Radius m	Mass per Length kg/m	Flapwise Rad. of Gyration m	Edgewise Rad. of Gyration m	Mass Center x m	Mass Center y m	Elastic Center x m	Elastic Center y m	Shear Center x m	Shear Center y m
2.800	1189.51	1.8240	1.7652	-0.0042	-0.0035	-0.0049	-0.0032	-0.0029	-0.0095
4.815	1191.64	1.8247	1.7650	-0.0054	-0.0036	-0.0063	-0.0033	-0.0036	-0.0096
6.542	1202.77	1.8196	1.7598	-0.0118	-0.0057	-0.0061	-0.0041	-0.0016	-0.0085
8.269	1171.49	1.7927	1.7476	-0.0173	-0.0054	-0.0161	-0.0045	0.0063	0.0050
9.996	1113.62	1.7357	1.7215	-0.0014	-0.0082	0.0135	-0.0052	0.0374	0.0111
11.724	1049.31	1.6187	1.7196	0.0192	-0.0036	0.0409	0.0025	0.1122	0.0371
13.450	974.63	1.5142	1.6657	0.0981	0.0040	0.1365	0.0081	0.2909	0.0674
15.176	908.74	1.3837	1.6318	0.1562	0.0124	0.2041	0.0110	0.4993	0.1001
16.904	868.87	1.2498	1.6077	0.2543	0.0221	0.3104	0.0164	0.7543	0.0915
18.344	845.51	1.1538	1.5999	0.3217	0.0305	0.3859	0.0227	0.9346	0.0960
20.498	775.15	1.0509	1.5921	0.3852	0.0319	0.4837	0.0217	1.0895	0.1037
22.232	735.79	0.9932	1.5986	0.4255	0.0381	0.5504	0.0287	1.0923	0.1222
23.959	691.12	0.9450	1.5873	0.4811	0.0414	0.6208	0.0334	1.1711	0.1225
25.686	654.85	0.9013	1.5724	0.5367	0.0421	0.6963	0.0354	1.2377	0.1179
27.413	625.88	0.8603	1.5525	0.5858	0.0407	0.7590	0.0345	1.2881	0.1121
29.141	593.32	0.8128	1.5640	0.5752	0.0369	0.7346	0.0308	1.3139	0.0984
30.868	580.97	0.7716	1.5349	0.5885	0.0298	0.7538	0.0235	1.3093	0.0844
32.595	566.23	0.7341	1.5023	0.6065	0.0233	0.7721	0.0168	1.3213	0.0723
34.323	548.24	0.7010	1.4623	0.6111	0.0191	0.7906	0.0124	1.3075	0.0629
36.050	529.65	0.6707	1.4183	0.6269	0.0175	0.8097	0.0106	1.2972	0.0592
37.778	510.31	0.6421	1.3798	0.6337	0.0175	0.8099	0.0107	1.2796	0.0576
39.505	494.68	0.6123	1.3437	0.6212	0.0185	0.7942	0.0119	1.2485	0.0578
41.233	477.51	0.5844	1.3017	0.6167	0.0198	0.7831	0.0132	1.2256	0.0588
42.873	460.93	0.5588	1.2664	0.5993	0.0215	0.7683	0.0150	1.1896	0.0594
44.601	441.78	0.5336	1.2237	0.5852	0.0232	0.7544	0.0169	1.1587	0.0605
46.328	425.33	0.5086	1.1894	0.5665	0.0250	0.7349	0.0189	1.1275	0.0611
48.055	401.38	0.4877	1.1343	0.5744	0.0260	0.7303	0.0202	1.0935	0.0621
49.783	385.14	0.4651	1.1001	0.5542	0.0273	0.7079	0.0217	1.0607	0.0621
51.510	365.95	0.4455	1.0577	0.5472	0.0280	0.6888	0.0228	1.0269	0.0622
53.237	346.94	0.4262	1.0190	0.5313	0.0285	0.6700	0.0235	0.9920	0.0620
55.051	326.32	0.4085	0.9669	0.5248	0.0285	0.6546	0.0239	0.9544	0.0611
56.779	310.27	0.3909	0.9354	0.5022	0.0286	0.6306	0.0241	0.9208	0.0597
58.506	291.66	0.3757	0.8936	0.4964	0.0280	0.6132	0.0238	0.8894	0.0588
60.233	272.43	0.3613	0.8538	0.4816	0.0273	0.5893	0.0235	0.8476	0.0570
61.961	256.95	0.3461	0.8228	0.4593	0.0267	0.5652	0.0229	0.8140	0.0546
63.688	237.77	0.3340	0.7836	0.4497	0.0255	0.5477	0.0220	0.7836	0.0528
65.354	221.77	0.3207	0.7570	0.4256	0.0247	0.5221	0.0212	0.7515	0.0502
67.081	203.15	0.3078	0.7223	0.4056	0.0236	0.4947	0.0203	0.7098	0.0478
68.808	186.77	0.2944	0.6963	0.3838	0.0226	0.4696	0.0194	0.6812	0.0459
70.535	171.66	0.2809	0.6708	0.3589	0.0218	0.4432	0.0187	0.6489	0.0432
72.324	153.75	0.2688	0.6385	0.3474	0.0206	0.4214	0.0177	0.6187	0.0411
74.052	140.05	0.2562	0.6152	0.3205	0.0199	0.3953	0.0170	0.5883	0.0384
75.779	124.35	0.2450	0.5868	0.3034	0.0191	0.3702	0.0164	0.5567	0.0369
77.459	108.93	0.2325	0.5729	0.2719	0.0184	0.3383	0.0159	0.5249	0.0347
79.186	95.18	0.2200	0.5488	0.2494	0.0179	0.3146	0.0154	0.4990	0.0323
80.961	82.34	0.2065	0.5312	0.2162	0.0177	0.2708	0.0154	0.4617	0.0306
82.688	68.28	0.1915	0.5084	0.1887	0.0170	0.2431	0.0149	0.4302	0.0284
84.377	54.47	0.1731	0.4837	0.1433	0.0166	0.2015	0.0144	0.3918	0.0254
86.143	40.65	0.1476	0.4457	0.1014	0.0154	0.1376	0.0138	0.3414	0.0223
87.871	25.20	0.1106	0.3752	0.0474	0.0132	0.0689	0.0122	0.2709	0.0173
89.166	15.42	0.0725	0.2698	0.0150	0.0097	0.0209	0.0091	0.1812	0.0119

Table 4.10.: Reference blade cross section mass properties and centers.

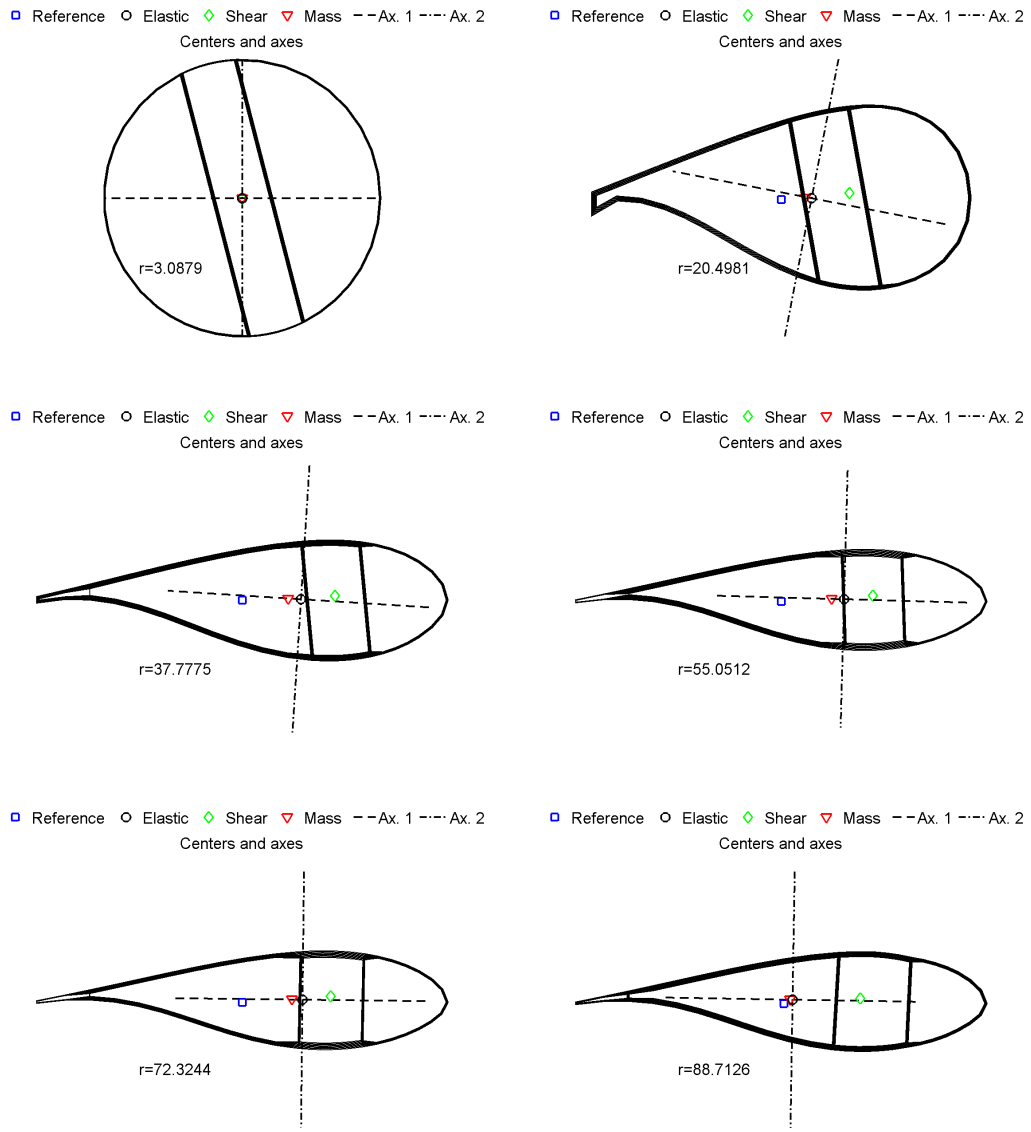


Figure 4.9.: Elastic center, shear center, mass center and elastic axes orientation at  $r = 2.8 \text{ m}, 20.498 \text{ m}, 37.778 \text{ m}, 55.051 \text{ m}, 72.324 \text{ m}, 88.713 \text{ m}$ .

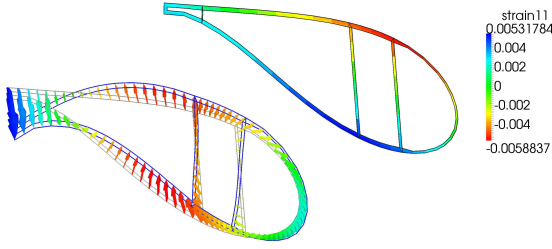


Figure 4.10.: Example 2D cross section mesh with longitudinal strain (background) and warping displacements (foreground) as computed by BECAS.

#### 4.1.4. Strength Analysis

##### Introduction

Strength analysis was performed using a simplified method. The local longitudinal normal strain was computed for the 27 cross sections and 14 load cases per cross section defined in Appendix E, and compared to allowable values listed in Section 4.1.1.

The stress recovery module of the cross section analysis software BECAS was used for this purpose [29, 30]. (In Section 4.1.3 the same software was used to compute cross section stiffness and mass properties.) Longitudinal strains were evaluated at the element centers and compared to allowable values on an element-by-element basis. As a consequence, for laminates consisting of different multidirectional plies (see Figure 4.6), the ply with the lowest allowable strain will normally determine the allowable strain level. Figure 4.7 shows an example 2D finite element mesh.

The cross section forces and moments listed in Appendix E are a “direct” input to the stress recovery module of BECAS. This means that no boundary conditions or load application methods need to be defined. See [29] for further details.

In simple terms, BECAS computes the linear, local 3D stress and strain field as if the cross section investigated was part of a prismatic beam. As a consequence, “end effects” (which affect the stress state close to the root and tip of the blade) and the effects of taper and twist of the blade are not included.

As an example, Figure 4.10 shows a 2D cross section mesh with the longitudinal strain and the warping displacements as computed by BECAS.

##### Partial Safety Factors

Partial safety factors were chosen according to [31].

The partial safety factors for the loads  $\gamma_F$  are defined by:

$$F_d = \gamma_F F_k , \quad (4.13)$$

$C_{1a} = 1.35$	influence of ageing
$C_{2a} = 1.1$	temperature effect
$C_{3a} = 1.1$	laminate produced by preprints, winding techniques, pultrusion or resin infusion method = 1.2 wet laminate with hand lay-up, pressing techniques
= 1.2	
$C_{4a} = 1.0$	post-cured laminate = 1.1 non post-cured laminate
= 1.1	

Table 4.11.: Reduction factors for the material safety factor according to [31].

Multidirectional Ply	Uniax	Biax	Triax	
$\varepsilon_1^T / \gamma_{Ma}$ (tensile)	0.9523	0.7255	0.9976	%
$\varepsilon_1^C / \gamma_{Ma}$ (compressive)	0.6802	0.6802	0.8162	%

Table 4.12.: Design values of the longitudinal tensile and compressive strain to failure of the multidirectional plies.

where  $F_d$  are the design values of the load,  $\gamma_F$  is the partial safety factor for the loads and  $F_k$  is the characteristic value of the loads. Further details are described in Chapter 6.

The partial safety factors for the composite material are given by

$$\gamma_{Ma} = \gamma_{M0} \prod_i C_{ia} , \quad (4.14)$$

where

$$\gamma_{M0} = 1.35 . \quad (4.15)$$

Values for the reduction factors  $C_{ia}$  are given in Table 4.11.

For this study  $C_{3a} = 1.1$  and  $C_{4a} = 1.0$  were chosen, so that the partial safety factor for the material is:

$$\gamma_{Ma} = 1.35 \cdot 1.35 \cdot 1.1 \cdot 1.1 \cdot 1.0 = 2.205 . \quad (4.16)$$

Table 4.12 shows the design values of the longitudinal strain to failure of the multidirectional plies, which is the characteristic values (see Table 4.6) divided by partial safety factor for the material.

The design is safe if the design values of the resistance  $R_d$  are larger than the design values of the loads  $F_d$ :

$$R_d \geq F_d , \quad (4.17)$$

or

$$R_k / \gamma_{Ma} \geq \gamma_F F_k , \quad (4.18)$$

or

$$\frac{R_k}{\gamma_{Ma} \gamma_F F_k} \geq 1 . \quad (4.19)$$

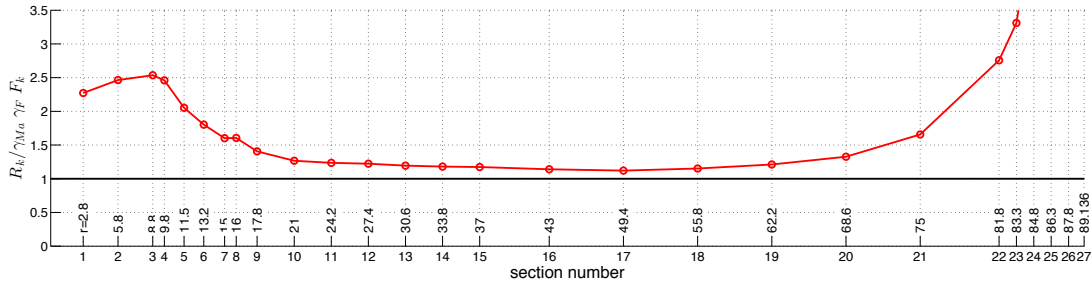


Figure 4.11.: Strength: Minimum value of the left hand side of Equation (4.19) found at each section.

## Results

Figure 4.11 shows the minimum value of the left hand side of Equation (4.19) found at each section. The minima occur mainly due to negative flapwise bending moments causing compressive stresses on the suction side. The design is safe as all values in Figure 4.11 are larger than 1.

### 4.1.5. Buckling Analysis

The ABAQUS 3D finite element shell model described in Section 4.1.2 was used to analyze buckling strength.

The model does not include the blade prebend described in Chapter 3. However, the effect of the slight prebend on the buckling behavior of the blade is negligible.

#### Linear Eigenvalue Buckling Analysis

The buckling strength of the blade was analyzed using linear eigenvalue buckling analysis. The eigenvalue problem is:

$$(\mathbf{K}_0^{MN} + \lambda_i \mathbf{K}_{\Delta}^{MN}) v_i^M = 0 , \quad (4.20)$$

where  $\mathbf{K}_0^{MN}$  is the stiffness matrix corresponding to the base state, which includes the effects of the preloads.  $\mathbf{K}_{\Delta}^{MN}$  is the differential initial stress and load stiffness matrix.  $\lambda_i$  are the eigenvalues and  $v_i^M$  are the buckling mode shapes (eigenvectors). Further details can be found in [28].

For the results presented in this section  $\mathbf{K}_0^{MN}$  included the geometrically non-linear effects of a 50 % preload.

Buckling strength was analyzed for the 27 cross sections and 14 load cases per cross section defined in Appendix E. For this purpose the 3D finite element shell model was divided into sections with a length of approximately 1.2 times the local chord length, containing the cross section investigated (the cross section where the loads are given) in the middle of the section. Kinematic coupling constraints were applied at both ends of the section, forcing

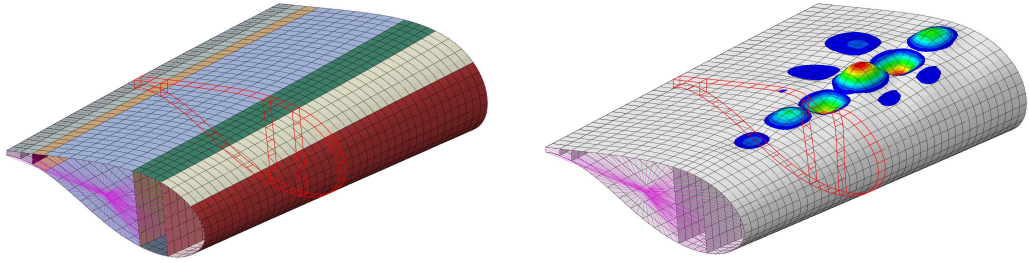


Figure 4.12.: Example buckling model with the cross section investigated highlighted (left) and first eigenmode (right).

$C_{1c} = 1.1$	to account for the scattering of the moduli
$C_{2c} = 1.1$	temperature effect
$C_{3c} = 1.25$	for linear computations

Table 4.13.: Reduction factors for the material safety factor according to [31].

the end sections to move like rigid bodies. Loads were applied to the reference nodes of the coupling constraints in such a way that the cross section investigated was loaded by the cross section forces and moments defined by the respective load case. Figure 4.12 shows an example model with the cross section investigated highlighted.

### Partial Safety Factors

Partial safety factors were chosen according to [31]. The partial safety factors for the loads  $\gamma_F$  are treated in Chapter 6.

The partial safety factors for the composite material are given by

$$\gamma_{MD} = \gamma_{M0} \prod_i C_{ic}, \quad (4.21)$$

where

$$\gamma_{M0} = 1.35. \quad (4.22)$$

Values for the reduction factors  $C_{ic}$  are given in Table 4.13.

As linear eigenvalue analysis was used in this study, the partial safety factor for the material is:

$$\gamma_{MD} = 1.35 \cdot 1.1 \cdot 1.1 \cdot 1.25 = 2.042. \quad (4.23)$$

In [31] it is stated that the partial safety factor for the material  $\gamma_{MD}$  may also be applied to the loads for simplification. This approach is chosen in this report. That is, the design is safe if:

$$\frac{R_k}{\gamma_{MD} \gamma_F F_k} \geq 1, \quad (4.24)$$

where  $F_k$  are the characteristic values of the loads and  $R_k$  are the characteristic values of the resistance.

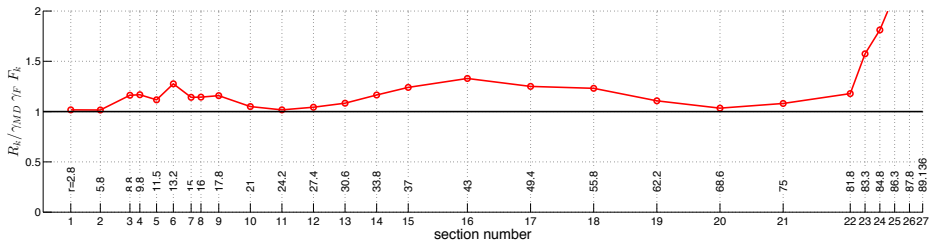


Figure 4.13.: Buckling: Minimum value of the left hand side of Equation (4.24) found at each section.

Property	Value	Unit
Young's modulus $E$	210	GPa
Poisson's ratio $\nu$	0.3	—
Mass density $\rho$ <sup>(a)</sup>	7855(8500)	kg/m <sup>3</sup>
Minimum yield strength $\sigma_y$	355	MPa

<sup>(a)</sup> The mass density was taken as 8500 kg/m<sup>3</sup> in order to account for the mass of secondary structures.

Table 4.14.: Mechanical properties of steel S355.

## Results

Figure 4.13 shows the minimum value of the left hand side of Equation (4.24) found at each section. The minima occur mainly due to negative flapwise bending moments causing compressive stresses on the suction side. The design is safe as all values in Figure 4.13 are larger than 1.

Figure 4.14 shows some typical buckling modes. It can be observed that the various substructures of the blade interact when the blade buckles. For example, from the first two pictures in Figure 4.14 it can be seen that the buckles in the caps are accompanied by corresponding buckles in the neighboring sandwich panels. This is because the model assumes a rotationally stiff connection where the various substructures join. Some production methods would not yield such a rotationally stiff connection for the real blade, and the buckling loads would be correspondingly lower.

## 4.2. Structural Design of the Tower

### 4.2.1. Material Parameters

The tower is made from steel S355, as defined in the European standard DIN EN 10025-2. Material parameters are given in Table 4.14. For the calculation of the cross section mass properties the mass density was increased by approximately 8 % ( $\rho = 8500 \text{ kg/m}^3$ ) in order to account for the mass of secondary structures.

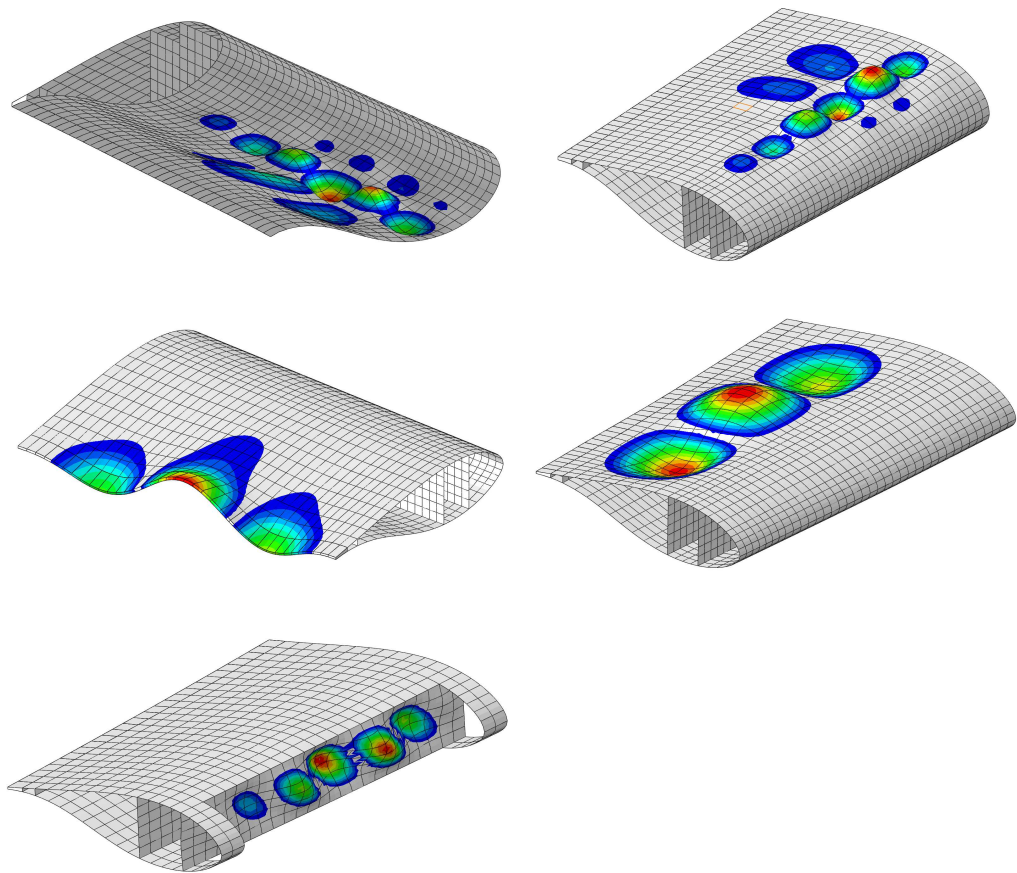


Figure 4.14.: Typical buckling modes. From left to right, top to bottom: Buckling of the pressure side cap, buckling of the suction side cap, buckling of the trailing edge, buckling of the trailing panels, buckling of the leading shear web.

height m	outer diameter m	wall thickness mm
0.000	8.3000	38
11.500	8.0215	38
11.501	8.0215	36
23.000	7.7431	36
23.001	7.7430	34
34.500	7.4646	34
34.501	7.4646	32
46.000	7.1861	32
46.001	7.1861	30
57.500	6.9076	30
57.501	6.9076	28
69.000	6.6292	28
69.001	6.6291	26
80.500	6.3507	26
80.501	6.3507	24
92.000	6.0722	24
92.001	6.0722	22
103.500	5.7937	22
103.501	5.7937	20
115.630	5.5000	20

Table 4.15.: Wall thickness distribution of the tower.

#### 4.2.2. Geometry and Material Thickness

The outer diameter of the tower varies linearly from  $D = 8.3\text{ m}$  at the bottom ( $h = 0\text{ m}$ ) to  $D = 5.5\text{ m}$  at the top ( $h = 115.63\text{ m}$ ). The tower was divided into 10 sections, where the wall thickness is constant in each section. Table 4.15 shows the wall thickness distribution.

#### 4.2.3. Cross Section Stiffness and Mass Properties

The cross section stiffness and mass properties of the tower were derived using the following simple text book formulas:

The cross section area  $A$  is:

$$A = (D^2 - d^2) \frac{\pi}{4}, \quad (4.25)$$

where  $D$  is the outer diameter and  $d$  is the inner diameter.

The mass per length  $m$  is:

$$m = A\rho, \quad (4.26)$$

where  $\rho$  is the mass density.

height m	cross section area $\text{m}^2$	mass per length $\text{kg}/\text{m}$	radius of gyration $\text{m}^4$	second moment of area $\text{m}^4$	torsional stiffness constant
0.000	0.98632	8383.74	2.921	8.41605	16.83210
11.500	0.95308	8101.16	2.823	7.59342	15.18684
11.501	0.90314	7676.68	2.823	7.19909	14.39819
23.000	0.87165	7409.00	2.725	6.47197	12.94394
23.001	0.82343	6999.18	2.726	6.11710	12.23421
34.500	0.79369	6746.37	2.627	5.47792	10.95583
34.501	0.74720	6351.21	2.628	5.15979	10.31958
46.000	0.71921	6113.27	2.529	4.60134	9.20267
46.001	0.67444	5732.78	2.530	4.31732	8.63463
57.500	0.64820	5509.71	2.432	3.83271	7.66541
57.501	0.60516	5143.87	2.432	3.58027	7.16053
69.000	0.58067	4935.68	2.334	3.16290	6.32580
69.001	0.53935	4584.50	2.335	2.93961	5.87921
80.500	0.51661	4391.17	2.236	2.58319	5.16638
80.501	0.47702	4054.66	2.237	2.38671	4.77342
92.000	0.45602	3876.20	2.138	2.08525	4.17049
92.001	0.41816	3554.35	2.139	1.91334	3.82669
103.500	0.39891	3390.76	2.041	1.66114	3.32229
103.501	0.36277	3083.57	2.041	1.51168	3.02335
115.630	0.34432	2926.71	1.937	1.29252	2.58504

Table 4.16.: Cross section stiffness and mass properties of the tower.

The radius of gyration  $r_g$  is:

$$r_g = \frac{1}{4} \sqrt{D^2 + d^2}. \quad (4.27)$$

The second moment of area  $I$  is:

$$I = (D^4 - d^4) \frac{\pi}{64}. \quad (4.28)$$

The torsional stiffness constant  $K$  is:

$$K = (D^4 - d^4) \frac{\pi}{32}. \quad (4.29)$$

Table 4.16 list the stiffness and mass properties of the tower. The total mass is 628 442 kg.

#### 4.2.4. Loads and Boundary Conditions

The static strength and buckling strength of the tower were analyzed for a single static load case only. The following loads were applied:



Figure 4.15.: Tower finite element model and loads.

- The highest horizontal force (thrust force) that occurred at the tower top ( $h = 115.63$  m):  $F = 4605$  kN with the simultaneous bending moment  $M = 17851$  kNm, as listed in Section 6.4.3. (Both values include the partial safety factor for the loads  $\gamma_F$ .)
- A concentrated force corresponding to the tower top mass of 674 002 kg.
- The self-weight of the tower applied as a distributed force on an element-by-element level.

Figure 4.15 shows the finite element model and the loads applied. The model is encastered at the bottom ( $h = 0$  m).

#### 4.2.5. Strength Analysis

An ABAQUS 3D finite element shell model was used to determine the static strength and buckling strength of the tower [28]. 8-node layered shell elements (ABAQUS element type S8R) were used. The outer surface of the tower was used as reference surface, containing the finite element nodes (“node offset option”). The model contains approximately 71.600 elements corresponding to 215.000 nodes or 1.292.000 degrees of freedom. The small element size (high number of elements) is dictated by the buckling wave length (see Figure 4.17).

The partial safety factor for the material is  $\gamma_M = 1.1$  [31].

The design is safe if:

$$\frac{\sigma_y}{\gamma_M \gamma_F \sigma_{VM}} \geq 1 , \quad (4.30)$$

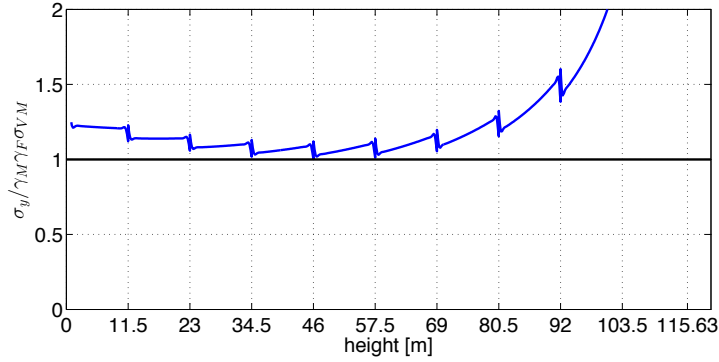


Figure 4.16.: Tower von Mises stress.

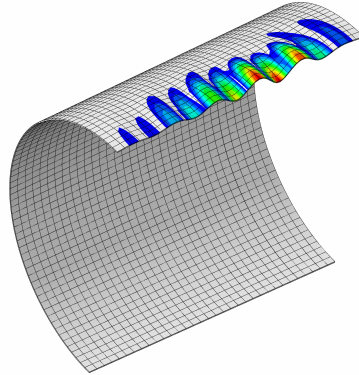


Figure 4.17.: Tower buckling mode.

where  $\sigma_{VM}$  is the von Mises stress,  $\sigma_y$  is the yield strength, and  $\gamma_F$  is the partial safety factor for the loads.

Figure 4.16 shows the left hand side of Equation 4.30. The design is safe as all values are larger than 1.

#### 4.2.6. Buckling Analysis

The buckling strength of the tower was analyzed using linear eigenvalue buckling analysis. See Section 4.1.5 for further details about the analysis procedure.

The tower mass and tower top mass were applied to the model as “dead loads” and buckling was analyzed with respect to a change in the thrust force, see Section 4.2.4.

The critical buckling load obtained was 3.15 times the thrust force given in Section 4.2.4. This can be seen as an available safety factor for material and analysis procedure. Figure 4.17 shows the buckling mode obtained.

## 5. Control

The Basic DTU Wind Energy Controller, which is used for the load case calculations is documented in [32]. The controller features both partial and full load operation capabilities as well as switching mechanisms ensuring smooth switching between the two modes of operation. The partial and full load controllers are both based on classical proportional-integral control theory as well as additional filters such as an optional drive train damper and a notch filter mitigating the influence of rotor speed dependent variations in the feedback. The controller relies on generator speed as the primary feedback sensor. Additionally, the reference generator power is used as a feedback term to smoothen the switching between partial and full load operation. A low-pass filtered wind speed measurement is used for wind speed dependent minimum blade pitch in partial load operation. The controller uses the collective blade pitch angle and electromagnetic generator torque to control the wind turbine. In full load operation a feedback term from the collective blade pitch angle is used to schedule the gains of the proportional-integral controller to counter the effects of changing dynamics of the wind turbine for different wind speeds.

The steady state values for the wind turbine are calculated by the frequency-based aero-servo-elastic analysis software HAWCStab2 [18] where a number of parameters have to be chosen. The rotor speed operating ranges from 6 to 9.6 rpm. The minimum pitch angle is 0 deg. and the optimal tip-speed-ratio is 7.5.

Frequency analysis reveals that the first two tower modes are located at approximately 0.25 Hz and that the first drive-train modes is at approximately 1.85 Hz. These values are not conflicting with the rotor speed harmonic frequency ranges 3P and 6P which are located at (0.30 Hz ... 0.48 Hz) and (0.60 Hz ... 0.96 Hz), respectively. So no extra effort has to be made to avoid operating in troublesome speed ranges.

Using a method documented in [33], HAWCStab2 is used to derive tuning parameters for the controller where the desired properties for a simplified mass-spring-damper formulation of the closed-loop system: For the partial load controller is a natural frequency of 0.05 Hz and a critical damping ratio of 0.7. For the full load controller is a natural frequency of 0.06 Hz and a critical damping ratio of 0.7.

The tuning parameters used by the controller in the HAWC2 simulations is:

```
; Overall parameters
constant 1 10000.0 ; Rated power [kW]
constant 2 0.628 ; Minimum rotor speed [rad/s]
constant 3 1.005 ; Rated rotor speed [rad/s]
constant 4 15.6e6 ; Maximum allowable generator torque [Nm]
constant 5 100.0 ; Minimum pitch angle, theta_min [deg],
                   ; if |theta_min|>90, then a table of <wsp,theta_min> is read ;
                   ; from file named 'wpstable.n', where n=int(theta_min)
constant 6 90.0   ; Maximum pitch angle [deg]
constant 7 10.0   ; Maximum pitch velocity operation [deg/s]
constant 8 0.2    ; Frequency of generator speed filter [Hz]
constant 9 0.7    ; Damping ratio of speed filter [-]
constant 10 1.85  ; Frequency of free-free DT torsion mode [Hz], if zero no notch filter used
; Partial load control parameters
constant 11 0.100131E+08 ; Optimal Cp tracking K factor [kNm/(rad/s)^2], ;
```

```

; Qg=K*Omega^2, K=eta*0.5*rho*A*Cp_opt*R^3/lambda_opt^3
constant 12 0.683456E+08 ; Proportional gain of torque controller [Nm/(rad/s)]
constant 13 0.153367E+08 ; Integral gain of torque controller [Nm/rad]
constant 14 0.0 ; Differential gain of torque controller [Nm/(rad/s^2)]
; Full load control parameters
constant 15 1 ; Generator control switch [1=constant power, 2=constant torque]
constant 16 0.524485E+00 ; Proportional gain of pitch controller [rad/(rad/s)]
constant 17 0.141233E+00 ; Integral gain of pitch controller [rad/rad]
constant 18 0.0 ; Differential gain of pitch controller [rad/(rad/s^2)]
constant 19 0.4e-8 ; Proportional power error gain [rad/W]
constant 20 0.4e-8 ; Integral power error gain [rad/(Ws)]
constant 21 198.32888 ; Coefficient of linear term in aerodynamic gain scheduling, KK1 [deg]
constant 22 693.22213 ; Coefficient of quadratic term in aerodynamic gain scheduling, KK2 [deg^2] &
; (if zero, KK1 = pitch angle at double gain)
constant 23 1.3 ; Relative speed for double nonlinear gain [-]
; Cut-in simulation parameters
constant 24 [cutin_t0] ; Cut-in time [s]
constant 25 4.0 ; Time delay for soft start of torque [1/1P]
; Cut-out simulation parameters
constant 26 [stop_t0] ; Cut-out time [s]
constant 27 [TorqCutOff] ; Time constant for 1st order filter lag of torque cut-out [s]
constant 28 1 ; Stop type [1=linear two pitch speed stop, 2=exponential pitch speed stop]
constant 29 1.0 ; Time delay for pitch stop 1 [s]
constant 30 [PitchVel1] ; Maximum pitch velocity during stop 1 [deg/s]
constant 31 1.0 ; Time delay for pitch stop 2 [s]
constant 32 [PitchVel2] ; Maximum pitch velocity during stop 2 [deg/s]
; Expert parameters (keep default values unless otherwise given)
constant 33 0.5 ; Lower angle above lowest minimum pitch angle for switch [deg]
constant 34 0.5 ; Upper angle above lowest minimum pitch angle for switch [deg], if equal then hard switch
constant 35 95.0 ; Ratio between filtered speed and reference speed for fully open torque limits [%]
constant 36 5.0 ; Time constant of 1st order filter on wind speed used for minimum pitch [1/1P]
constant 37 5.0 ; Time constant of 1st order filter on pitch angle used for gain scheduling [1/1P]
; Drivetrain damper
constant 38 0.0 ; Proportional gain of active DT damper [Nm/(rad/s)], requires frequency in input 10
; Over speed
constant 39 1500.0 ; Over speed percentage before initiating shut-down
; Additional non-linear pitch control term
constant 40 0.0 ; Err0 [rad/s]
constant 41 0.0 ; ErrDot0 [rad/s^2]
constant 42 0.0 ; PitNonLin1 [rad/s]

```

## **6. Aero-Servo-Elastic Design**

### **6.1. Introduction**

The load predictions of the DTU 10MW RWT are very important because the designed blade and turbine have to be able to withstand all loadings experienced during its life time. The considered load cases are from the IEC 61400-1 Ed. 3 standard [34]. The loads during the turbine life time are investigated and the maximum and minimum loads along the blade span as well as the maximum blade tip deflection are given as input to the structural design step. This process is continued while both the structural design and aeroelastic design are satisfied.

### **6.2. Description and Characteristics of the Components**

The properties of the turbine components of the DTU 10MW RWT are established using the up-scaling procedure described in Chapter 2. Details of the aerodynamic design is described in Chapter 3 and details of the structural design of the blades are described in Chapter 4. The gross properties of the DTU 10MW RWT are given in Chapter 2.

The remaining information on the model is presented as follows:

- The nacelle and hub properties in Section 6.2.1
- The drivetrain properties in Section 6.2.2
- The tower properties in Section 6.2.3

#### **6.2.1. Nacelle and Hub**

The hub of the DTU 10MW RWT is located 7.07 m upwind of the tower center line at an elevation of 119 m above the ground. The yaw bearing is placed 115.63 m above ground and with a shaft tilt of 5 deg., this gives a distance directed along the shaft from the hub center to the yaw axis of 7.1 m. The vertical distance along the yaw axis from the tower top to the shaft is 2.75 m.

As mentioned in Chapter 2 the mass and inertia of the hub and nacelle has been reduced relative to an upscaled version of the NREL 5MW reference turbine [1] to give a presumed more realistic value. This is done by scaling the total mass of the nacelle and hub of the Vestas V-164 8MW turbine by substituting  $f_s$  in equation 2.1 by  $s_f = 178.2/164$  corresponding to the difference in rotor diameter. The distribution of nacelle and hub mass of the total hub and nacelle mass are kept at the same ratios as in the NREL 5MW reference turbine. The inertias are scaled to the same levels as an equal weighing

Table 6.1.: Nacelle and hub Properties

Elevation of Yaw Bearing above Ground	119 m
Vertical Distance along Yaw Axis from Yaw Bearing to Shaft	2.75 m
Distance along Shaft from Hub Center to Yaw Axis	7.07 m
Distance along Shaft from Hub Center to Main Bearing	2.7
Hub Mass	105,520 kg
Hub Inertia about Low-Speed Shaft	325,671 kgm <sup>2</sup>
Nacelle Mass	446,036 kg
Nacelle Inertia about Yaw Axis	7,326,346 kgm <sup>2</sup>
Nacelle CM Location Downwind of Yaw Axis	2.687 m
Nacelle CM Location above Yaw Bearing	2.45 m

component of the scaled NREL 5MW reference turbine [1]. This gives a hub mass of 105,520 kg and a hub inertia of 325,671 kgm<sup>2</sup> with center of mass (CM) located in the center of the hub. The nacelle mass is 446,036 kg with CM located 2.687 m downwind of the yaw axis and 2.45 m above the yaw bearing. The nacelle inertia about the yaw axis is 7,326,346 kgm<sup>2</sup>. The nacelle and hub properties are summarized in Table 6.1.

### 6.2.2. Drivetrain Properties

The DTU 10MW RWT has a medium speed gearbox design. This design offers some advantages compared to traditional high speed geared concepts and can be incorporated in to a low weight and compact design. This concept seems to be a good compromise between a direct drive concept with high costs of rare earth metals and a high speed geared concept with higher risk of failure in the high and intermediate stages of the gear box [35], [36]. The DTU 10MW RWT turbine has a rated rotor speed of 9.6 rpm and a rated generator speed of 480 rpm with a gearbox ratio of 50:1. The gearbox is assumed be a double-stage gearbox with no frictional losses. The electrical efficiency of the generator is taken to be 94%. The generator inertia about the medium-speed shaft is 1500.5 kgm<sup>2</sup>. The driveshaft was designed to have a natural frequency of 1.8 Hz and a structural-damping ratio of 0.89% critical (with a free-free mode of a drivetrain composed of a flexible rotor and a generator on a flexible tower). This gives an equivalent driveshaft linear spring constant of 2,452,936,425 Nm/rad. The drivetrain mode depends on whether the full flexibility of the system is taken into account (blades and tower) and if the generator is locked or free. The drivetrain properties are summarized in table 6.3 and the full information on the drivetrain modes are summarized in table 6.2.

Table 6.2.: Natural frequency for the shaft torsion mode

Shaft torsion mode	Nat. freq. [Hz]	Logarithmic Damping[%]	Critical Damping[%]
$F_{\text{free-free flexible}}$	1.803	5.614	0.894
$F_{\text{free-free rigid}}$	4.003	31.455	5.000
$F_{\text{free-fixed flexible}}$	0.502	3.013	0.480
$F_{\text{free-fixed rigid}}$	0.612	4.762	0.758

Table 6.3.: Drivetrain Properties

Rated Rotor Speed	9.6 rpm
Rated Generator Speed	480 rpm
Gearbox Ratio	50 : 1
Electrical Generator Efficiency	94
Generator Inertia about High-Speed Shaft	1500.5 kgm <sup>2</sup>
Equivalent Drive-Shaft Torsional-Spring Constant	2,317,025,352 Nm/rad
Equivalent Drive-Shaft Torsional-Damping Constant	9,240,560 Nm/(rad/s)

### 6.2.3. Tower

The properties of the tower for the DTU 10MW RWT will depend on the type of support structure that has to carry the turbine. This section will only cover the details of a tower for a land based version but additional support structures for offshore use can be designed as well.

The tower is designed by an iterative process where the first version of the tower was based on the NREL 5MW turbine [1] and the scaling method described in Chapter 2.1. However, it was decided to use a relatively shorter tower, so the tower was designed from scratch. The first version of this design was then optimised based on the loads from the aeroelastic calculation. The design was verified by doing both strength and buckling analysis.

The tower properties are summarized in Table 4.15. The resulting overall (integrated) tower mass is 628,442 kg with CM located at 47.6 m along the tower centreline above the ground. The structural damping ratio is specified to be 1% critical in all modes of the isolated tower (without the rotor-nacelle assembly mass present).

## 6.3. Description of Design Load Cases

The DTU 10MW RWT is intended for offshore operation and is therefore designed based on wind class IA according to IEC61400-1 standard [34]. The IEC61400-1 standard describes several design load cases with which a turbine design must be verified in order to withstand all load situations during its life time (20 years). Most of the design load cases except controller dependent design cases (DLC1.4, DLC2.2, DLC3.1, DLC3.2, DLC3.3) and transport, assemble, maintenance, and repair cases (DLC8) were considered in this report. Thus, the control of these events was assumed to be handled, so that the turbine should not be designed for these loads. More detailed descriptions of the design load cases are found in Appendix D. For all aeroelastic simulations HAWC2 was used. HAWC2 is an aeroelastic simulation software intended for calculating wind turbine response in the time domain developed by DTU Wind Energy [37, 38, 39]. In order to investigate the considered design load cases several assumptions were adapted as follows:

- 1) Mechanical break system was not considered for shut-down related load cases.
- 2) Shut-down situation resulting from extreme wind conditions such as the extreme operating gust (EOG) was followed during the extreme wind events.
- 3) Approximately 2 deg./sec and 5 deg./sec were considered as pitch velocity for normal and emergency shut-down case, respectively.

Table 6.4.: Natural frequency for the isolated blade

Mode	Natural frequency[Hz]	Logarithmic Damping[%]
1st flap mode	0.61	3.0
1st edge mode	0.93	3.0
2nd flap mode	1.74	8.4
2nd edge mode	2.76	8.9
3rd flap mode	3.57	17.0
1st torsion mode	5.69	20.8
4th flap mode	6.11	26.4
3rd edge mode	6.66	5.0

- 4) The generator torque was lost within 0.1sec for the grid fault load cases.
- 5) In DLC6.2, power back-up was not provided for the control and yaw system. Therefore yaw misaligned situations were considered. The wind direction was covering all azimuthal positions by an equally increase of 30 deg..

## 6.4. Aeroelastic Results

In this section, aeroelastic results are discussed. First of all natural frequencies for the isolated blade and for the whole turbine are addressed. Second, the statistic analyses are discussed. Third, the ultimate loads and fatigue loads are discussed respectively. Finally, tower clearance is addressed.

### 6.4.1. Eigenvalue Analyses

First, the blade natural frequencies were obtained from HAWC2 (see Table 6.4). Damping and logarithmic decrement values were tuned as 3% for the first blade modes. The natural frequencies and damping values for different modes of the whole turbine are addressed in Table 6.5.

### 6.4.2. Statistic Analyses

A simple wind step condition was investigated in order to verify the controller performance. Figure 6.1 presents wind steps (red line), pitch angles (black line), and generator power (blue line), respectively. It can be seen that the controller performs very well. In the next step, the statistics for DLC1.1 are investigated. The maximum, mean and minimum values from each simulation in DLC1.1 including yaw error cases are shown in Figure 6.2. In the Figure the different symbols illustrate the different load cases. For example, "○" represents the DLC1.1 without yaw error case, "△" represents the DLC1.1 with 10 deg. yaw error case, and "□" represents the DLC1.1 with -10 deg. yaw error case, respectively. The colour illustrates the different statistics as well (blue: the maximum value, red: the mean value, and black: the minimum value).

Table 6.5.: Natural frequency of the whole turbine

Mode	Natural frequency[Hz]	Logarithmic Damping[%]
1st Tower side-side mode	0.25	1.9
1st Tower side-side mode	0.25	1.9
1st fix-free mode	0.50	3.1
1st asymmetric flap with yaw	0.55	2.3
1st asymmetric flap with tilt	0.59	2.8
1st collective flap mode	0.63	3.1
1st assymetric edge1	0.92	2.9
1st assymetric edge2	0.94	3.0
2nd assymetric flap with yaw	1.38	4.8
2nd assymetric flap with tilt	1.55	6.1

where edge1: blade1 (pointing upward) is almost standstill and other two blades are assymetrically excited mode. edge2: blade2 is almost standstill and other two blade are assymetrically excited mode.

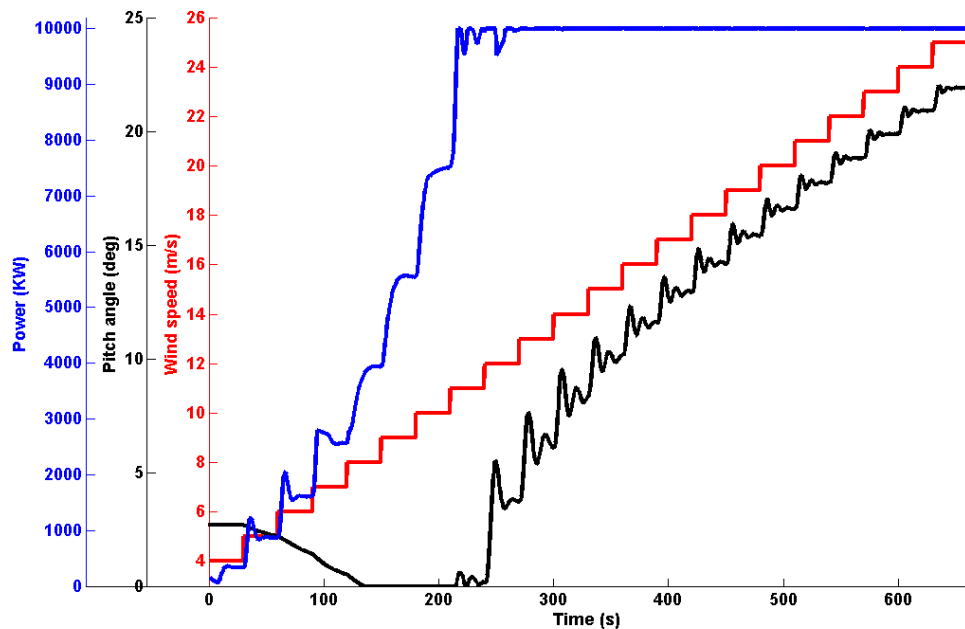


Figure 6.1.: A wind step case, red line: wind speed, black line: pitch angle, and blue line: generator power.

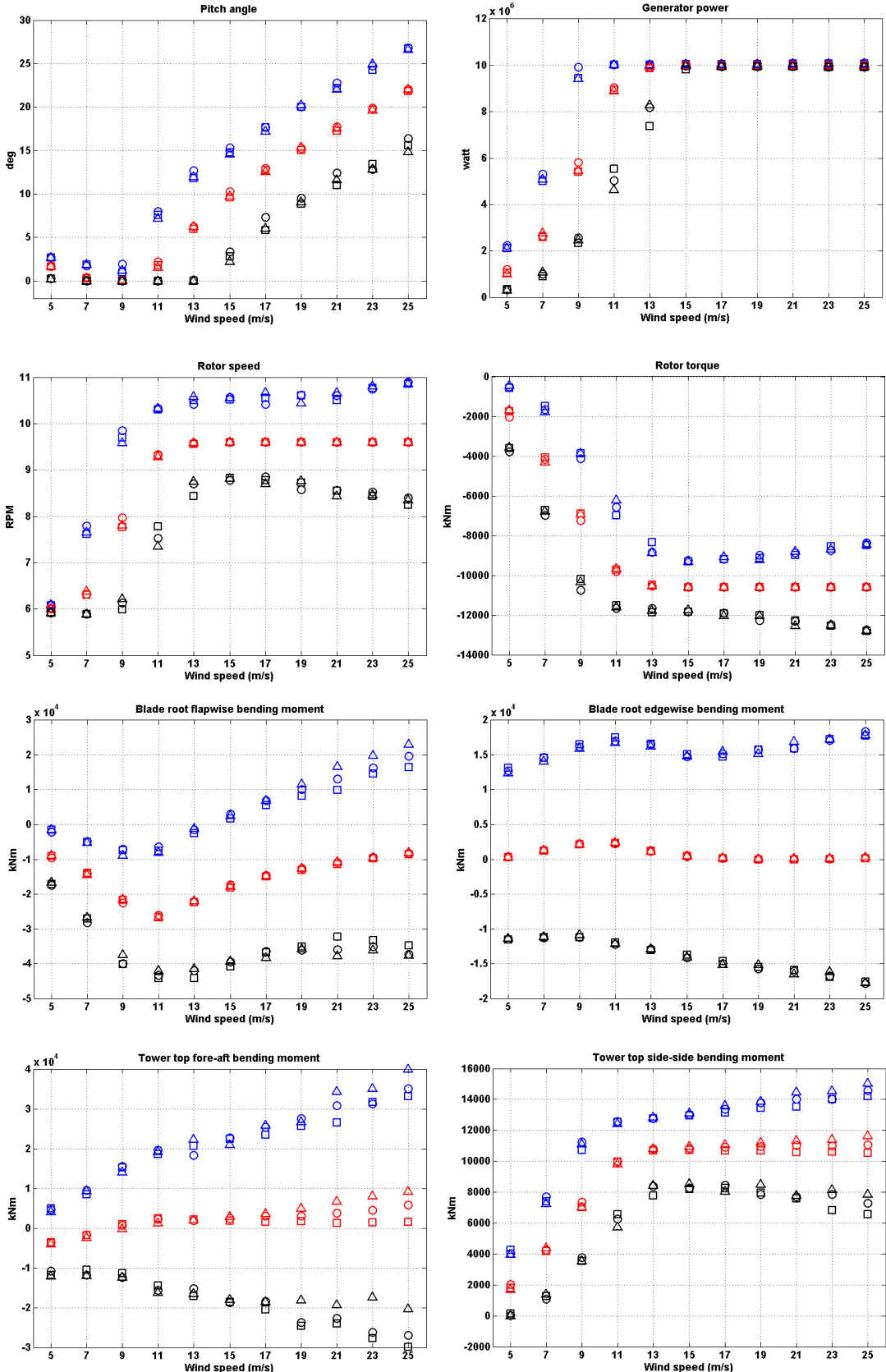


Figure 6.2.: Statistic analysis for DLC1.1: "○": 0 deg. yaw, "△": 10 deg. yaw, "□": -10 deg. yaw, blue: the maximum value, red: the mean value, and black: the minimum value .

Table 6.6.: The maximum and the minimum tower top thrust and the simultaneous tower top bending moment for the design load case 1.3.

	Tower top thrust, Fy [kN]	Simultaneous tower top bending moment, Mx [kNm]
Max	3.229e3	1.018e4
Min	-4.186e3	-1.623e4

### 6.4.3. Ultimate Load Analyses

The load carrying components of the wind turbine structures should be verified with the ultimate and fatigue strength of the structural members to demonstrate the structural integrity of a wind turbine with the appropriate safety level [34]. The ultimate loads were used in order to verify the blade and the tower design. The IEC 61400-1 Ed.3 standard recommends that the extreme values of the loading from DLC1.1 are determined using the statistical extrapolation for the 50 year recurrence period, but according to Natarajan et al. [40] traditional Gumbel method used to perform extreme load extrapolation in accordance with the IEC 61400-1 Ed.3 standard is conservative. Because of the uncertainty in the used IEC standard concerning which method to use for the extrapolation the GL approach [41] is adopted instead, which requires a partial safety factor of 1.35.

The ultimate loads on the cross-sections along the blade span and the maximum thrust and bending moment on the tower top are reported. Figure 6.3 - 6.5 show the maximum bending moment for the tower bottom fore-aft and side-side, the yaw bearing (tower top) tilt and roll, and blade root flapwise and edgewise bending moments. All values illustrated are the maximum of the absolute values from each load case. From the results it is seen that DLC1.3 is a design load case for the tower bottom fore-aft and side-side, and yaw bearing bending moments tilt and roll, respectively. Figure 6.5a shows that DLC1.3 is a design load case for the flapwise blade root bending moment as well. However, DLC2.1 is a design load case for the blade root edgewise bending moment (see Figure 6.5b). In order to verify the structural design of the composite blade, the maximum and the minimum cross-sectional loads along the span are required with which the buckling and strength analysis are performed. In Appendix E the obtained cross-sectional loads are listed. In order to verify the tower design, the maximum and the minimum thrust at tower top and the tower top moment, which occurred simultaneously when the maximum and the minimum tower top thrust occurred, should be reported. Table 6.6 shows the maximum and the minimum tower top thrust and the simultaneous tower top bending moments.

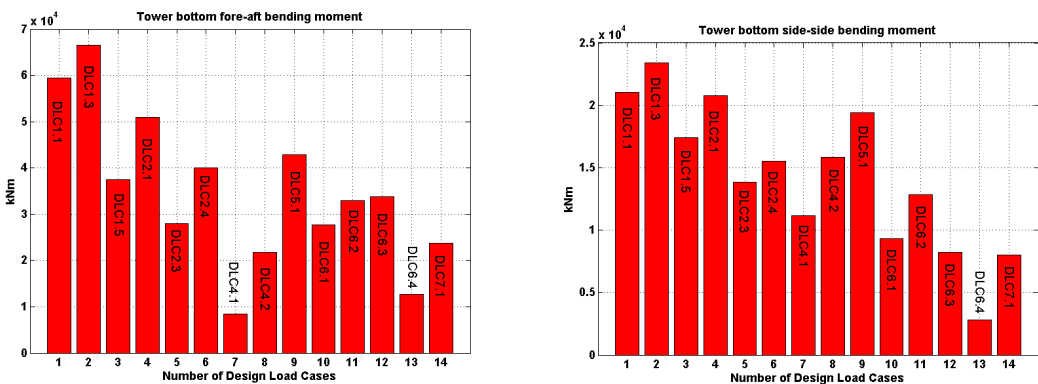
### 6.4.4. Fatigue Load Analyses

The IEC 61400-1 Ed.3 standard [34] suggests DLC1.2, DLC2.4, DLC3.1, DLC4.1, and DLC6.4 for the fatigue analyses such as 1Hz equivalent fatigue loads, the life time equivalent fatigue loads. In this report, the life time equivalent fatigue loads for the tower, the shaft and the blade were investigated. Among the suggested design load cases for the fatigue analyses DLC1.2 is the most frequent design load condition during the life time.

Table 6.7.: The tower clearance.

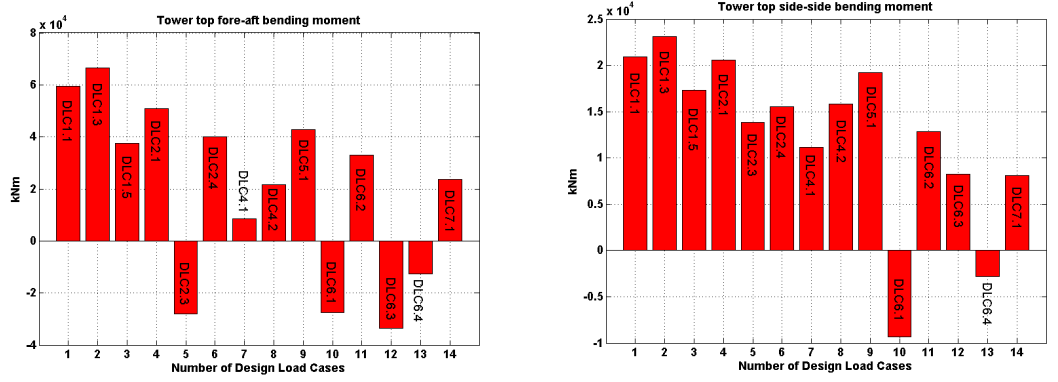
Design Load Case	Blade tip deflection in the hub coordinate system[m]	Margin [m(%)]
------------------	--	---------------

DLC 1.1	11.5	6.76 (37%)
DLC 1.3	12.4	5.86 (32%)
DLC 1.5	10.5	7.76 (42%)
DLC 2.1	8.97	9.29 (51%)
DLC 2.3	6.56	11.7 (64%)
DLC 2.4	7.86	10.4 (57%)
DLC 4.1	5.28	12.98 (71%)
DLC 4.2	7.52	10.74 (59%)
DLC 5.1	10.1	8.16 (45%)
DLC 6.1	1.23	17.03 (93%)
DLC 6.2	1.45	16.81 (92%)
DLC 6.3	1.23	17.03 (93%)
DLC 6.4	0.27	17.99 (99%)
DLC 7.1	1.06	17.2 (94%)



(a) Tower bottom fore-aft bending moment      (b) Tower bottom side-side bending moment

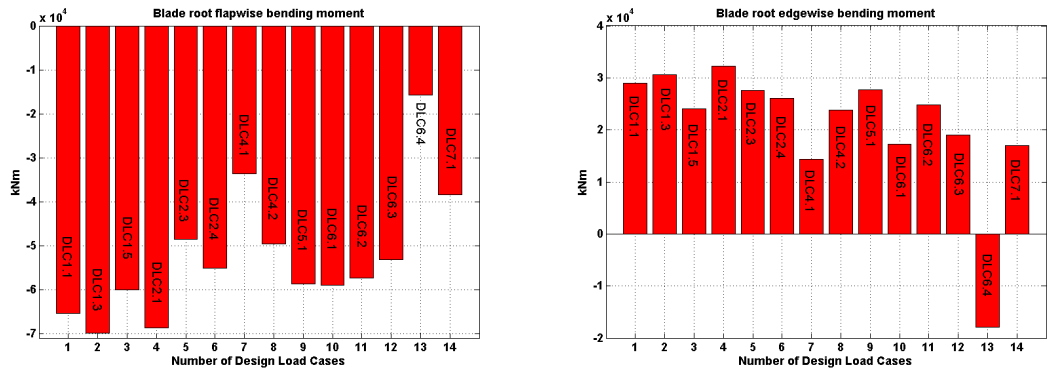
Figure 6.3.: Tower bottom bending moments



(a) Tower top fore-aft bending moment

(b) Tower top side-side bending moment

Figure 6.4.: Tower top (yaw bearing) bending moments



(a) Blade root flapwise bending moment

(b) Blade root edgewise bending moment

Figure 6.5.: Blade root bending moments

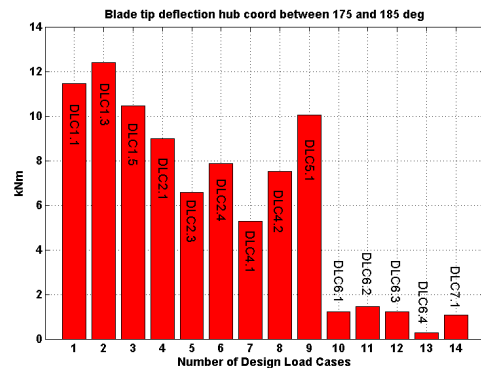


Figure 6.6.: Blade tip deflection measured at hub coordinate system between 175 deg. and 185 deg. in azimuth (blade is pointing upward at 0 deg. in azimuth).

Table 6.8.: The distributed hours during the life time for DLC1.1

Wind speed (m/s)	Hours for each condition			Hours (sum of 6 seeds)
	-10 deg. yaw	0 deg. yaw	10 deg. yaw	
4 - 6	6433.7	12867.4	6433.7	25734.7
6 - 8	6382.2	12764.3	6382.2	25528.7
8 - 10	6521.6	13043.3	6521.6	26086.5
10 - 12	5939.9	11879.8	5939.9	23759.5
12 - 14	4911.8	9823.5	4911.8	19647.0
14 - 16	3725.8	7451.5	3725.8	14903.0
16 - 18	2609.0	5217.9	2609.0	10435.9
18 - 20	1693.6	3387.3	1693.6	6774.6
20 - 22	1022.2	2044.4	1022.2	4088.9
22 - 24	574.8	1149.7	574.8	2299.3
24 - 26	301.7	603.3	301.7	1206.6

Therefore only DLC1.2 including yaw misaligned conditions was considered. The fatigue loads are based on  $11 \times 600$ s time series with different turbulent seeds and yaw misalignments (in total 33 load cases are considered per each turbulence seed), 1 for every 2 m/s from 5 to 25 m/s. The fatigue loads are given as a damage equivalent load (DEL) of  $10^7$  cycles, Nref, corresponding to 20 years life time damage, based on the Palmgren-Miner's summation rule.

$$DEL = \left( \frac{1}{N_{\text{ref}}} \sum_{1..n_{\text{sim}}}^i \left( \frac{T_{\text{life},i}}{T_{\text{sim},i}} \sum_{1..n_k}^k N_{i,k} S_{i,k}^m \right) \right)^{1/m} \quad (6.1)$$

where  $N_{i,k}$  are the number of cycles at load range  $S_{i,k}$  determined with rainflow counting.  $T_{\text{life},i}$  is the period that the turbine will be running at the given wind speed of the simulation time series number  $i$  in accordance with Table 6.8. For the blade loads a Wöhler exponent of  $m = 10$  has been used. Other components are assumed to be steel,  $m = 3$ .

Figure 6.7 - 6.9 show the life time fatigue loads for the tower bottom bending moments ( $m = 3$ ), the shaft bending moments ( $m = 3$ ), and the blade root bending moments ( $m = 10$ ), respectively.

#### 6.4.5. Tower Clearance

In this section, the tower clearance is investigated. The measured tower clearance windows are -5 deg. and 5 deg. azimuth from the tower center, i.e. 175 deg. and 185 deg. azimuth where blade is pointing upward at 0 deg. azimuth. Figure 6.10 shows a sketch of tower clearance of the DTU 10MW RWT. The tower clearance including tilt, cone, and prebend is without loads 18.26m. Two different approaches were adapted: First, the relevant safety

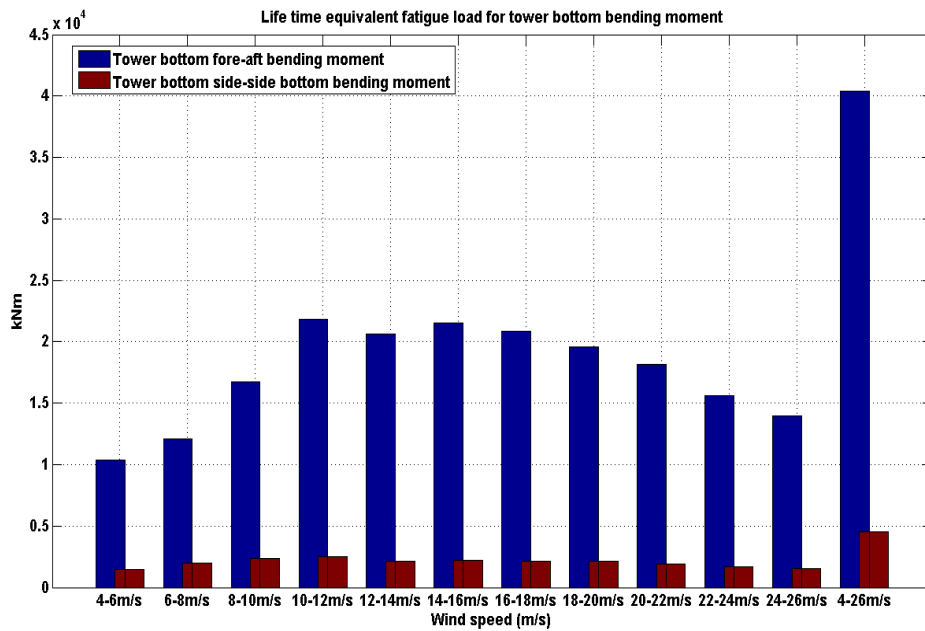


Figure 6.7.: Life time equivalent fatigue loads for the tower bottom bending moment: blue: tower bottom fore-aft bending moment, red: tower bottom side-side bending moment.

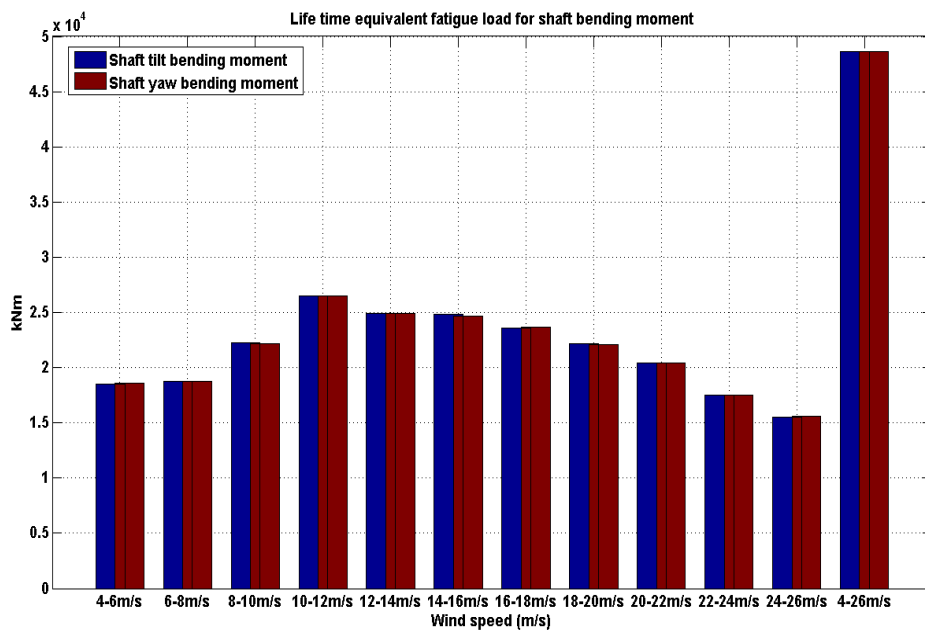


Figure 6.8.: Life time equivalent fatigue loads for the shaft bending moment: blue: shaft tilt bending moment, red: shaft yaw bending moment.

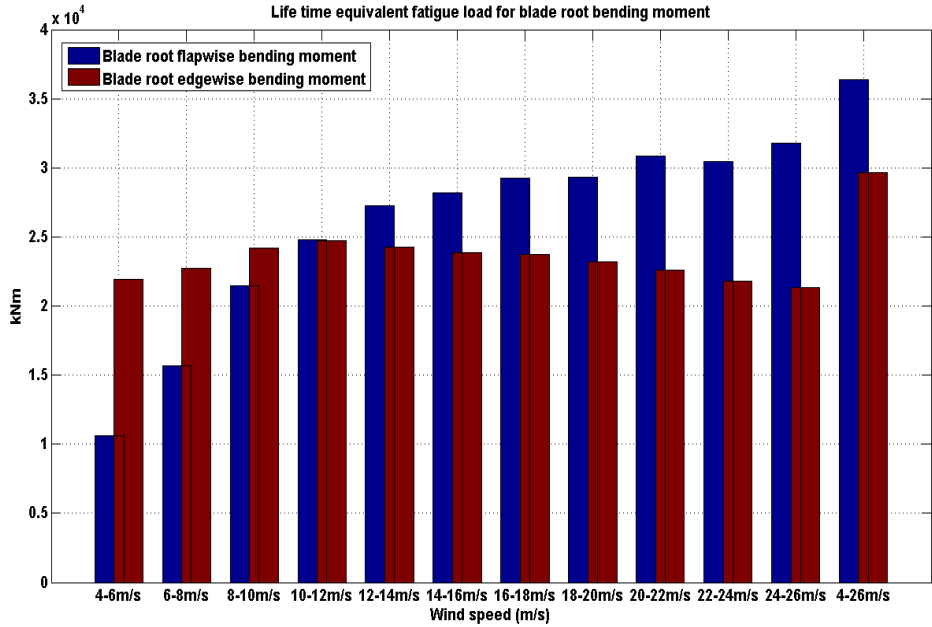


Figure 6.9.: Life time equivalent fatigue loads for the blade root bending moment: blue: blade root flapwise bending moment, red: blade root edgewise bending moment.

factor with respect to the considered load case was multiplied with the maximum blade deflection toward the tower. If there were still clearance between the blade and the tower then it was assumed that the tower clearance was sufficient [34]. Second, the minimum clearance between the blade and the tower had to be larger than 30% for the operation case (DLC1.X to DLC5.X) and 5% for the parked case (6.X and 7.X) where the safety factors were considered as well [41]. Figure 6.6 shows the maximum tip deflection including safety factor. DLC1.3 case provide the largest blade tip deflection which is 12.4m. Therefore there is 5.86m clearance which is almost 32 % margin (see Table 6.7). There is enough tower clearance for all load cases considered. So, it can be concluded that the tower clearance of the DTU 10MW RWT is safistied for two different requirements.

#### 6.4.6. Vibration Issue

The DTU 10MW RWT shows edgewise vibrations for both an operational and a standstill condition. The standstill vibration occurs when the inflow comes from either 30 deg. or -30 deg. for load cases DLC6.2 and DLC7.1. Figure 6.11 shows the blade root edgewise bending moment when the wind comes from 30 deg. and -30 deg., respectively.

One way to resolve the edgewise vibration is to change the structural pitch resulting in the vibration direction changing. However, this requires a new blade structural design. In order to resolve the vibration problem without a change in the design, different pitch angle sequences were considered which lead to the vibration direction changing resulting

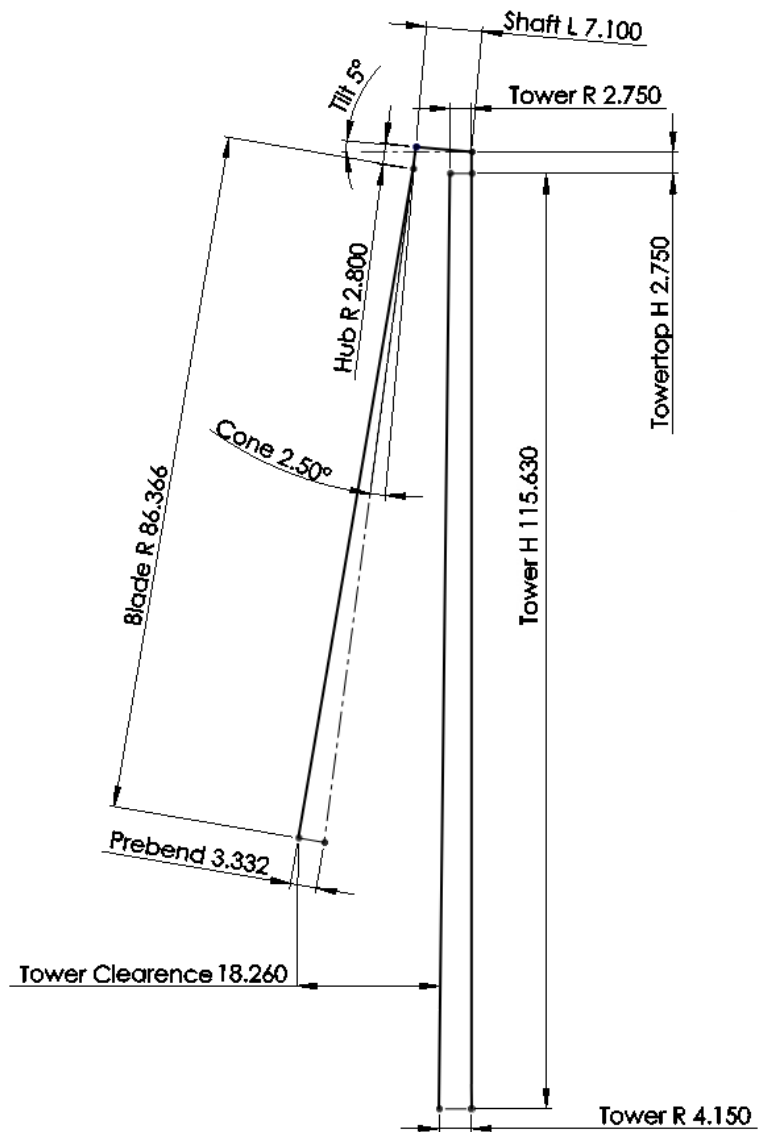
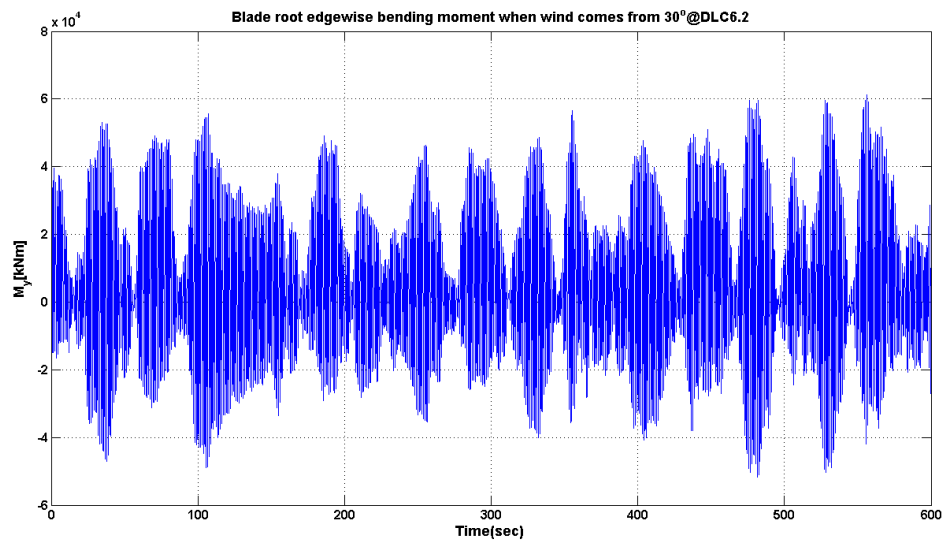
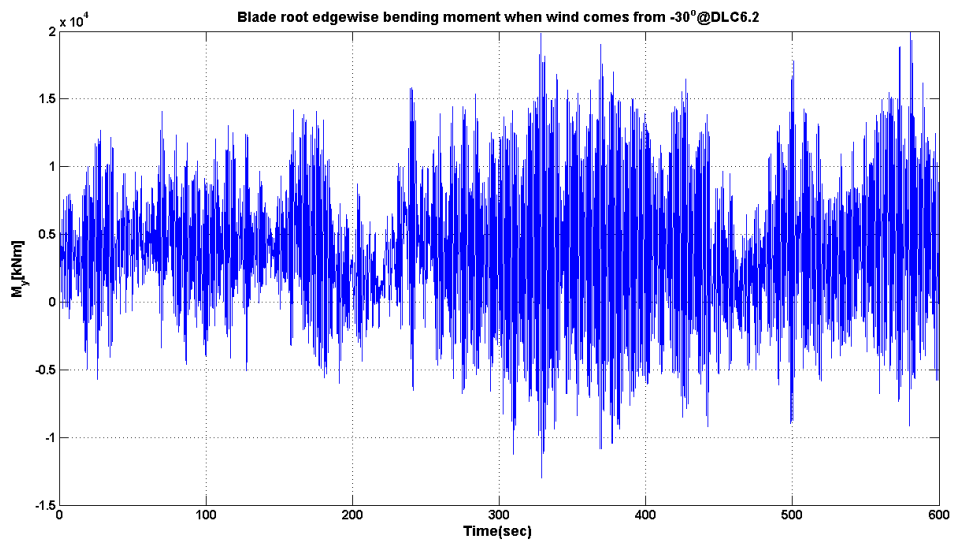


Figure 6.10.: A sketch of tower clearance.



(a) Blade root edgewise moment (wind direction: 30 deg.)

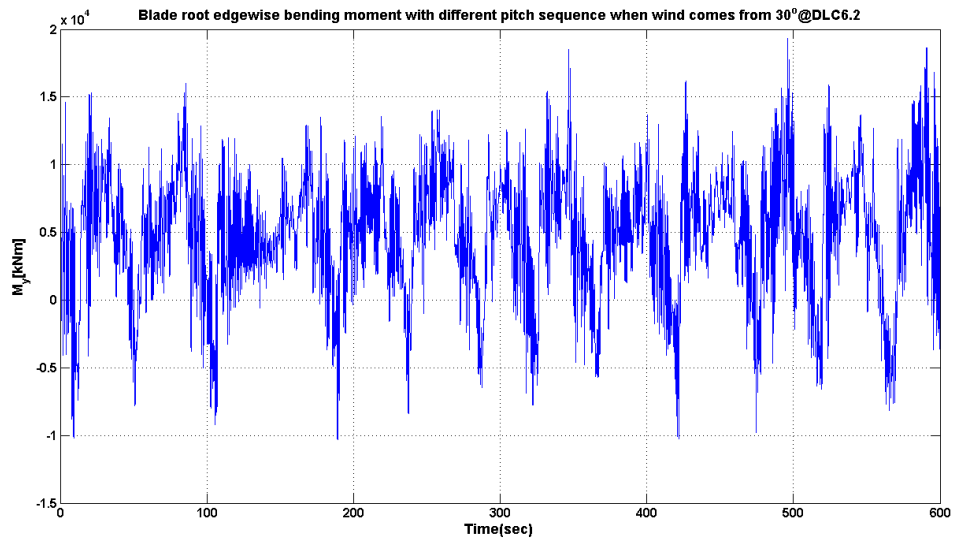


(b) Blade root edgewise moment (wind direction: -30 deg.)

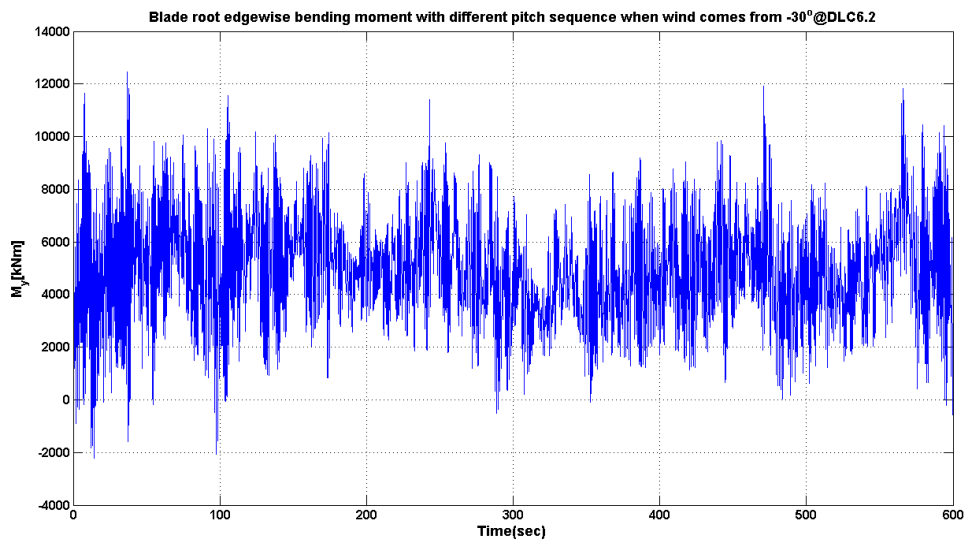
Figure 6.11.: Blade root edgewise bending moments when wind comes from  $\pm 30$  deg..

in aerodynamic damping improvements. The considered pitch sequence in this report is 70-90-90 (i.e. 70 deg. for blade 1 where blade 1 is pointing upwards, 90 deg. for blade 2, and 90 deg. for blade 3), 90-70-90, or 90-90-70. All possible combinations of pitch sequences had to be considered since the rotor was idling. It is shown in Figure 6.12 that the edgewise vibration problem can be remedied using this pitch strategy.

At an extreme turbulence model condition (DLC1.3) the turbine shows an edgewise vibration issue (see Figure 6.13). This issue can be solved by tuning natural frequencies and increasing the aerodynamic damping of the blade. This issue has not been addressed in this report and will be subject to further investigations in future work.

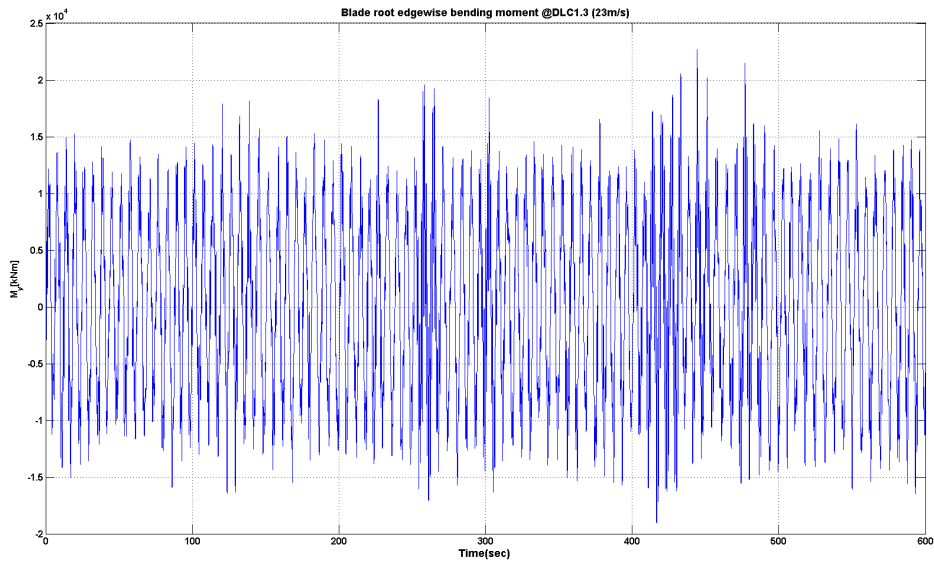


(a) Blade root edgewise moment with the different pitch sequence (wind direction: 30 deg.)

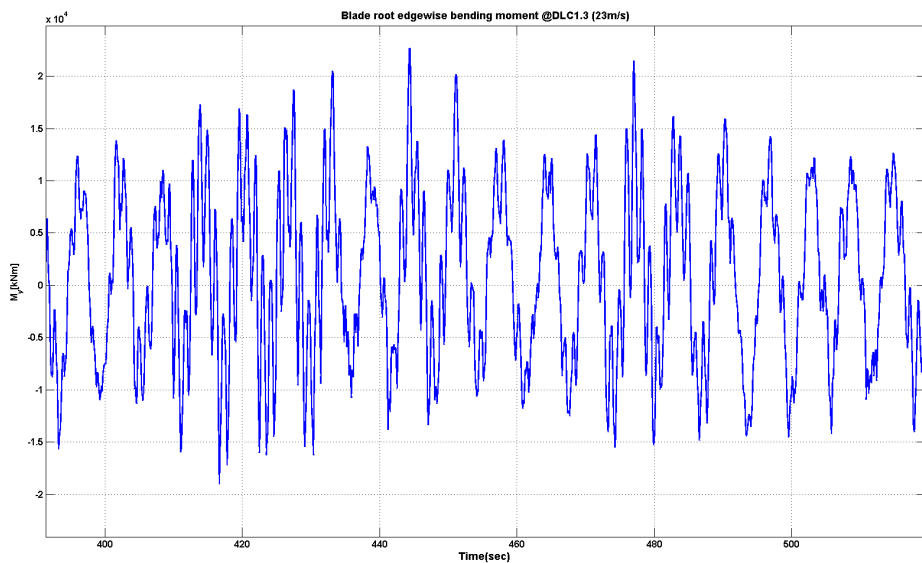


(b) Blade root edgewise moment with the different pitch sequence (wind direction: -30 deg.)

Figure 6.12.: Blade root edgewise bending moments when wind comes from  $\pm 30$  deg. with using the different pitch setup.



(a) Blade root edgewise moment at DLC1.3 (wind speed: 23m/s)



(b) Zoomed in blade root edgewise moment at DLC1.3 (wind speed: 23m/s)

Figure 6.13.: An edgewise vibration from an extreme turbulence wind condition.

#### **6.4.7. Stability Investigation for Run-Away Situation**

The analysis is performed by simulating the rotor without generator torque in a run-away situation where the rotor reaches its terminal speed for the given wind speed and pitch angle. The terminal rotor speed is the speed at which its aerodynamic torque for a certain constant uniform wind speed becomes zero due to a balance between negative torque from the outer part of the blade at negative AOAs and positive torque from the inner part. Besides that this simulated run-away is a more realistic scenario where flutter may occur, a big advantage of this procedure for bringing the blade to flutter in attached flow is that the rotor speed can be controlled by the wind speed.

In the run-away situation, the response of the freely rotating rotor is simulated in HAWC2 (with rigid dummy shaft, drivetrain, and tower structures) for pitch angles equal to zero and the wind speed is initial set to 4.5 m/s. The upper plot of Figure 6.14 shows that the rotor reaches a terminal speed of around 8 rpm without any instability occurring. After 250 s the wind speed is increased from 4.5 m/s to 14 m/s over 1500 s. Note that the rotor speeds at increasing wind speed are not identical to terminal rotor speeds, because the rotor mass is being accelerated in the process, which requires slightly positive aerodynamic torque. A combination of large AOA variations and flapwise blade vibrations usually indicates a flutter motion of the blade. However the simulation shows a high content of edgewise vibration which is significantly more pronounced compared to the flapwise and beside that the AOA variations are not that severe. The edgewise vibration is being build up slowly and thus has only a slightly negative aeroelastic damping.

The middle plot of Figure 6.14 shows that the amplitude of the AOA, at an aerodynamic calculation point at blade radius 80 m, and the flapwise blade tip deflection are increased in a self-induced vibration.

The lower plot of Figure 6.14 shows the edgewise and flapwise tip deflections. It can be seen that the edgewise vibrations are dominating and that the instability is not flutter. The frequency of the oscillations is 0.94 Hz, which is close the 1st edgewise mode of the blade.

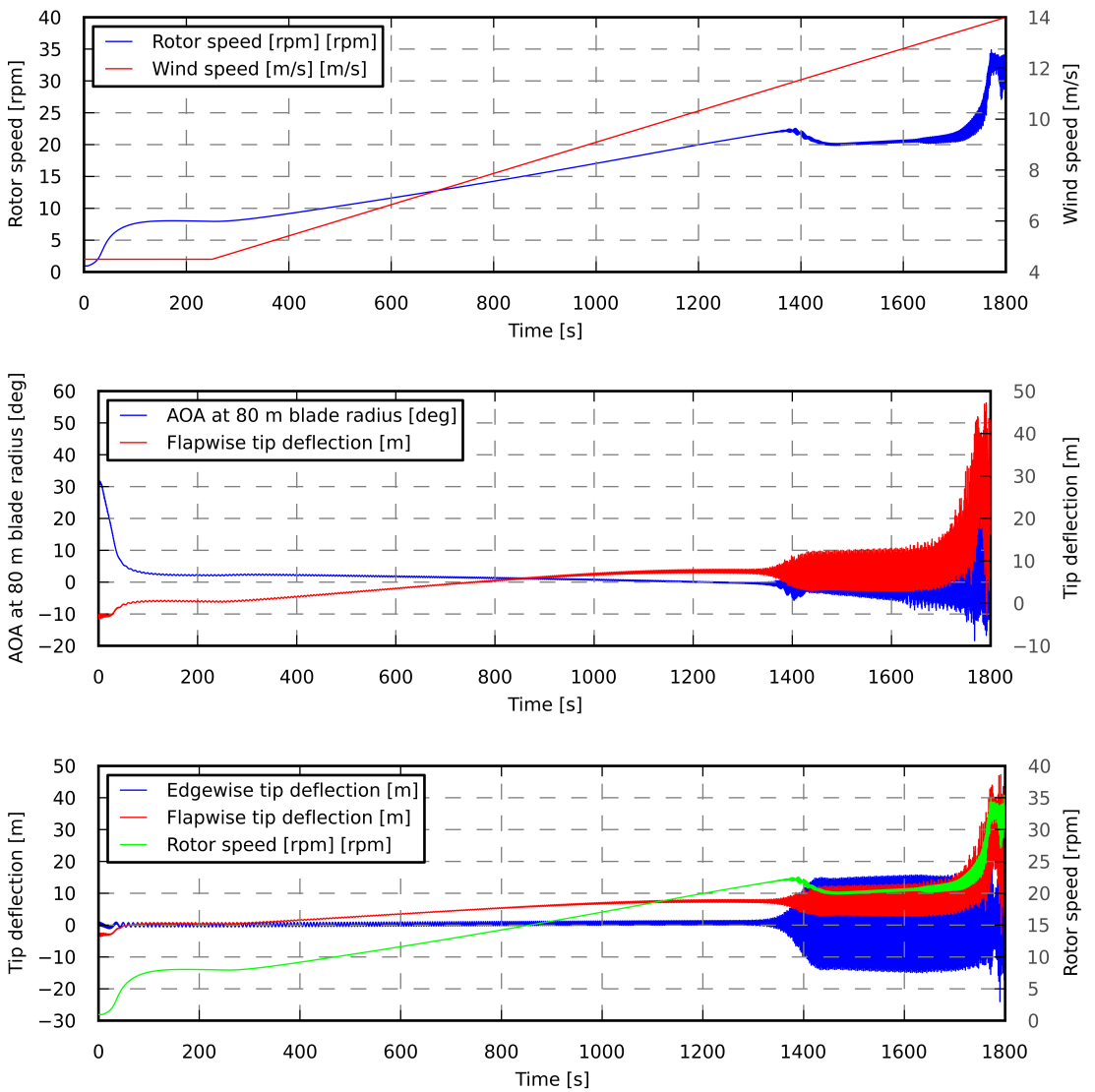


Figure 6.14.: Time series from run-away HAWC2 simulation. The initial speed is 4.5 m/s. The dominating edgewise vibration indicate a non-flutter like mode.



## 7. Conclusions

As part of the Light Rotor project, which is an Energy Development and Demonstration Project (EUDP project) supported by the Danish Energy Agency in a collaboration between the Wind Energy Department at the Technical University of Denmark and Vestas Wind Systems, a 10 MW reference wind turbine was designed, so that future designs can be benchmarked against this design. The scope of the design was therefore neither to develop the lightest nor the best performing rotor or wind turbine, but to establish a reasonable design to check computational tools and design methods in a context, which was consistent both for low fidelity models and for high fidelity models. The 10 MW wind turbine is called "DTU 10 MW Reference Wind Turbine" or in short "DTU 10MW RWT".

In the design of the wind turbine several issues were identified as challenges representative for the design of large wind turbines. Among these issues, vibrations in stand still was observed both for wind directions corresponding to approximately +/-90 degrees angle of attack and approximately 30 degrees angle of attack. The turbine did not show severe problems, but there was a trend towards rather low damping of the blades for this event. Also, in normal operation at the higher wind speeds edgewise vibrations were observed. The dynamics were not severe and was not an instability, but it showed that the blades were rather low damped. Finally, the aerodynamic airfoil characteristics at these Reynolds numbers in the order of 10 million were uncertain, in that no wind tunnel tests existed for these airfoils at these Reynolds numbers and only a few wind tunnel tests for airfoils exist at all for airfoils at these Reynolds numbers. That was the reason for using computational tools to predict the performance. However, it was observed, that the transition modeling from laminar to turbulent flow between different codes did not agree on the performance and therefore the overall aerodynamic performance was somewhat different depending on the computational tool and the corresponding transition modeling from laminar to turbulent flow.

The DTU 10 MW RWT is a wind turbine that is designed rather light weight and is an attempt to design a wind turbine that is on the limit of maximum stress and strain values. However, it is designed using traditional techniques and design methods and also traditional layout such as the specific power, which is the ratio between the rated power and the swept rotor area. It is the hope that this rotor and the entire wind turbine can serve as a basis to develop simulation tools and develop new designs and this way pave the way to the design of even more reliable, efficient and cost effective wind turbines in the future.



## Acknowledgements

This project was funded partly by the Danish Energy Agency by the project EUDP2010-I Light Rotor, and partly by eigen funding from the project partners. We would like to acknowledge the persons in the Aeroelastic Design Section and the Structures Section in the DTU Wind Energy Department, where many discussions have taken place. Especially, Peter B. Andersen, Mac Gaunaa, Torben J. Larsen, Anders M. Hansen and José Blasques have given important input to the design process. Also, would like to acknowledge Tomas Vronsky and Jens-Jakob Wedel Heinen (Vestas). Finally, we acknowledge Takis Chaviaropoulos (CRES, Greece) and Ervin Bossanyi (GL-GarradHassan), who are part of the EU project InnWind.



## Bibliography

- [1] J. Jonkman, S. Butterfield, W. Musial, and G. Scott. Definition of a 5-MW reference wind turbine for offshore system development. Technical Report NREL/TP-500-38060, NREL, 2009.
- [2] Chaviaropoulos, P.K. Similarity rules for wind turbine up-scalingl. Online Documentation, 2006.
- [3] Anders Bjørk. Coordinates and calculations for the ffa-w1-xxx, ffa-w2-xxx and ffa-w3-xxx series of airfoils for horizontal axis wind turbines. Technical Report FFA TN 1990-15, FFA, Stockholm, Sweden, 1990.
- [4] Peter Fuglsang, Ioannis Antoniou, Kristian S. Dahl, and Helge Aa. Madsen. Wind tunnel tests of the ffa-w3-241, ffa-w3-301 and naca 63-430 airfoils. Technical Report Risø-R-1041(EN), ISBN 87-550-2377-0, Risø National Laboratory, Roskilde, 1998.
- [5] Jess A. Michelsen. Basis3D—a platform for development of multiblock PDE solvers. Technical Report AFM 92-05, Technical University of Denmark, 1992.
- [6] Jess A. Michelsen. Block structured multigrid solution of 2D and 3D elliptic PDEs. Technical Report AFM 94-06, Technical University of Denmark, 1994.
- [7] Niels N. Sørensen. General purpose flow solver applied to flow over hills. Technical Report Risø-R-827(EN), Risoe National Laboratory, 1995.
- [8] F. R. Menter. Zonal two-equation  $k - \omega$  models for aerodynamic flows. *AIAA paper 93-2906*, 1993.
- [9] F.R. Menter, R.B. Langtry, S.R. Likki, Y.B. Suzen, P.G. Huang, , and S. Volker. A correlation-based transition model using local variables, part I - model formulation. In *Proceedings of ASME Turbo Expo 2004, Power for Land, Sea, and Air*, number ASME. GT2004-53452, Vienna, Austria, June 14-17 2004.
- [10] Niels N. Sørensen. CFD modelling of laminar-turbulent transition for airfoils and rotors using the  $\gamma-Re_\theta$  model. *Wind Energy*, DOI 10.1002/we.325, 2009.
- [11] Niels N. Sørensen. HypGrid2D—a 2-D mesh generator. Technical report, Risø-R-1035(EN), Risoe National Laboratory, 1998.
- [12] J. Johansen, N. N. Sørensen, and R. Mikkelsen. Rotoraerodynamik (in danish). Technical report, Risø National Laboratory, Roskilde, Denmark, 2004. in "Research in aeroelasticity", ed. C.Bak, Risø-R-1434(DA).
- [13] C. Bak, J. Johansen, and P. B. Andersen. Three-dimensional corrections of airfoil characteristics based on pressure distributions. In *Proc. European Wind Energy Conference and Exhibition (EWEC), 27. Feb. - 2. Mar. 2006, Athens, Greece*, 2006.

- [14] Jørgen Thirstrup Petersen, Helge Aagaard Madsen, Anders Bjørck, Peder Enevoldsen, Stig Øye, Hans Ganander, and Danny Winkelhaar. Prediction of dynamic loads and induced vibrations in stall. Technical report, Risø-R-1045(EN), Risoe National Laboratory, Roskilde, Denmark, 1998.
- [15] C. Bak, N. Troldborg, and H. A. Madsen. Dan-aero mw: Measured airfoil characteristics for a mw rotor in atmospheric conditions. In *Scientific Proceedings. EWEA, 2011, Brussel, Belgium*, 2011.
- [16] K. Fuglsang, P.; Thomsen. Site-specific design optimization of 1.5-2.0 mw wind turbines. *J. Solar Energy Eng.*, (123):296–303, 2001.
- [17] M. Drela. Xfoil: An analysis and design system for low reynolds number airfoils. In *Conference on Low Reynolds Number Airfoil Aerodynamics, University of Notre Dame*, 1989.
- [18] Morten Hansen. Aeroelastic properties of backward swept blades. In *Aerospace Sciences Meetings*, pages –. American Institute of Aeronautics and Astronautics, January 2011. doi: 10.2514/6.2011-260. URL <http://dx.doi.org/10.2514/6.2011-260>.
- [19] Niels N. Sørensen. Rotor computations using a 'steady state' moving mesh. IEA Joint Action Committee on aerodynamics. Annex XI and 20. Aero experts meeting, Pamplona (ES), 25-26 May 2005.
- [20] Python programming language – official website. URL <http://www.python.org>.
- [21] Pointwise. URL <http://pointwise.com>.
- [22] C. C. Chamis. Simplified composite micromechanics equations for hygral, thermal, and mechanical properties. *Sampe Quarterly*, 15:14–23, 1984.
- [23] M. Hinton, P. Soden, and Abdul-Salam Kaddour. *Failure Criteria in Fibre-Reinforced-Polymer Composites*. Elsevier, 2004.
- [24] Michael F. Ashby. *Materials Selection in Mechanical Design*. Elsevier, forth edition, 2011.
- [25] K. E. Easterling, R. Harrysson, L. J. Gibson, and M. F. Ashby. On the mechanics of balsa and other woods. *Proceedings of the Royal Society of London. A. Mathematical and Physical Sciences*, 383(1784):31–41, 1982. doi: 10.1098/rspa.1982.0118.
- [26] R. P. L. Nijssen, D. R. V. Van Delft, P. A. Joosse, A. M. Van Wingerde, C. W. Kensche, T. P. Philippidis, P. Brøndsted, and A. G. Dutton. OPTIMAT BLADES - optimal and reliable use of composite materials for wind turbines. In *Proc. 14th International Conference on Composite Materials (ICCM-14), 14.-18. Jul.*, San Diego, California, 2003.
- [27] DOE / MSU composite material fatigue database, mar 2010. Version 19.
- [28] Dassault Systèmes. Abaqus 6.11: Abaqus analysis user's manual. Online Documentation, 2011.

- [29] José Pedro Blasques. User's manual for BECAS - a cross section analysis tool for anisotropic and inhomogeneous beam sections of arbitrary geometry. Technical Report Risø-R-1785(EN), Risø DTU, National Laboratory for Sustainable Energy, 2011.
- [30] José Pedro Blasques and Mathias Stolpe. Multi-material topology optimization of laminated composite beam cross sections. *Composite Structures*, 94(11):3278 – 3289, 2012. ISSN 0263-8223. doi: 10.1016/j.compstruct.2012.05.002.
- [31] Germanischer Lloyd. Guideline for the certification of wind turbines, 2010.
- [32] Morten Hartvig Hansen and Lars Christian Henriksen. Basic DTU Wind Energy controller. Technical Report DTU Wind Energy E-0018, Technical University of Denmark, 2013.
- [33] M. H. Hansen, A. H., T. J. Larsen, S. Øye, P. Sørensen, and P. Fuglsang. Control design for a pitch-regulated, variable speed wind turbine. Technical Report Risø-R-1500(EN), Risø National Laboratory, 2005.
- [34] IEC. IEC 61400-1: Wind Turbines - Part 1: Design Requirements. Standard, aug 2005.
- [35] A. B Andersen and A Winnemuller. Selecting the Optimum Drive Train: Finding the optimal solution for drivetrains seen from the perspective of the wind turbine owner. In Peter Tavner, editor, *EWEA 2013 Scientific Proceedings*, pages 16–18. EWEA, February 2013.
- [36] S Schmidt and A Vath. Comparison of Existing Medium-speed Drive Train: Concepts with a differential gearbox approach. In Peter Tavner, editor, *EWEA 2012 Scientific Proceedings*, pages 117–120. EWEA, 2012.
- [37] T. J. Larsen and A. M. Hansen. How 2 hawc2, the user's manual. Technical Report Risø -R-1597(ver. 4-3)(EN), Risø National Laboratory, 2012.
- [38] T. J. Larsen, H. A. Madsen, G Larsen, and Hansen K. S. Validation of the dynamic wake meander model for loads and power production in the egmond and zee wind farm. *Wind Energy*, Accepted, 2012.
- [39] T. Kim, A. M. Hansen, and K. Branner. Development of an anisotropic beam finite element for composite wind turbine blades in multibody system. *Renewable Energy*, 59:178–183, 2013.
- [40] A. Natarajan and W. E. Holley. Statistical extreme load extrapolation with quadratic distortions for wind turbine. *Journal of Solar Energy Engineering*, 130(3):031017–1 – 031017–7, 2008. doi: 10.1115/1.2931513.
- [41] Germanischer Lloyd. Guideline for the Certification of Wind Turbines. Standard, July 2010.



## Appendix A.

### Cubic Splines Defining Blade Properties

Splines are functions defined piecewise by polynomials (see Figure A.1). At the intersections of two polynomial pieces, continuity conditions (e.g. n-times continuously differentiable) are usually assigned in order to achieve a smooth curve.

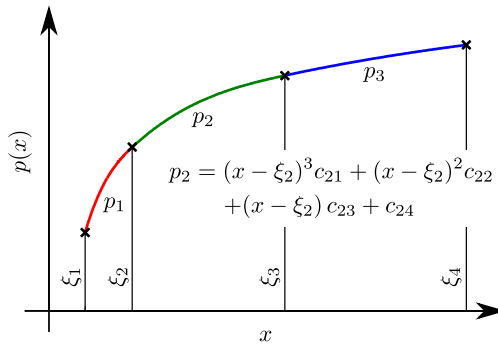


Figure A.1.: Cubic spline.

A spline  $p(x)$  can be described in terms of its breaks  $\xi_1, \xi_2, \dots, \xi_l$  and its polynomial coefficients  $c_{ji}$ :

$$p_j(x) = \sum_{i=1}^k (x - \xi_j)^{k-i} c_{ji} \quad j = 1, 2, \dots, l \quad , \quad (\text{A.1})$$

where  $l$  is the number of polynomial pieces and  $k$  is the number of coefficients in each polynomial ( $k = 4$  for a cubic spline). The polynomial  $p_j(x)$  describes the spline in the interval  $\xi_j \leq x \leq \xi_{j+1}$ .

In this report, cubic splines ( $k = 4$ ) have been used to define various blade properties as a function of the radial position  $r$ . The tables in this Appendix list the breaks and polynomial coefficients of the splines. At breaks all spline curves are either once or twice continuously differentiable. Note that the splines always pass through the points  $(\xi_j, c_{j4})$  for  $j = 1, 2, \dots, l$ .

#### Putting together splines in Matlab

The example below demonstrates how a spline defined by its breaks and coefficients can be put together in Matlab<sup>1</sup> using the `ppmak` command.

---

<sup>1</sup><http://www.mathworks.com>

```
breaks = [2.8000 4.8000 18.8310 27.1510 37.4240 63.6150 89.1660];  
  
coefs = [  
    0.00000000E+000 0.00000000E+000 0.00000000E+000 1.00000000E+000;  
    1.62937798E-004 -4.63665745E-003 0.00000000E+000 1.00000000E+000;  
   -6.85077910E-005 2.22188329E-003 -3.38816961E-002 5.37263996E-001;  
   -1.27824823E-005 5.11928831E-004 -1.11363793E-002 3.69716661E-001;  
   -7.36208618E-007 1.17985509E-004 -4.66526923E-003 2.95480597E-001;  
    0.00000000E+000 0.00000000E+000 0.00000000E+000 2.41000000E-001];  
  
rel_thick_spline = ppmak(breaks,coefs,1);
```

Table A.1.: Breaks and coefficients of cubic spline describing the chord length as a function of the radial coordinate (both in meters).

	$\xi_j$	$\xi_{j+1}$	$c_{j1}$	$c_{j2}$	$c_{j3}$	$c_{j4}$
j=1	2.8000	8.1960	0.00000000E+00	0.00000000E+00	0.00000000E+00	5.38000000E+00
j=2	8.1960	19.9548	-4.61301443E-04	1.04228497E-02	0.00000000E+00	5.38000000E+00
j=3	19.9548	28.0124	9.54064544E-05	-5.85020456E-03	5.37688193E-02	6.07113924E+00
j=4	28.0124	38.2220	7.94309215E-05	-3.54396342E-03	-2.19256287E-02	6.17447367E+00
j=5	38.2220	55.0271	2.42467032E-05	-1.11108961E-03	-6.94518582E-02	5.66574440E+00
j=6	55.0271	70.0576	8.59761392E-06	1.11315203E-04	-8.62531671E-02	4.29988830E+00
j=7	70.0576	78.1586	4.71207167E-06	4.98994511E-04	-7.70799070E-02	3.05780226E+00
j=8	78.1586	85.0000	-4.39083118E-04	6.13511989E-04	-6.80674918E-02	2.46863016E+00
j=9	85.0000	86.2521	-1.32866948E-03	-8.39831774E-03	-1.21326462E-01	1.89106967E+00
j=10	86.2521	88.6595	-1.47600180E-02	-1.33891816E-02	-1.48606495E-01	1.72338280E+00
j=11	88.6595	88.9861	-6.79818589E+00	-1.19989176E-01	-4.69702133E-01	1.08209177E+00
j=12	88.9861	89.1660	1.04359293E+01	-6.78085172E+00	-2.72351677E+00	6.79055450E-01

Table A.2.: Breaks and coefficients of cubic spline describing the relative thickness (dimensionless) as a function of the radial coordinate (in meters).

	$\xi_j$	$\xi_{j+1}$	$c_{j1}$	$c_{j2}$	$c_{j3}$	$c_{j4}$
j=1	2.8000	4.8000	0.00000000E+00	0.00000000E+00	0.00000000E+00	1.00000000E+00
j=2	4.8000	18.8310	1.63195479E-04	-4.64026965E-03	0.00000000E+00	1.00000000E+00
j=3	18.8310	27.1510	-6.94374457E-05	2.22911763E-03	-3.38308740E-02	5.37264647E-01
j=4	27.1510	37.4240	-1.19564154E-05	4.95958990E-04	-1.11582365E-02	3.70105515E-01
j=5	37.4240	63.6150	-9.34760029E-07	1.27474224E-04	-4.75370706E-03	2.94855128E-01
j=6	63.6150	89.1660	0.00000000E+00	0.00000000E+00	0.00000000E+00	2.41000000E-01

Table A.3.: Breaks and coefficients of cubic spline describing the twist angle (in degree) as a function of the radial coordinate (in meters).

	$\xi_j$	$\xi_{j+1}$	$c_{j1}$	$c_{j2}$	$c_{j3}$	$c_{j4}$
j=1	2.8000	9.1190	0.00000000E+00	0.00000000E+00	0.00000000E+00	1.45000000E+01
j=2	9.1190	15.5543	-1.94790140E-03	-1.76633017E-02	0.00000000E+00	1.45000000E+01
j=3	15.5543	21.3482	5.39990815E-03	-5.52692913E-02	-4.69343116E-01	1.32493815E+01
j=4	21.3482	30.1888	-1.35567415E-03	3.85902922E-02	-5.65979568E-01	9.72497036E+00
j=5	30.1888	43.4352	-1.20591403E-04	2.63537363E-03	-2.01519947E-01	6.80074227E+00
j=6	43.4352	57.5373	9.58895526E-05	-2.15683227E-03	-1.95180996E-01	4.31345834E+00
j=7	57.5373	89.1660	-1.48680703E-05	1.89989991E-03	-1.98804282E-01	1.40098858E+00

Table A.4.: Breaks and coefficients of cubic spline describing the distance between pitch axis and leading edge (in meters) as a function of the radial coordinate (in meters).

	$\xi_j$	$\xi_{j+1}$	$c_{j1}$	$c_{j2}$	$c_{j3}$	$c_{j4}$
j=1	2.8000	10.0000	0.00000000E+000	0.00000000E+000	0.00000000E+000	2.69000000E+000
j=2	10.0000	20.0000	9.73846154E-005	-2.87384615E-003	0.00000000E+000	2.69000000E+000
j=3	20.0000	85.0000	0.00000000E+000	0.00000000E+000	-2.82615385E-002	2.50000000E+000
j=4	85.0000	87.2000	2.03344796E-004	-1.24297791E-002	-2.82615385E-002	6.63000000E-001
j=5	87.2000	89.1660	3.22933723E-003	-2.47827255E-002	-8.00000000E-002	5.42829700E-001

Table A.5.: Breaks and coefficients of cubic spline describing distance between pitch axis and cap center position (in meters) as a function of the radial coordinate (in meters).

	$\xi_j$	$\xi_{j+1}$	$c_{j1}$	$c_{j2}$	$c_{j3}$	$c_{j4}$
j=1	2.8000	10.0000	0.00000000E+000	0.00000000E+000	0.00000000E+000	0.00000000E+000
j=2	10.0000	30.0000	-1.43253727E-004	4.11507454E-003	0.00000000E+000	0.00000000E+000
j=3	30.0000	87.2000	0.00000000E+000	0.00000000E+000	-7.30149072E-003	5.00000000E-001
j=4	87.2000	89.1660	0.00000000E+000	0.00000000E+000	-7.30149072E-003	8.23547308E-002

Table A.6.: Breaks and coefficients of cubic spline describing the width of the caps (in meters) as a function of the radial coordinate (in metres).

	$\xi_j$	$\xi_{j+1}$	$c_{j1}$	$c_{j2}$	$c_{j3}$	$c_{j4}$
j=1	2.8000	6.0000	0.00000000E+00	0.00000000E+00	0.00000000E+00	1.12000000E+00
j=2	6.0000	10.0000	2.87162162E-04	-3.02364865E-03	0.00000000E+00	1.12000000E+00
j=3	10.0000	84.0000	0.00000000E+00	0.00000000E+00	-1.04054054E-02	1.09000000E+00
j=4	84.0000	87.2000	-5.34615503E-04	-1.81880092E-03	-1.04054054E-02	3.20000000E-01
j=5	87.2000	89.1660	-5.34615503E-04	-6.95110975E-03	-3.84691195E-02	2.50559901E-01

## Appendix B.

### Geometry

The original coordinates for FFA-W3-XXX airfoil series are located in the `geometry/airfoils` directory. These airfoils are quite coarsely discretized and have open trailing edges. The more finely resolved airfoil contours used in the 2D CFD simulations are described in Appendix C.1. Table B.1 contains a list of file names and descriptions of the blade planform geometry files.

Filename	ni	Description
DTU_10MW_RWT_blade_axis_straight.dat	40	Low resolution blade geometry for the straight blade.
DTU_10MW_RWT_blade_axis_straight_fine.dat	200	High resolution blade geometry for the straight blade.
DTU_10MW_RWT_blade_axis_prebend.dat	40	Low resolution blade geometry for the pre-bended blade.
DTU_10MW_RWT_blade_axis_prebend_fine.dat	200	High resolution blade geometry for the pre-bended blade.

Table B.1.: List of the the planform geometry files in the `geometry` directory.

The reference 3D surface geometry of the primary components of the DTU 10MW RWT are included in the `geometry` directory. All surfaces are saved in both the unformatted Plot3D format written in double precision as well as the IGES format. The components are generated with their primary axis along the- $z$  axis starting at  $(x, y, z) = (0,0,0)$ . The surfaces are defined as a series of stacked crossed sectional shapes. The blade is resolved with 257 points in the chordwise direction and 200 points in the spanwise direction. The other geometry components are resolved with  $200 \times 200$  points. In the blade geometry, a cylindrical hub with length 2.8 m is included. Since the baseline geometry is defined from individual components it does not include intersections between these components. Only the surfaces used in the 3D CFD simulations described in Section 3.5.2 have been generated as a watertight surface and are described in more detail in Appendix C.2.

A basic Python program is supplied in the `geometry/tools` directory, which is capable of reading the geometry files and rotating and translating the components into place. A Fortran program is also included in `read_plot3d.f` for reading the grids, and it is left to the user to add their own code to write the data in other formats.

Table B.2 contains a list of file names and descriptions of the Plot3D geometry files. All the geometry components

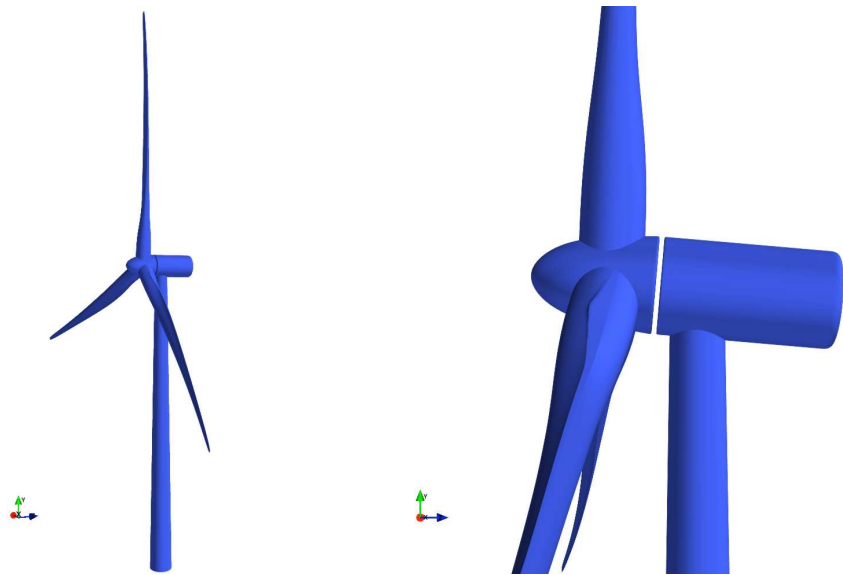


Figure B.1.: Plots of the DTU 10 MW RWT geometry.

<b>Filename</b>	<b>(ni, nj, nk)</b>	<b>Description</b>
DTU_10MW_RWT_blade3D.xyz	(257, 200, 1)	Coordinates of the straight blade with closed trailing edge.
DTU_10MW_RWT_blade3D_openTE.xyz	(257, 200, 1)	Coordinates of the straight blade with open trailing edge.
DTU_10MW_RWT_blade3D_prebend.xyz	(257, 200, 1)	Coordinates of the pre-bended blade with closed trailing edge.
DTU_10MW_RWT_blade3D_prebend_openTE.xyz	(257, 200, 1)	Coordinates of the pre-bended blade with open trailing edge.
DTU_10MW_RWT_nacelle_spinner_3D.xyz	(200, 200, 1)	Coordinates of the patched nacelle and spinner geometry.
DTU_10MW_RWT_nacelle3D.xyz	(200, 200, 1)	Coordinates of the nacelle only geometry.
DTU_10MW_RWT_spinner3D.xyz	(200, 200, 1)	Coordinates of the spinner only geometry.
DTU_10MW_RWT_tower3D.xyz	(200, 200, 1)	Coordinates of the tower geometry.

Table B.2.: List of the Plot3D files in the `geometry` directory.

## **Appendix C.**

### **CFD Data**

The `release/CFD` directory contains two sub-directories, one that contains 2D meshes for the baseline FFA airfoils used on the RWT blade, and another that contains the 3D surface and volume meshes used for the 3D CFD simulations on the rotor.

#### **C.1. 2D CFD Data**

##### **Meshes**

The `CFD/2D/FFA-w3-xxx` directories contains the airfoil shapes and 2D meshes for the airfoils:

1. FFA-W3-224,
2. FFA-W3-301,
3. FFA-W3-336GF,
4. FFA-W3-348GF,
5. FFA-W3-360GF.

For each airfoil an unformatted Plot3D file as well as a file with the airfoil surface point distribution is included. The `read_plot3d.f` file contains a basic fortran routine to read the 2D meshes and attributes.

##### **Simulation Results**

The simulation results presented in Figures 3.3 to 3.7 are included in the `CFD/2D/FFA-w3-xxx` directories. In addition to lift-drag polars, also the pressure and skin friction coefficients are included.

#### **C.2. 3D CFD Data**

The `CFD/3D_DTU_10MW_RWT` directory contains the surface and volume meshes used in the 3D CFD simulations on the RWT rotor described in Section 3.5.2 as well as the results presented in this section.

## **Coordinate system**

The coordinate system used is right-handed and the rotor is oriented in the following way:

- Rotation center at  $(x, y, z) = (0, 0, 0)$ ,
- Blade 1 pointing along positive  $y$ ,
- Flow in the positive  $z$  direction,
- Rotation according to the right hand rule clockwise when viewing the rotor from upstream.

## **Rotor-only mesh (directory: baseline)**

- The spinner and nacelle of the wind turbine are not included,
- The rotor has no tilt,
- The blades have no pre-bend and zero cone angle.

The surface mesh was generated using HypGrid2D [11] and consists of 256 cells in the chordwise direction and 128 cells in the spanwise direction with a  $64 \times 64$  cells tip cap and includes all three blades. The surface mesh is partitioned in 108 blocks of  $32 \times 32$  cells.

## **Rotor and spinner/nacelle mesh (directory: with\_spinner)**

- The spinner and nacelle of the wind turbine are included,
- Rotor, spinner and nacelle geometry is one single water-tight surface,
- The rotor has no tilt,
- The blades have no pre-bend and zero cone angle.

The surface mesh for the spinner and nacelle was generated using Pointwise and had a total of 42 blocks of  $32 \times 32$  cells, but has an otherwise identical surface mesh to the rotor-only mesh for the outer part of the rotor.

## **Volume Meshes**

The volume meshes have 128 cells in the normal direction, with a first cell height of 2.d-6 m and an average domain radius of 1800 m ( $\approx 10D$ ). The volume mesh is partitioned into blocks of  $32 \times 32 \times 32$  totalling 432 blocks for the rotor-only mesh and 600 blocks for the rotor and spinner/nacelle mesh.

## **Boundary conditions**

The rotor simulations described in Section 3.5.2 had an outflow region specified in a region covered by a cone with angle 20 degrees starting from the rotor center. The rest of the outer spherical boundary was specified as inlet.

## **Tools**

The `geometry/tools/read_grid.f` file contains a basic fortran routine for reading the Plot3D files. The python scripts included in `geometry/tools/geometry_tools.py` can also be used to read, manipulate and plot the surface and volume grids.

## **Simulation Results**

The 3D CFD simulation results for the rotor-only mesh are included in the `CFD/3D_DTU_10MW_RWT/baseline/EllipSys3D` directory for both fully turbulent and transitional simulations. The data includes integrated rotor loads as well as sectional forces along the blade.



## **Appendix D.**

### **Load Cases**

Load case	DLC	Wind condition	Time (sec)	num. of turb. seed	Type of analysis	Safety factor	Other conditions
Power production	1.1	Normal Turbulence Model (NTM)	600	6	Ultimate	1.35	Extrapolation scheme is not applied. Therefore 1.35 as a safety factor is considered instead of 1.25.
	1.2	Normal Turbulence Model (NTM)	600	6	Fatigue	-	
	1.3	Extreme Turbulence Model (ETM)	600	6	Ultimate	1.35	
	1.4	Extreme coherent gust with direction change (ECD)	100	-	Ultimate	1.35	
	1.5	Extreme Wind Shear (EWS)	100	-	Ultimate	1.35	EWS is applied after transient period.
Power production with fault	2.1	Normal Turbulence Model (NTM)	300	12	Ultimate	1.35	Electrical network is loss 10s after transient period.
	2.3	Extreme Operating Gust (EOG)	100	-	Ultimate	1.1	Electrical network is loss from 52s to 60s after transient period and EOG is applied just after transient period.
	2.4	Normal Turbulence Model (NTM)	600	6	Fatigue	-	$\pm 20^\circ$ are considered as the electrical system faults.
Start up	3.1	Normal Wind Profile Model (NWP)	300	-	Fatigue	-	Starting up the turbine 0.1s after transient period.
	3.2	Extreme Operating Gust (EOG)	100	-	Ultimate	1.35	Starting up the turbine 0.1s after transient period and EOG is applied 1s after transient period.
	3.3	Extreme Direction Change (EDC)	100	-	Ultimate	1.35	Starting up the turbine 0.1s after transient period and EDC is applied 1s after transient period.

where 100s is considered as a transient period.

Table D.1.: Breaks and coefficients of cubic spline describing the chord length as a function  
*DTU Wind of the Eggerup Offshore* (both in meters).

Load case	DLC	Wind condition	Time (sec)	num. of turb. seed	Type of analysis	Safety factor	Other conditions
Normal shut down	4.1	Normal Wind Profile Model (NWP)	100	-	Fatigue	-	Shutting down the turbine 10s after transient period.
	4.2	Extreme Operating Gust (EOG)	100	-	Ultimate	1.35	Shutting down the turbine 20s after transient period and EOG is applied just after transient period.
Emergency shut down	5.1	Normal Turbulence Model (NTM)	600	12	Ultimate	1.35	Shutting down the turbine 20s after transient period.
Parked (Idling)	6.1	Extreme Wind Speed Model (EWM), 50year recurrence period	600	6	Ultimate	1.35	$\pm 8^\circ$ with the turbulent extreme wind model are considered.
	6.2	Extreme Wind Speed Model (EWM), 50year recurrence period	600	6	Ultimate	1.1	It is assumed that the power for the control and yaw system is able to be back-up within 6 hours.
	6.3	Extreme Wind Speed Model (EWM), 1year recurrence period	600	6	Ultimate	1.35	$\pm 20^\circ$ with the turbulent extreme wind model are considered.
	6.4	Normal Turbulence Model (NTM)	600	6	Fatigue	-	Considered wind speed range is $5m/s \leq V_{hub} \leq 35m/s$ .
Parked and fault condition	7.1	Extreme Wind Speed Model (EWM), 1year recurrence period	600	6	Ultimate	1.1	Wind direction is an equally increase of $30^\circ$ .

where 100s is considered as a transient period.



## **Appendix E.**

### **Extreme loads**

This Appendix lists the extreme loads computed using the aeroelastic code HAWC2 as described in Chapter 6. Results are presented in tabular form for 27 sections along the blade. The extreme values (maxima and minima) of the corresponding load component are located at the diagonal. In addition to the extreme values of the load components the maximum magnitude of the resulting transverse force  $F_{\text{res}}$  and the maximum magnitude of the resulting bending moment  $M_{\text{res}}$  are listed. The simultaneous loads of the other load components are given in the rows.

Each row also lists the load case for which the extreme value occurred and the corresponding safety factor for the loads  $\gamma_F$ . The values given *include* the safety factor for the loads!

The forces and moments relate to the elastic center of the respective cross-section, and are given in a coordinate system aligned with the elastic axes: The x-axis is aligned with the first elastic axis and points towards the leading edge of the blade. The y-axis is aligned with the second elastic axis and points towards the suction side of the blade.

Each row in the tables in this Appendix constitutes a load case for the respective cross section. Some of these load cases may be redundant. For example, the row representing the maximum magnitude of the resulting bending moment  $M_{\text{res}}$  may be identical to the row representing the maximum transverse force  $F_y$ .

Table E.1.: Result of extreme load evaluation for section 1 at  $r = 2.8$  m.

	Load case	$\gamma_F$ [-]	$F_x$ [MN]	$F_y$ [MN]	$F_z$ [MN]	$F_{\text{res}}$ [MN]	$M_x$ [MNm]	$M_y$ [MNm]	$M_z$ [MNm]	$M_{\text{res}}$ [Nm]	
$F_x$	max	dlc1.3	1.35	0.9545	0.8515	1.7150	1.2791	-22.0023	28.8520	0.2992	36.2842
	min	dlc1.3	1.35	-0.8811	-0.0049	1.7782	0.8811	1.8962	-29.8540	-0.6836	29.9141
$F_y$	max	dlc1.3	1.35	0.7415	1.7107	1.3008	1.8644	-67.0299	20.8406	0.2070	70.1950
	min	dlc6.2	1.1	0.0516	-1.4705	0.2888	1.4714	53.3185	5.4149	0.6498	53.5928
$F_z$	max	dlc2.1	1.35	-0.1386	-0.0961	2.9550	0.1687	8.5575	-1.5307	-0.3035	8.6933
	min	dlc6.2	1.1	-0.0221	-0.5805	-0.9061	0.5809	32.5763	-1.3402	0.2697	32.6039
$F_{\text{res}}$	max	dlc1.3	1.35	0.8734	1.6969	1.6753	1.9085	-55.4986	26.5028	0.3113	61.5020
$M_x$	max	dlc6.2	1.1	0.0516	-1.4705	0.2888	1.4714	53.3185	5.4149	0.6498	53.5928
	min	dlc1.3	1.35	0.1648	1.4088	0.9889	1.4184	-69.9054	8.9310	0.4212	70.4736
$M_y$	max	dlc2.1	1.35	0.9132	0.0594	1.6056	0.9152	13.9288	32.2634	0.7215	35.1416
	min	dlc1.3	1.35	-0.8811	-0.0049	1.7782	0.8811	1.8962	-29.8540	-0.6836	29.9141
$M_z$	max	dlc5.1	1.35	0.0248	0.0159	0.5433	0.0294	-0.4221	3.4578	1.2423	3.4835
	min	dlc2.1	1.35	-0.2631	-0.0325	0.5618	0.2651	0.0746	-11.0580	-1.4891	11.0582
$M_{\text{res}}$	max	dlc1.3	1.35	0.5940	1.3346	0.9789	1.4608	-67.0671	21.7271	0.4639	70.4987

Table E.2.: Result of extreme load evaluation for section 2 at  $r = 5.8$  m.

	Load case	$\gamma_F$ [-]	$F_x$ [MN]	$F_y$ [MN]	$F_z$ [MN]	$F_{\text{res}}$ [MN]	$M_x$ [MNm]	$M_y$ [MNm]	$M_z$ [MNm]	$M_{\text{res}}$ [Nm]	
$F_x$	max	dlc1.3	1.35	0.9155	0.8241	1.7060	1.2318	-19.4659	26.0434	0.2850	32.5143
	min	dlc1.3	1.35	-0.8371	0.0019	1.7420	0.8371	1.9130	-27.2759	-0.6774	27.3429
$F_y$	max	dlc1.3	1.35	0.7025	1.6879	1.3008	1.8282	-61.9121	18.6724	0.1983	64.6666
	min	dlc6.2	1.1	0.0646	-1.4296	0.2524	1.4311	48.9713	5.2403	0.6872	49.2509
$F_z$	max	dlc2.1	1.35	-0.1241	-0.0987	2.8841	0.1586	8.3027	-1.1409	-0.2991	8.3807
	min	dlc6.2	1.1	-0.0294	-0.5627	-0.8436	0.5635	30.8746	-1.2720	0.2912	30.9008
$F_{\text{res}}$	max	dlc1.3	1.35	0.8374	1.6646	1.6515	1.8633	-50.4330	23.9342	0.2973	55.8241
$M_x$	max	dlc6.2	1.1	0.0646	-1.4296	0.2524	1.4311	48.9713	5.2403	0.6872	49.2509
	min	dlc1.3	1.35	0.1689	1.4054	1.0211	1.4155	-65.6709	8.4290	0.4223	66.2096
$M_y$	max	dlc2.1	1.35	0.8556	0.0672	1.6054	0.8582	12.8450	29.6236	0.6948	32.2886
	min	dlc1.3	1.35	-0.8371	0.0019	1.7420	0.8371	1.9130	-27.2759	-0.6774	27.3429
$M_z$	max	dlc2.3	1.1	0.7082	-0.4000	1.7072	0.8133	28.2533	25.3360	1.0627	37.9495
	min	dlc2.1	1.35	-0.2554	-0.0295	0.5137	0.2571	-0.0104	-10.2805	-1.2084	10.2805
$M_{\text{res}}$	max	dlc1.3	1.35	0.1689	1.4054	1.0211	1.4155	-65.6709	8.4290	0.4223	66.2096

Table E.3.: Result of extreme load evaluation for section 3 at  $r = 8.8$  m.

	Load case	$\gamma_F$ [-]	$F_x$ [MN]	$F_y$ [MN]	$F_z$ [MN]	$F_{\text{res}}$ [MN]	$M_x$ [MNm]	$M_y$ [MNm]	$M_z$ [MNm]	$M_{\text{res}}$ [Nm]
$F_x$	max	dlc1.3	1.35	0.8755	0.7950	1.6817	1.1826	-17.0164	23.3385	0.2771
	min	dlc1.3	1.35	-0.7901	0.0076	1.6935	0.7902	1.9487	-24.8473	-0.6711
$F_y$	max	dlc1.3	1.35	0.6640	1.6609	1.2879	1.7887	-56.8663	16.6114	0.2025
	min	dlc6.2	1.1	-0.0256	-1.3883	-0.5059	1.3886	43.9873	1.3562	0.5819
$F_z$	max	dlc2.1	1.35	-0.1091	-0.1045	2.7921	0.1510	8.0312	-0.8174	-0.2955
	min	dlc6.2	1.1	-0.0422	-0.5719	-0.7807	0.5734	29.1913	-1.1648	0.3088
$F_{\text{res}}$	max	dlc1.3	1.35	0.8019	1.6284	1.6140	1.8151	-45.4697	21.4603	0.2950
	min	dlc6.2	1.1	0.0850	-1.3826	0.2135	1.3852	44.7568	5.1663	0.7134
$M_x$	max	dlc6.2	1.1	0.0850	-1.3826	0.2135	1.3852	44.7568	5.1663	0.7134
	min	dlc1.3	1.35	0.1735	1.4004	1.0383	1.4111	-61.4485	7.9073	0.4339
$M_y$	max	dlc2.1	1.35	0.8140	0.0386	1.5843	0.8149	13.0197	27.1010	0.6793
	min	dlc1.3	1.35	-0.7852	-0.0072	1.7013	0.7852	3.0787	-24.8496	-0.6870
$M_z$	max	dlc2.3	1.1	0.6716	-0.4158	1.6572	0.7899	27.0496	23.2466	1.0476
	min	dlc1.3	1.35	-0.5102	0.0210	1.9439	0.5106	6.6347	-19.4429	-0.9657
$M_{\text{res}}$	max	dlc1.3	1.35	0.1735	1.4004	1.0383	1.4111	-61.4485	7.9073	0.4339
	min	dlc1.3	1.35	0.1735	1.4004	1.0383	1.4111	-61.4485	7.9073	0.4339

Table E.4.: Result of extreme load evaluation for section 4 at  $r = 9.8$  m.

	Load case	$\gamma_F$ [-]	$F_x$ [MN]	$F_y$ [MN]	$F_z$ [MN]	$F_{\text{res}}$ [MN]	$M_x$ [MNm]	$M_y$ [MNm]	$M_z$ [MNm]	$M_{\text{res}}$ [Nm]
$F_x$	max	dlc1.3	1.35	0.8621	0.7842	1.6560	1.1654	-16.2208	22.4824	0.2657
	min	dlc1.3	1.35	-0.7746	0.0083	1.6631	0.7746	1.9681	-24.0627	-0.6670
$F_y$	max	dlc1.3	1.35	0.6515	1.6506	1.2687	1.7745	-55.2134	15.9617	0.1910
	min	dlc6.2	1.1	-0.0202	-1.3761	-0.4937	1.3763	42.5974	1.3784	0.6011
$F_z$	max	dlc2.1	1.35	-0.1035	-0.1092	2.7374	0.1504	7.9439	-0.7004	-0.2932
	min	dlc6.2	1.1	-0.0468	-0.5804	-0.7604	0.5823	28.6127	-1.1247	0.3192
$F_{\text{res}}$	max	dlc1.3	1.35	0.7905	1.6150	1.5857	1.7981	-43.8484	20.6746	0.2802
$M_x$	max	dlc6.2	1.1	0.0891	-1.3674	0.2020	1.3703	43.3851	5.0826	0.7315
	min	dlc1.3	1.35	0.1751	1.3977	1.0264	1.4086	-60.0528	7.7364	0.4267
$M_y$	max	dlc2.1	1.35	0.8013	0.0271	1.5579	0.8018	13.0637	26.3058	0.6711
	min	dlc1.3	1.35	-0.7699	-0.0070	1.6703	0.7699	3.0836	-24.0703	-0.6831
$M_z$	max	dlc2.3	1.1	0.6604	-0.4225	1.6239	0.7840	26.6466	22.5954	1.0432
	min	dlc1.3	1.35	-0.4973	0.0211	1.9083	0.4978	6.6693	-18.9369	-0.9616
$M_{\text{res}}$	max	dlc1.3	1.35	0.1751	1.3977	1.0264	1.4086	-60.0528	7.7364	0.4267
										60.5490

Table E.5.: Result of extreme load evaluation for section 5 at  $r = 11.5$  m.

	Load case	$\gamma_F$ [-]	$F_x$ [MN]	$F_y$ [MN]	$F_z$ [MN]	$F_{\text{res}}$ [MN]	$M_x$ [MNm]	$M_y$ [MNm]	$M_z$ [MNm]	$M_{\text{res}}$ [Nm]	
$F_x$	max	dlc1.3	1.35	0.8378	0.7658	1.6326	1.1351	-14.9033	21.0269	0.2673	25.7729
	min	dlc1.3	1.35	-0.7498	0.0088	1.6290	0.7499	1.9837	-22.7831	-0.6697	22.8693
$F_y$	max	dlc1.3	1.35	0.6303	1.6321	1.2531	1.7496	-52.4256	14.8639	0.2026	54.4920
	min	dlc6.2	1.1	-0.0113	-1.3524	-0.4737	1.3525	40.2716	1.4089	0.6108	40.2962
$F_z$	max	dlc2.1	1.35	-0.3188	0.5652	2.6764	0.6489	-21.9315	-9.2286	-0.1700	23.7941
	min	dlc6.2	1.1	-0.0543	-0.6002	-0.7270	0.6026	27.6165	-1.0347	0.3268	27.6359
$F_{\text{res}}$	max	dlc1.3	1.35	0.7703	1.5917	1.5565	1.7683	-41.1267	19.3390	0.2878	45.4466
$M_x$	max	dlc6.2	1.1	0.0957	-1.3402	0.1834	1.3436	41.0823	4.9234	0.7394	41.3762
	min	dlc1.3	1.35	0.1774	1.3934	1.0251	1.4046	-57.6850	7.4304	0.4377	58.1616
$M_y$	max	dlc2.1	1.35	0.7783	0.0095	1.5354	0.7784	13.0970	24.9540	0.6673	28.1821
	min	dlc1.3	1.35	-0.7454	-0.0075	1.6351	0.7455	3.0736	-22.7981	-0.6863	23.0043
$M_z$	max	dlc2.3	1.1	0.6401	-0.4325	1.5876	0.7725	25.9275	21.4809	1.0367	33.6699
	min	dlc1.3	1.35	-0.4774	0.0204	1.8688	0.4779	6.7084	-18.1281	-0.9607	19.3295
$M_{\text{res}}$	max	dlc1.3	1.35	0.1774	1.3934	1.0251	1.4046	-57.6850	7.4304	0.4377	58.1616

Table E.6.: Result of extreme load evaluation for section 6 at  $r = 13.2$  m.

	Load case	$\gamma_F$ [-]	$F_x$ [MN]	$F_y$ [MN]	$F_z$ [MN]	$F_{\text{res}}$ [MN]	$M_x$ [MNm]	$M_y$ [MNm]	$M_z$ [MNm]	$M_{\text{res}}$ [Nm]	
$F_x$	max	dlc1.3	1.35	0.8121	0.7456	1.6027	1.1024	-13.6126	19.6475	0.2472	23.9025
	min	dlc1.3	1.35	-0.7267	0.0074	1.5903	0.7268	2.0122	-21.5182	-0.6676	21.6120
$F_y$	max	dlc1.3	1.35	0.6090	1.6115	1.2317	1.7228	-49.6688	13.8267	0.1799	51.5574
	min	dlc6.2	1.1	-0.0027	-1.3241	-0.4548	1.3241	37.9742	1.4133	0.6422	38.0005
$F_z$	max	dlc2.1	1.35	-0.3041	0.5581	2.6109	0.6356	-20.9757	-8.6780	-0.1767	22.6999
	min	dlc6.2	1.1	-0.0611	-0.6252	-0.6952	0.6282	26.5666	-0.9441	0.3448	26.5834
$F_{\text{res}}$	max	dlc1.3	1.35	0.7492	1.5656	1.5220	1.7357	-38.4433	18.0696	0.2588	42.4782
$M_x$	max	dlc6.2	1.1	0.1017	-1.3103	0.1660	1.3143	38.8238	4.7536	0.7679	39.1138
	min	dlc1.3	1.35	0.1745	1.3840	1.0163	1.3949	-55.3232	7.0217	0.3944	55.7670
$M_y$	max	dlc2.1	1.35	0.7552	-0.0095	1.5056	0.7553	13.1137	23.6727	0.6577	27.0623
	min	dlc1.3	1.35	-0.7227	-0.0101	1.5954	0.7227	3.0724	-21.5404	-0.6843	21.7584
$M_z$	max	dlc2.3	1.1	0.6201	-0.4436	1.5459	0.7624	25.2079	20.4328	1.0317	32.4490
	min	dlc1.3	1.35	-0.4601	0.0173	1.8237	0.4604	6.7589	-17.3205	-0.9567	18.5925
$M_{\text{res}}$	max	dlc1.3	1.35	0.1792	1.3878	1.0163	1.3993	-55.3232	7.1420	0.4202	55.7823

Table E.7.: Result of extreme load evaluation for section 7 at  $r = 15$  m.

	Load case	$\gamma_F$ [-]	$F_x$ [MN]	$F_y$ [MN]	$F_z$ [MN]	$F_{\text{res}}$ [MN]	$M_x$ [MNm]	$M_y$ [MNm]	$M_z$ [MNm]	$M_{\text{res}}$ [Nm]
$F_x$	max	dlc1.3	1.35	0.7834	0.7223	1.5725	1.0655	-12.2852	18.1696	0.2559
	min	dlc1.3	1.35	-0.7043	0.0046	1.5515	0.7043	2.0292	-20.2721	-0.6687
$F_y$	max	dlc1.3	1.35	0.5865	1.5876	1.2099	1.6925	-46.7836	12.7178	0.2183
	min	dlc6.2	1.1	0.0059	-1.2882	-0.4360	1.2882	35.6039	1.4222	0.6225
$F_z$	max	dlc2.1	1.35	-0.2900	0.5505	2.5453	0.6222	-19.9781	-8.2145	-0.1653
	min	dlc6.2	1.1	-0.0668	-0.6550	-0.6636	0.6584	25.4097	-0.8096	0.3387
$F_{\text{res}}$	max	dlc1.3	1.35	0.7257	1.5350	1.4871	1.6979	-35.6469	16.7025	0.2885
$M_x$	max	dlc6.2	1.1	0.1069	-1.2750	0.1490	1.2795	36.4862	4.5603	0.7465
	min	dlc1.3	1.35	0.1762	1.3776	1.0068	1.3889	-52.8340	6.6807	0.4283
$M_y$	max	dlc2.1	1.35	0.7114	-0.0034	1.4858	0.7114	12.2710	22.3188	0.6453
	min	dlc1.3	1.35	-0.7006	-0.0141	1.5556	0.7007	3.0577	-20.3019	-0.6862
$M_z$	max	dlc2.3	1.1	0.5991	-0.4558	1.5041	0.7528	24.4094	19.2976	1.0117
	min	dlc1.3	1.35	-0.4449	0.0123	1.7785	0.4451	6.7957	-16.5576	-0.9545
$M_{\text{res}}$	max	dlc1.3	1.35	0.1805	1.3808	1.0068	1.3925	-52.8274	6.7925	0.4540
										53.2623

Table E.8.: Result of extreme load evaluation for section 8 at  $r = 16$  m.

	Load case	$\gamma_F$ [-]	$F_x$ [MN]	$F_y$ [MN]	$F_z$ [MN]	$F_{\text{res}}$ [MN]	$M_x$ [MNm]	$M_y$ [MNm]	$M_z$ [MNm]	$M_{\text{res}}$ [Nm]	
$F_x$	max	dlc1.3	1.35	0.7668	0.7080	1.5502	1.0437	-11.5710	17.3894	0.2530	20.8873
	min	dlc1.3	1.35	-0.6924	0.0028	1.5259	0.6924	2.0387	-19.5910	-0.6679	19.6968
$F_y$	max	dlc1.3	1.35	0.5737	1.5731	1.1932	1.6745	-45.2125	12.1300	0.2255	46.8114
	min	dlc6.2	1.1	0.0103	-1.2653	-0.4261	1.2654	34.3120	1.4136	0.6181	34.3411
$F_z$	max	dlc2.1	1.35	-0.2826	0.5451	2.5019	0.6140	-19.4381	-7.9501	-0.1647	21.0010
	min	dlc6.2	1.1	-0.0692	-0.6724	-0.6467	0.6760	24.7362	-0.7371	0.3392	24.7472
$F_{\text{res}}$	max	dlc1.3	1.35	0.7122	1.5165	1.4631	1.6754	-34.1300	15.9768	0.2904	37.6844
$M_x$	max	dlc6.2	1.1	0.1091	-1.2535	0.1400	1.2582	35.2176	4.4464	0.7414	35.4972
	min	dlc1.3	1.35	0.1770	1.3733	0.9959	1.3846	-51.4668	6.4969	0.4333	51.8752
$M_y$	max	dlc2.1	1.35	0.6986	-0.0152	1.4633	0.6988	12.2703	21.6098	0.6407	24.8505
	min	dlc1.3	1.35	-0.6888	-0.0166	1.5295	0.6890	3.0491	-19.6241	-0.6855	19.8595
$M_z$	max	dlc2.3	1.1	0.5877	-0.4635	1.4761	0.7485	23.9661	18.6987	1.0009	30.3976
	min	dlc1.3	1.35	-0.4375	0.0087	1.7484	0.4376	6.8151	-16.1358	-0.9523	17.5160
$M_{\text{res}}$	max	dlc1.3	1.35	0.1810	1.3760	0.9959	1.3879	-51.4571	6.6050	0.4589	51.8793

Table E.9.: Result of extreme load evaluation for section 9 at  $r = 17.8\text{m}$ .

	Load case	$\gamma_F$ [-]	$F_x$ [MN]	$F_y$ [MN]	$F_z$ [MN]	$F_{\text{res}}$ [MN]	$M_x$ [MNm]	$M_y$ [MNm]	$M_z$ [MNm]	$M_{\text{res}}$ [Nm]
$F_x$	max	dlc1.3	1.35	0.7354	0.6806	1.5159	1.0020	-10.3125	16.0261	0.2445
	min	dlc1.3	1.35	-0.6712	-0.0003	1.4850	0.6712	2.0536	-18.3818	-0.6660
$F_y$	max	dlc1.3	1.35	0.5498	1.5443	1.1678	1.6392	-42.4023	11.1091	0.2345
	min	dlc6.2	1.1	0.0175	-1.2194	-0.4086	1.2196	32.0533	1.3923	0.6109
$F_z$	max	dlc2.1	1.35	-0.2703	0.5353	2.4328	0.5997	-18.4625	-7.4808	-0.1655
	min	dlc6.2	1.1	-0.0723	-0.7043	-0.6172	0.7080	23.4830	-0.6005	0.3408
$F_{\text{res}}$	max	dlc1.3	1.35	0.5498	1.5443	1.1678	1.6392	-42.4023	11.1091	0.2345
$M_x$	max	dlc6.2	1.1	0.0413	-1.1446	-0.4035	1.1453	33.0305	2.0517	0.6443
	min	dlc1.3	1.35	0.1778	1.3647	0.9812	1.3762	-49.0013	6.1706	0.4402
$M_y$	max	dlc2.1	1.35	0.6745	-0.0372	1.4289	0.6755	12.2378	20.3649	0.6317
	min	dlc1.3	1.35	-0.6680	-0.0211	1.4878	0.6683	3.0271	-18.4215	-0.6839
$M_z$	max	dlc2.3	1.1	0.5665	-0.4779	1.4316	0.7412	23.1388	17.6519	0.9820
	min	dlc1.3	1.35	-0.4261	0.0006	1.7005	0.4261	6.8401	-15.3821	-0.9485
$M_{\text{res}}$	max	dlc1.3	1.35	0.1778	1.3647	0.9812	1.3762	-49.0013	6.1706	0.4402
										49.3883

Table E.10.: Result of extreme load evaluation for section 10 at  $r = 21$  m.

	Load case	$\gamma_F$ [-]	$F_x$ [MN]	$F_y$ [MN]	$F_z$ [MN]	$F_{\text{res}}$ [MN]	$M_x$ [MNm]	$M_y$ [MNm]	$M_z$ [MNm]	$M_{\text{res}}$ [Nm]	
$F_x$	max	dlc1.3	1.35	0.6773	0.6256	1.4478	0.9220	-8.2509	13.7634	0.2386	16.0471
	min	dlc1.3	1.35	-0.6344	-0.0091	1.4081	0.6344	2.0966	-16.3969	-0.6529	16.5304
$F_y$	max	dlc1.3	1.35	0.4879	1.4818	1.1155	1.5601	-37.8213	8.8014	0.2949	38.8319
	min	dlc6.2	1.1	0.1087	-1.1327	0.1019	1.1379	29.2162	3.7395	0.6695	29.4545
$F_z$	max	dlc2.1	1.35	-0.2509	0.5129	2.3027	0.5710	-16.8566	-6.7659	-0.1649	18.1638
	min	dlc6.2	1.1	-0.0750	-0.7583	-0.5678	0.7620	21.0710	-0.3632	0.3216	21.0741
$F_{\text{res}}$	max	dlc1.3	1.35	0.5043	1.4809	1.1164	1.5644	-37.6769	9.3755	0.2752	38.8259
$M_x$	max	dlc6.2	1.1	0.2123	-1.0317	-0.3724	1.0534	29.5002	7.0034	0.9094	30.3201
	min	dlc1.3	1.35	0.1787	1.3461	0.9459	1.3579	-44.7673	5.5505	0.4591	45.1101
$M_y$	max	dlc2.1	1.35	0.6296	-0.0862	1.3594	0.6354	12.1219	18.2678	0.5898	21.9238
	min	dlc1.3	1.35	-0.6317	-0.0323	1.4096	0.6325	3.0047	-16.4462	-0.6710	16.7185
$M_z$	max	dlc2.3	1.1	0.5301	-0.5053	1.3473	0.7323	21.7285	15.8434	0.9168	26.8913
	min	dlc1.3	1.35	-0.4304	-0.0494	1.6114	0.4332	7.0581	-14.6188	-0.9377	16.2334
$M_{\text{res}}$	max	dlc1.3	1.35	0.1787	1.3461	0.9459	1.3579	-44.7673	5.5505	0.4591	45.1101

Table E.11.: Result of extreme load evaluation for section 11 at  $r = 24.2$  m.

	Load case	$\gamma_F$ [-]	$F_x$ [MN]	$F_y$ [MN]	$F_z$ [MN]	$F_{\text{res}}$ [MN]	$M_x$ [MNm]	$M_y$ [MNm]	$M_z$ [MNm]	$M_{\text{res}}$ [Nm]
$F_x$	max	dlc1.3	1.35	0.6201	0.5670	1.3796	0.8402	-6.3263	11.7007	0.2098
	min	dlc1.3	1.35	-0.5978	-0.0194	1.3335	0.5981	2.0900	-14.4587	-0.6439
$F_y$	max	dlc1.3	1.35	0.4443	1.4147	1.0644	1.4828	-33.2051	7.3193	0.2831
	min	dlc6.2	1.1	0.1081	-1.0553	0.0802	1.0609	25.7233	3.3898	0.6537
$F_z$	max	dlc2.1	1.35	-0.2329	0.4912	2.1765	0.5436	-15.2363	-6.0230	-0.1670
	min	dlc6.2	1.1	-0.0725	-0.7945	-0.5227	0.7978	18.5518	-0.1156	0.3236
$F_{\text{res}}$	max	dlc1.3	1.35	0.4605	1.4110	1.0647	1.4843	-33.0681	7.8414	0.2638
$M_x$	max	dlc1.3	1.35	0.0195	-0.7359	1.7650	0.7362	26.5539	1.6363	-0.0493
	min	dlc1.3	1.35	0.1795	1.3249	0.9077	1.3370	-40.5149	4.9810	0.4500
$M_y$	max	dlc2.1	1.35	0.5768	-0.1117	1.3012	0.5875	11.3194	16.3736	0.5579
	min	dlc1.3	1.35	-0.5956	-0.0447	1.3338	0.5972	2.9221	-14.5158	-0.6619
$M_z$	max	dlc6.2	1.1	0.1860	-0.9590	-0.3510	0.9769	26.1955	6.1252	0.9005
	min	dlc1.3	1.35	-0.4174	-0.0746	1.5220	0.4240	6.9106	-13.2988	-0.9337
$M_{\text{res}}$	max	dlc1.3	1.35	0.1795	1.3249	0.9077	1.3370	-40.5149	4.9810	0.4500
										40.8200

Table E.12.: Result of extreme load evaluation for section 12 at  $r = 27.4$  m.

	Load case	$\gamma_F$ [-]	$F_x$ [MN]	$F_y$ [MN]	$F_z$ [MN]	$F_{\text{res}}$ [MN]	$M_x$ [MNm]	$M_y$ [MNm]	$M_z$ [MNm]	$M_{\text{res}}$ [Nm]
$F_x$ max	dlc1.3	1.35	0.5642	0.4654	1.3068	0.7314	-4.1776	10.5990	0.1511	11.3926
min	dlc1.3	1.35	-0.5626	-0.0346	1.2575	0.5637	2.0678	-12.5822	-0.6230	12.7509
$F_y$ max	dlc1.3	1.35	0.4027	1.3413	1.0099	1.4005	-28.7949	6.0157	0.2006	29.4166
min	dlc6.2	1.1	0.1058	-0.9822	0.0614	0.9878	22.4749	3.0484	0.6737	22.6807
$F_z$ max	dlc2.1	1.35	-0.2156	0.4710	2.0484	0.5180	-13.6443	-5.2502	-0.1799	14.6196
min	dlc6.2	1.1	-0.0613	-0.7981	-0.4806	0.8005	15.9572	0.0895	0.3474	15.9574
$F_{\text{res}}$ max	dlc1.3	1.35	0.4027	1.3413	1.0099	1.4005	-28.7949	6.0157	0.2006	29.4166
$M_x$ max	dlc1.3	1.35	0.0180	-0.7347	1.6344	0.7349	24.3210	2.0302	0.0516	24.4056
min	dlc1.3	1.35	0.1790	1.2983	0.8637	1.3106	-36.3231	4.4471	0.3816	36.5943
$M_y$ max	dlc2.1	1.35	0.5417	-0.1605	1.2275	0.5650	10.9493	14.6497	0.5308	18.2894
min	dlc1.3	1.35	-0.4655	0.2981	1.1790	0.5528	-7.7661	-12.9682	-0.3300	15.1158
$M_z$ max	dlc6.2	1.1	0.1812	-0.8926	-0.3278	0.9108	23.2100	5.5252	0.9169	23.8586
min	dlc1.3	1.35	-0.4069	-0.1072	1.4308	0.4208	6.6988	-11.9562	-0.9200	13.7049
$M_{\text{res}}$ max	dlc1.3	1.35	0.1799	1.2944	0.8636	1.3069	-36.3185	4.5287	0.4046	36.5998

Table E.13.: Result of extreme load evaluation for section 13 at  $r = 30.6$  m.

	Load case	$\gamma_F$ [-]	$F_x$ [MN]	$F_y$ [MN]	$F_z$ [MN]	$F_{\text{res}}$ [MN]	$M_x$ [MNm]	$M_y$ [MNm]	$M_z$ [MNm]	$M_{\text{res}}$ [Nm]	
$F_x$	max	dlc2.1	1.35	0.5190	-0.2550	1.1121	0.5783	11.2096	12.6676	0.4794	16.9152
	min	dlc1.3	1.35	-0.5268	-0.0514	1.1688	0.5293	2.0280	-10.9941	-0.5923	11.1796
$F_y$	max	dlc1.3	1.35	0.1753	1.2618	0.8022	1.2740	-32.4301	3.8441	0.4260	32.6571
	min	dlc6.2	1.1	0.1025	-0.9102	0.0450	0.9160	19.4759	2.6970	0.5602	19.6617
$F_z$	max	dlc2.1	1.35	-0.1991	0.4492	1.8995	0.4913	-12.2859	-4.7494	-0.1572	13.1720
	min	dlc6.2	1.1	-0.0414	-0.7619	-0.4401	0.7630	13.3607	0.2941	0.2681	13.3639
$F_{\text{res}}$	max	dlc1.3	1.35	0.3609	1.2574	0.9412	1.3082	-24.8318	4.7771	0.2608	25.2871
$M_x$	max	dlc1.3	1.35	0.0235	-0.7498	1.5027	0.7501	22.3217	1.8258	-0.0022	22.3962
	min	dlc1.3	1.35	-0.0422	1.1364	0.9716	1.1372	-32.4606	0.8070	0.4734	32.4706
$M_y$	max	dlc2.1	1.35	0.5109	-0.2038	1.1356	0.5501	10.5061	12.9468	0.4698	16.6733
	min	dlc1.3	1.35	-0.4468	0.2683	1.0994	0.5212	-6.8607	-11.6442	-0.3097	13.5150
$M_z$	max	dlc2.1	1.35	0.3969	-0.5321	0.7703	0.6638	17.1568	11.8362	0.8138	20.8435
	min	dlc1.3	1.35	-0.3958	-0.1423	1.3244	0.4206	6.4618	-10.8388	-0.8961	12.6188
$M_{\text{res}}$	max	dlc1.3	1.35	0.1757	1.2569	0.8021	1.2691	-32.4392	3.9252	0.4466	32.6758

Table E.14.: Result of extreme load evaluation for section 14 at  $r = 33.8$  m.

	Load case	$\gamma_F$ [-]	$F_x$ [MN]	$F_y$ [MN]	$F_z$ [MN]	$F_{\text{res}}$ [MN]	$M_x$ [MNm]	$M_y$ [MNm]	$M_z$ [MNm]	$M_{\text{res}}$ [Nm]
$F_x$	max	dlc2.1	1.35	0.4849	-0.2563	1.0427	0.5485	10.1788	11.2851	0.4511
	min	dlc1.3	1.35	-0.4887	-0.0644	1.0888	0.4929	1.9327	-9.4027	-0.5581
$F_y$	max	dlc1.3	1.35	0.1685	1.2155	0.7494	1.2271	-28.5110	3.3172	0.3786
	min	dlc6.2	1.1	0.1006	-0.8382	0.0287	0.8442	16.7325	2.3954	0.5337
$F_z$	max	dlc2.1	1.35	-0.1834	0.4298	1.7652	0.4673	-10.8383	-4.1469	-0.1505
	min	dlc6.2	1.1	-0.0156	-0.6870	-0.3986	0.6872	10.9752	0.3911	0.2352
$F_{\text{res}}$	max	dlc1.3	1.35	0.1685	1.2155	0.7494	1.2271	-28.5110	3.3172	0.3786
	min	dlc1.3	1.35	0.0198	-0.7422	1.3745	0.7425	20.1389	2.1923	0.1096
$M_x$	max	dlc1.3	1.35	0.0492	1.0116	0.7530	1.0128	-29.1700	2.1019	0.4038
	min	dlc1.3	1.35	0.4721	-0.2175	1.0661	0.5198	9.6364	11.4189	0.4273
$M_y$	max	dlc2.1	1.35	-0.4260	0.2409	1.0287	0.4894	-5.9984	-10.2726	-0.2926
	min	dlc1.3	1.35	0.3810	-0.5272	0.7186	0.6505	15.5538	10.6129	0.7997
$M_z$	max	dlc2.1	1.35	-0.3816	-0.1691	1.2285	0.4174	6.0788	-9.6316	-0.8632
	min	dlc1.3	1.35	0.0728	1.0128	0.5945	1.0154	-29.1393	3.2052	0.2921
$M_{\text{res}}$	max	dlc1.3	1.35							29.3150

	Load case	$\gamma_F$ [-]	$F_x$ [MN]	$F_y$ [MN]	$F_z$ [MN]	$F_{\text{res}}$ [MN]	$M_x$ [MNm]	$M_y$ [MNm]	$M_z$ [MNm]	$M_{\text{res}}$ [Nm]	
$F_x$	max	dlc2.1	1.35	0.4528	-0.2808	0.9578	0.5328	9.4125	9.8310	0.4349	13.6104
	min	dlc1.3	1.35	-0.4487	-0.0748	1.0063	0.4549	1.7932	-7.9237	-0.5237	8.1241
$F_y$	max	dlc1.3	1.35	0.1581	1.1569	0.6927	1.1677	-24.7580	2.8234	0.3147	24.9184
	min	dlc2.1	1.35	0.1653	-0.7759	1.3395	0.7933	14.7090	4.3013	0.2420	15.3250
$F_z$	max	dlc2.1	1.35	-0.1685	0.4102	1.6271	0.4435	-9.4557	-3.5750	-0.1471	10.1090
	min	dlc6.2	1.1	0.0100	-0.5844	-0.3570	0.5845	8.8841	0.3995	0.1995	8.8931
$F_{\text{res}}$	max	dlc1.3	1.35	0.1581	1.1569	0.6927	1.1677	-24.7580	2.8234	0.3147	24.9184
$M_x$	max	dlc1.3	1.35	0.0269	-0.7378	1.2549	0.7382	17.9614	2.1249	0.1412	18.0867
	min	dlc1.3	1.35	0.0809	0.9693	0.5382	0.9726	-26.0064	2.9363	0.2559	26.1716
$M_y$	max	dlc2.1	1.35	0.4446	-0.2411	0.9806	0.5057	8.9954	9.9994	0.4107	13.4501
	min	dlc1.3	1.35	-0.4023	0.2199	0.9544	0.4584	-5.2174	-8.9609	-0.2754	10.3691
$M_z$	max	dlc2.1	1.35	0.3650	-0.5201	0.6628	0.6354	13.9645	9.4448	0.7943	16.8586
	min	dlc1.3	1.35	-0.3655	-0.1888	1.1299	0.4114	5.6131	-8.4588	-0.8244	10.1517
$M_{\text{res}}$	max	dlc1.3	1.35	0.0809	0.9693	0.5382	0.9726	-26.0064	2.9363	0.2559	26.1716

Table E.15.: Result of extreme load evaluation for section 15 at  $r = 37$  m.

Table E.16.: Result of extreme load evaluation for section 16 at  $r = 43$  m.

	Load case	$\gamma_F$ [-]	$F_x$ [MN]	$F_y$ [MN]	$F_z$ [MN]	$F_{\text{res}}$ [MN]	$M_x$ [MNm]	$M_y$ [MNm]	$M_z$ [MNm]	$M_{\text{res}}$ [Nm]	
$F_x$	max	dlc2.1	1.35	0.3934	-0.2962	0.7947	0.4925	7.9866	7.5166	0.2707	10.9674
	min	dlc1.3	1.35	-0.3706	-0.1129	0.8379	0.3874	1.8886	-5.7143	-0.4367	6.0183
$F_y$	max	dlc1.3	1.35	0.1342	1.0237	0.5725	1.0325	-18.8390	2.0156	0.2525	18.9465
	min	dlc1.3	1.35	0.0319	-0.7133	1.0322	0.7141	14.4437	0.8930	-0.0902	14.4712
$F_z$	max	dlc2.1	1.35	-0.1474	0.3642	1.3525	0.3929	-7.4277	-2.5466	-0.1733	7.8521
	min	dlc6.2	1.1	0.0099	-0.4918	-0.2867	0.4919	6.4294	0.4469	0.1796	6.4449
$F_{\text{res}}$	max	dlc1.3	1.35	0.1342	1.0237	0.5725	1.0325	-18.8390	2.0156	0.2525	18.9465
$M_x$	max	dlc1.3	1.35	0.0416	-0.6889	1.0131	0.6901	14.7903	2.2970	0.1960	14.9676
	min	dlc1.3	1.35	0.0849	0.8890	0.4251	0.8930	-20.8624	2.3443	0.2184	20.9937
$M_y$	max	dlc2.1	1.35	0.3829	-0.2624	0.8181	0.4642	7.7728	7.5978	0.2641	10.8694
	min	dlc1.3	1.35	-0.3518	0.1921	0.8008	0.4008	-4.0428	-6.8371	-0.2710	7.9430
$M_z$	max	dlc2.1	1.35	0.3334	-0.4987	0.5438	0.5999	11.3625	7.3758	0.5927	13.5465
	min	dlc1.3	1.35	-0.3302	-0.2020	0.9335	0.3871	4.8843	-6.5702	-0.6758	8.1868
$M_{\text{res}}$	max	dlc1.3	1.35	0.0849	0.8890	0.4251	0.8930	-20.8624	2.3443	0.2184	20.9937

Table E.17.: Result of extreme load evaluation for section 17 at  $r = 49.4$  m.

	Load case	$\gamma_F$ [-]	$F_x$ [MN]	$F_y$ [MN]	$F_z$ [MN]	$F_{\text{res}}$ [MN]	$M_x$ [MNm]	$M_y$ [MNm]	$M_z$ [MNm]	$M_{\text{res}}$ [Nm]	
$F_x$	max	dlc2.1	1.35	0.3281	-0.2966	0.6332	0.4423	6.2582	5.3298	0.2310	8.2202
	min	dlc1.3	1.35	-0.2986	-0.1720	0.7261	0.3446	3.9233	-4.3384	-0.4918	5.8492
$F_y$	max	dlc1.3	1.35	0.0371	0.8741	0.5745	0.8748	-13.2607	0.4291	0.2404	13.2677
	min	dlc1.3	1.35	0.0376	-0.6597	0.7932	0.6607	10.6766	1.0697	0.0164	10.7301
$F_z$	max	dlc2.1	1.35	-0.1184	0.3063	1.0834	0.3284	-5.2677	-1.7349	-0.1467	5.5460
	min	dlc6.2	1.1	0.0424	-0.2898	-0.2126	0.2929	3.8073	0.2830	0.0875	3.8178
$F_{\text{res}}$	max	dlc1.3	1.35	0.0371	0.8741	0.5745	0.8748	-13.2607	0.4291	0.2404	13.2677
$M_x$	max	dlc1.3	1.35	0.0669	-0.6405	0.7805	0.6440	11.0224	2.3206	0.3007	11.2641
	min	dlc1.3	1.35	0.0865	0.8012	0.3165	0.8058	-15.5562	1.8017	0.1535	15.6602
$M_y$	max	dlc2.1	1.35	0.2938	-0.4505	0.4212	0.5379	8.3254	5.4230	0.5288	9.9358
	min	dlc1.3	1.35	-0.2922	0.1633	0.6530	0.3347	-2.8828	-4.8319	-0.2283	5.6265
$M_z$	max	dlc2.1	1.35	0.2923	-0.4549	0.4276	0.5407	8.5012	5.3801	0.5395	10.0606
	min	dlc1.3	1.35	-0.2888	-0.2017	0.7415	0.3523	3.8387	-4.6841	-0.5669	6.0561
$M_{\text{res}}$	max	dlc1.3	1.35	0.0865	0.8012	0.3165	0.8058	-15.5562	1.8017	0.1535	15.6602

Table E.18.: Result of extreme load evaluation for section 18 at  $r = 55.8$  m.

	Load case	$\gamma_F$ [-]	$F_x$ [MN]	$F_y$ [MN]	$F_z$ [MN]	$F_{\text{res}}$ [MN]	$M_x$ [MNm]	$M_y$ [MNm]	$M_z$ [MNm]	$M_{\text{res}}$ [Nm]	
$F_x$	max	dlc2.1	1.35	0.2627	-0.2982	0.4680	0.3974	4.5192	3.4497	0.2072	5.6854
	min	dlc1.3	1.35	-0.2444	-0.1892	0.5527	0.3091	2.8518	-3.0506	-0.4447	4.1760
$F_y$	max	dlc1.3	1.35	0.0646	0.7365	0.3099	0.7393	-10.2749	0.7975	0.1454	10.3058
	min	dlc1.3	1.35	0.0687	-0.5906	0.5684	0.5946	7.3442	1.4762	0.2054	7.4911
$F_z$	max	dlc2.1	1.35	-0.0909	0.2589	0.8256	0.2744	-3.4198	-1.1083	-0.1047	3.5949
	min	dlc6.2	1.1	0.0259	-0.3676	-0.1649	0.3685	5.6974	0.4098	0.2279	5.7121
$F_{\text{res}}$	max	dlc1.3	1.35	0.0646	0.7365	0.3099	0.7393	-10.2749	0.7975	0.1454	10.3058
$M_x$	max	dlc1.3	1.35	0.1094	-0.5658	0.5612	0.5763	7.5652	2.2653	0.4175	7.8971
	min	dlc1.3	1.35	0.0877	0.7086	0.2138	0.7140	-10.7707	1.2486	0.1013	10.8428
$M_y$	max	dlc2.1	1.35	0.2452	-0.3870	0.3097	0.4582	5.7949	3.6886	0.4735	6.8693
	min	dlc2.1	1.35	-0.1747	0.1397	0.5072	0.2237	-1.5493	-3.2683	-0.1680	3.6170
$M_z$	max	dlc2.1	1.35	0.2243	-0.4409	0.4857	0.4946	6.1396	3.4203	0.4849	7.0280
	min	dlc1.3	1.35	-0.2422	-0.1983	0.5576	0.3130	2.7637	-3.0671	-0.4588	4.1286
$M_{\text{res}}$	max	dlc1.3	1.35	0.0877	0.7086	0.2138	0.7140	-10.7707	1.2486	0.1013	10.8428

Table E.19.: Result of extreme load evaluation for section 19 at  $r = 62.2$  m.

	Load case	$\gamma_F$ [-]	$F_x$ [MN]	$F_y$ [MN]	$F_z$ [MN]	$F_{\text{res}}$ [MN]	$M_x$ [MNm]	$M_y$ [MNm]	$M_z$ [MNm]	$M_{\text{res}}$ [Nm]	
$F_x$	max	dlc2.1	1.35	0.1978	-0.3275	0.1864	0.3827	3.8871	2.3953	0.2570	4.5658
	min	dlc1.3	1.35	-0.1874	-0.1712	0.3661	0.2539	1.9349	-1.8732	-0.2827	2.6931
$F_y$	max	dlc1.3	1.35	0.0536	0.5952	0.1767	0.5976	-6.5603	0.5270	0.1076	6.5814
	min	dlc1.3	1.35	0.0870	-0.4849	0.3464	0.4927	4.8880	1.3088	0.1688	5.0602
$F_z$	max	dlc2.1	1.35	-0.0576	0.1990	0.5545	0.2072	-2.1371	-0.4957	-0.0997	2.1939
	min	dlc6.2	1.1	0.0248	-0.2734	-0.1250	0.2745	3.4791	0.3534	0.1554	3.4970
$F_{\text{res}}$	max	dlc1.3	1.35	0.0536	0.5952	0.1767	0.5976	-6.5603	0.5270	0.1076	6.5814
$M_x$	max	dlc1.3	1.35	0.1218	-0.4738	0.3365	0.4892	5.0910	1.7618	0.2744	5.3872
	min	dlc1.3	1.35	0.0525	0.5806	0.1546	0.5829	-7.1578	0.6765	0.0776	7.1897
$M_y$	max	dlc1.3	1.35	0.1910	-0.0860	0.3443	0.2094	1.0163	2.4151	0.0650	2.6202
	min	dlc2.1	1.35	-0.1637	0.0844	0.3416	0.1842	-0.8862	-2.2574	-0.1452	2.4251
$M_z$	max	dlc6.2	1.1	0.1355	-0.2638	-0.0226	0.2965	2.8237	1.6068	0.2781	3.2488
	min	dlc2.1	1.35	-0.1636	-0.1294	0.3522	0.2086	1.2549	-2.1723	-0.3174	2.5087
$M_{\text{res}}$	max	dlc1.3	1.35	0.0525	0.5806	0.1546	0.5829	-7.1578	0.6765	0.0776	7.1897

Table E.20.: Result of extreme load evaluation for section 20 at  $r = 68.6$  m.

	Load case	$\gamma_F$ [-]	$F_x$ [MN]	$F_y$ [MN]	$F_z$ [MN]	$F_{\text{res}}$ [MN]	$M_x$ [MNm]	$M_y$ [MNm]	$M_z$ [MNm]	$M_{\text{res}}$ [Nm]
$F_x$ max	dlc1.3	1.35	0.1462	-0.0788	0.2204	0.1661	0.5723	1.3516	0.0316	1.4678
	min	dlc2.1	1.35	-0.1382	0.0490	0.2229	0.1466	-0.4272	-1.3196	-0.0968
$F_y$ max	dlc1.3	1.35	0.0454	0.4403	0.0799	0.4426	-3.9541	0.4076	0.0434	3.9751
	min	dlc1.3	1.35	0.0832	-0.3484	0.2048	0.3582	2.6882	0.8820	0.1333
$F_z$ max	dlc2.1	1.35	-0.0352	0.1378	0.3583	0.1423	-1.0832	-0.2327	-0.0693	1.1079
	min	dlc6.2	1.1	0.0318	-0.1926	-0.0888	0.1952	1.9665	0.2915	0.1084
$F_{\text{res}}$ max	dlc1.3	1.35	0.0454	0.4403	0.0799	0.4426	-3.9541	0.4076	0.0434	3.9751
$M_x$ max	dlc1.3	1.35	0.0991	-0.3271	0.1893	0.3418	2.9243	1.0280	0.1536	3.0997
	min	dlc1.3	1.35	0.0325	0.4035	0.0722	0.4048	-4.1252	0.4590	0.0321
$M_y$ max	dlc1.3	1.35	0.1462	-0.0788	0.2204	0.1661	0.5723	1.3516	0.0316	1.4678
	min	dlc2.1	1.35	-0.1357	0.0662	0.1958	0.1509	-0.5914	-1.3478	-0.0825
$M_z$ max	dlc1.3	1.35	0.1010	-0.3365	0.1935	0.3513	2.8707	1.0608	0.1735	3.0604
	min	dlc2.1	1.35	-0.1379	-0.0938	0.2204	0.1668	0.7267	-1.2590	-0.2112
$M_{\text{res}}$ max	dlc1.3	1.35	0.0325	0.4035	0.0722	0.4048	-4.1252	0.4590	0.0321	4.1507

Table E.21.: Result of extreme load evaluation for section 21 at  $r = 75$  m.

	Load case	$\gamma_F$ [-]	$F_x$ [MN]	$F_y$ [MN]	$F_z$ [MN]	$F_{\text{res}}$ [MN]	$M_x$ [MNm]	$M_y$ [MNm]	$M_z$ [MNm]	$M_{\text{res}}$ [Nm]
$F_x$	max	dlc1.3	1.35	0.0948	-0.0502	0.1220	0.1072	0.2151	0.5777	0.0098
	min	dlc2.1	1.35	-0.0971	0.0399	0.1095	0.1050	-0.2282	-0.6049	-0.0409
$F_y$	max	dlc1.3	1.35	0.0338	0.2946	0.0175	0.2965	-1.9123	0.2556	0.0107
	min	dlc1.3	1.35	0.0702	-0.2251	0.0846	0.2358	1.3145	0.4811	0.0888
$F_z$	max	dlc2.1	1.35	-0.0182	0.0804	0.1998	0.0825	-0.3943	-0.0852	-0.0390
	min	dlc6.2	1.1	0.0240	-0.1251	-0.0574	0.1274	0.8789	0.1332	0.0574
$F_{\text{res}}$	max	dlc1.3	1.35	0.0338	0.2946	0.0175	0.2965	-1.9123	0.2556	0.0107
$M_x$	max	dlc1.3	1.35	0.0589	-0.2223	0.0800	0.2300	1.3665	0.4316	0.0754
	min	dlc1.3	1.35	0.0338	0.2946	0.0175	0.2965	-1.9123	0.2556	0.0107
$M_y$	max	dlc1.3	1.35	0.0944	-0.0486	0.1192	0.1062	0.2207	0.5806	0.0103
	min	dlc2.1	1.35	-0.0971	0.0399	0.1095	0.1050	-0.2282	-0.6049	-0.0409
$M_z$	max	dlc1.3	1.35	0.0708	-0.2242	0.0881	0.2351	1.2730	0.4822	0.0940
	min	dlc2.1	1.35	-0.0947	-0.0645	0.1168	0.1146	0.3271	-0.5430	-0.1176
$M_{\text{res}}$	max	dlc1.3	1.35	0.0338	0.2946	0.0175	0.2965	-1.9123	0.2556	0.0107
										1.9293

Table E.22.: Result of extreme load evaluation for section 22 at  $r = 81.8$  m.

	Load case	$\gamma_F$ [-]	$F_x$ [MN]	$F_y$ [MN]	$F_z$ [MN]	$F_{\text{res}}$ [MN]	$M_x$ [MNm]	$M_y$ [MNm]	$M_z$ [MNm]	$M_{\text{res}}$ [Nm]	
$F_x$	max	dlc1.3	1.35	0.0396	0.1339	-0.0094	0.1396	-0.4392	0.1330	0.0138	0.4589
	min	dlc2.1	1.35	-0.0425	0.0145	0.0354	0.0449	-0.0457	-0.1287	-0.0159	0.1366
$F_y$	max	dlc1.3	1.35	0.0222	0.1482	-0.0135	0.1499	-0.4870	0.0850	0.0135	0.4944
	min	dlc1.3	1.35	0.0315	-0.1143	0.0066	0.1186	0.3683	0.1184	0.0066	0.3868
$F_z$	max	dlc2.1	1.35	-0.0063	0.0282	0.0656	0.0289	-0.0717	-0.0133	-0.0157	0.0730
	min	dlc6.2	1.1	0.0127	-0.0570	-0.0260	0.0584	0.2039	0.0398	0.0146	0.2077
$F_{\text{res}}$	max	dlc1.3	1.35	0.0222	0.1482	-0.0135	0.1499	-0.4870	0.0850	0.0135	0.4944
$M_x$	max	dlc1.3	1.35	0.0315	-0.1143	0.0066	0.1186	0.3683	0.1184	0.0066	0.3868
	min	dlc1.3	1.35	0.0230	0.1471	-0.0115	0.1489	-0.4880	0.0875	0.0144	0.4958
$M_y$	max	dlc1.3	1.35	0.0395	0.1350	-0.0105	0.1407	-0.4449	0.1339	0.0153	0.4646
	min	dlc2.1	1.35	-0.0424	0.0390	0.0400	0.0576	-0.1213	-0.1301	-0.0008	0.1779
$M_z$	max	dlc6.2	1.1	0.0281	-0.0074	-0.0062	0.0290	0.0467	0.1036	0.0255	0.1136
	min	dlc2.1	1.35	-0.0238	-0.0620	0.0336	0.0664	0.1860	-0.0608	-0.0376	0.1957
$M_{\text{res}}$	max	dlc1.3	1.35	0.0230	0.1471	-0.0115	0.1489	-0.4880	0.0875	0.0144	0.4958

Table E.23.: Result of extreme load evaluation for section 23 at  $r = 83.3$  m.

	Load case	$\gamma_F$ [-]	$F_x$ [MN]	$F_y$ [MN]	$F_z$ [MN]	$F_{\text{res}}$ [MN]	$M_x$ [MNm]	$M_y$ [MNm]	$M_z$ [MNm]	$M_{\text{res}}$ [Nm]
$F_x$	max	dlc1.3	1.35	0.0293	0.1028	-0.0114	0.1069	-0.2672	0.0802	0.0127
	min	dlc2.1	1.35	-0.0312	0.0290	0.0268	0.0426	-0.0715	-0.0764	-0.0005
$F_y$	max	dlc1.3	1.35	0.0170	0.1123	-0.0143	0.1136	-0.2919	0.0515	0.0114
	min	dlc1.3	1.35	0.0248	-0.0885	-0.0008	0.0919	0.2241	0.0735	0.0005
$F_z$	max	dlc2.1	1.35	-0.0043	0.0190	0.0441	0.0195	-0.0393	-0.0073	-0.0113
	min	dlc6.2	1.1	0.0098	-0.0427	-0.0195	0.0438	0.1218	0.0241	0.0086
$F_{\text{res}}$	max	dlc1.3	1.35	0.0175	0.1122	-0.0138	0.1136	-0.2915	0.0531	0.0113
$M_x$	max	dlc1.3	1.35	0.0248	-0.0885	-0.0008	0.0919	0.2241	0.0735	0.0005
	min	dlc1.3	1.35	0.0186	0.1113	-0.0115	0.1129	-0.2946	0.0564	0.0115
$M_y$	max	dlc1.3	1.35	0.0291	-0.0662	0.0103	0.0723	0.1655	0.0816	0.0013
	min	dlc2.1	1.35	-0.0312	0.0290	0.0268	0.0426	-0.0715	-0.0764	-0.0005
$M_z$	max	dlc1.3	1.35	0.0022	0.0925	0.0001	0.0925	-0.2333	0.0095	0.0176
	min	dlc2.1	1.35	-0.0172	-0.0474	0.0210	0.0504	0.1126	-0.0340	-0.0262
$M_{\text{res}}$	max	dlc1.3	1.35	0.0186	0.1113	-0.0115	0.1129	-0.2946	0.0564	0.0115

Table E.24.: Result of extreme load evaluation for section 24 at  $r = 84.8$  m.

	Load case	$\gamma_F$ [-]	$F_x$ [MN]	$F_y$ [MN]	$F_z$ [MN]	$F_{\text{res}}$ [MN]	$M_x$ [MNm]	$M_y$ [MNm]	$M_z$ [MNm]	$M_{\text{res}}$ [Nm]
$F_x$ max	dlc1.3	1.35	0.0202	-0.0472	0.0048	0.0513	0.0861	0.0431	-0.0024	0.0962
	min	dlc2.1	1.35	-0.0208	0.0197	0.0171	0.0287	-0.0358	-0.0386	0.0001
$F_y$ max	dlc1.3	1.35	0.0133	0.0782	-0.0098	0.0793	-0.1521	0.0304	0.0092	0.1551
	min	dlc1.3	1.35	0.0175	-0.0624	-0.0034	0.0648	0.1156	0.0397	-0.0033
$F_z$ max	dlc2.1	1.35	-0.0028	0.0116	0.0283	0.0119	-0.0179	-0.0037	-0.0073	0.0182
	min	dlc6.2	1.1	0.0069	-0.0293	-0.0134	0.0301	0.0625	0.0125	0.0039
$F_{\text{res}}$ max	dlc1.3	1.35	0.0133	0.0782	-0.0098	0.0793	-0.1521	0.0304	0.0092	0.1551
$M_x$ max	dlc1.3	1.35	0.0177	-0.0624	-0.0034	0.0648	0.1157	0.0400	-0.0038	0.1224
	min	dlc1.3	1.35	0.0133	0.0782	-0.0098	0.0793	-0.1521	0.0304	0.0092
$M_y$ max	dlc1.3	1.35	0.0202	-0.0472	0.0048	0.0513	0.0861	0.0431	-0.0024	0.0962
	min	dlc2.1	1.35	-0.0208	0.0197	0.0171	0.0287	-0.0358	-0.0386	0.0001
$M_z$ max	dlc1.3	1.35	0.0013	0.0638	-0.0013	0.0638	-0.1186	0.0052	0.0121	0.1187
	min	dlc1.3	1.35	-0.0026	-0.0210	0.0154	0.0211	0.0334	-0.0023	-0.0172
$M_{\text{res}}$ max	dlc1.3	1.35	0.0133	0.0782	-0.0098	0.0793	-0.1521	0.0304	0.0092	0.1551

Table E.25.: Result of extreme load evaluation for section 25 at  $r = 86.3$  m.

	Load case	$\gamma_F$ [-]	$F_x$ [MN]	$F_y$ [MN]	$F_z$ [MN]	$F_{\text{res}}$ [MN]	$M_x$ [MNm]	$M_y$ [MNm]	$M_z$ [MNm]	$M_{\text{res}}$ [Nm]	
$F_x$	max	dlc1.3	1.35	0.0119	-0.0285	0.0010	0.0308	0.0336	0.0173	-0.0040	0.0378
	min	dlc2.1	1.35	-0.0117	0.0163	0.0066	0.0201	-0.0182	-0.0150	0.0022	0.0235
$F_y$	max	dlc1.3	1.35	0.0087	0.0467	-0.0056	0.0475	-0.0598	0.0133	0.0059	0.0613
	min	dlc1.3	1.35	0.0105	-0.0371	-0.0040	0.0386	0.0452	0.0166	-0.0051	0.0481
$F_z$	max	dlc2.1	1.35	-0.0015	0.0058	0.0148	0.0059	-0.0062	-0.0016	-0.0038	0.0064
	min	dlc1.3	1.35	0.0064	0.0453	-0.0081	0.0457	-0.0579	0.0109	0.0070	0.0589
$F_{\text{res}}$	max	dlc1.3	1.35	0.0087	0.0467	-0.0056	0.0475	-0.0598	0.0133	0.0059	0.0613
$M_x$	max	dlc1.3	1.35	0.0105	-0.0371	-0.0040	0.0386	0.0452	0.0166	-0.0051	0.0481
	min	dlc1.3	1.35	0.0087	0.0467	-0.0056	0.0475	-0.0598	0.0133	0.0059	0.0613
$M_y$	max	dlc2.1	1.35	0.0118	-0.0274	-0.0001	0.0298	0.0329	0.0174	-0.0035	0.0372
	min	dlc2.1	1.35	-0.0117	0.0163	0.0066	0.0201	-0.0182	-0.0150	0.0022	0.0235
$M_z$	max	dlc2.1	1.35	0.0088	0.0437	-0.0048	0.0445	-0.0546	0.0137	0.0080	0.0563
	min	dlc1.3	1.35	-0.0016	-0.0116	0.0078	0.0118	0.0116	-0.0011	-0.0093	0.0116
$M_{\text{res}}$	max	dlc1.3	1.35	0.0087	0.0467	-0.0056	0.0475	-0.0598	0.0133	0.0059	0.0613

Table E.26.: Result of extreme load evaluation for section 26 at  $r = 87.8$  m.

	Load case	$\gamma_F$ [-]	$F_x$ [MN]	$F_y$ [MN]	$F_z$ [MN]	$F_{\text{res}}$ [MN]	$M_x$ [MNm]	$M_y$ [MNm]	$M_z$ [MNm]	$M_{\text{res}}$ [Nm]	
$F_x$	max	dlc2.1	1.35	0.0047	-0.0110	-0.0005	0.0120	0.0062	0.0038	-0.0022	0.0073
	min	dlc2.1	1.35	-0.0045	0.0057	0.0026	0.0073	-0.0031	-0.0031	0.0006	0.0043
$F_y$	max	dlc1.3	1.35	0.0034	0.0187	-0.0026	0.0190	-0.0114	0.0030	0.0028	0.0117
	min	dlc1.3	1.35	0.0028	-0.0146	-0.0008	0.0149	0.0084	0.0028	-0.0030	0.0088
$F_z$	max	dlc2.1	1.35	-0.0005	0.0018	0.0055	0.0019	-0.0010	-0.0005	-0.0013	0.0011
	min	dlc1.3	1.35	0.0025	0.0178	-0.0035	0.0180	-0.0108	0.0026	0.0031	0.0111
$F_{\text{res}}$	max	dlc1.3	1.35	0.0034	0.0187	-0.0026	0.0190	-0.0114	0.0030	0.0028	0.0117
$M_x$	max	dlc6.2	1.1	0.0017	-0.0119	-0.0034	0.0120	0.0086	0.0013	-0.0001	0.0086
	min	dlc1.3	1.35	0.0034	0.0187	-0.0026	0.0190	-0.0114	0.0030	0.0028	0.0117
$M_y$	max	dlc2.1	1.35	0.0047	-0.0110	-0.0005	0.0120	0.0062	0.0038	-0.0022	0.0073
	min	dlc2.1	1.35	-0.0045	0.0043	0.0033	0.0062	-0.0024	-0.0031	0.0002	0.0039
$M_z$	max	dlc1.3	1.35	0.0032	0.0179	-0.0014	0.0182	-0.0105	0.0027	0.0035	0.0109
	min	dlc1.3	1.35	0.0023	-0.0133	0.0009	0.0135	0.0073	0.0024	-0.0036	0.0076
$M_{\text{res}}$	max	dlc1.3	1.35	0.0034	0.0187	-0.0026	0.0190	-0.0114	0.0030	0.0028	0.0117

Table E.27.: Result of extreme load evaluation for section 27 at  $r = 89.136$  m.

	Load case	$\gamma_F$ [-]	$F_x$ [MN]	$F_y$ [MN]	$F_z$ [MN]	$F_{\text{res}}$ [MN]	$M_x$ [MNm]	$M_y$ [MNm]	$M_z$ [MNm]	$M_{\text{res}}$ [Nm]
$F_x$	max	dlc2.1	1.35	0.0000	-0.0000	0.0001	0.0000	-0.0000	-0.0000	0.0000
	min	dlc1.3	1.35	-0.0000	0.0000	0.0002	0.0001	0.0000	0.0000	0.0000
$F_y$	max	dlc1.3	1.35	-0.0000	0.0000	0.0001	0.0000	0.0000	0.0000	0.0000
	min	dlc1.3	1.35	0.0000	-0.0000	0.0001	0.0000	-0.0000	0.0000	-0.0000
$F_z$	max	dlc1.3	1.35	-0.0000	0.0000	0.0002	0.0000	0.0000	0.0000	0.0000
	min	dlc6.3	1.35	0.0000	-0.0000	-0.0000	0.0000	-0.0000	-0.0000	0.0000
$F_{\text{res}}$	max	dlc1.3	1.35	-0.0000	0.0000	0.0002	0.0001	0.0000	0.0000	0.0000
$M_x$	max	dlc1.3	1.35	-0.0000	0.0000	0.0001	0.0001	0.0000	0.0000	0.0000
	min	dlc1.3	1.35	0.0000	-0.0000	0.0001	0.0000	-0.0000	0.0000	-0.0000
$M_y$	max	dlc1.3	1.35	-0.0000	0.0000	0.0002	0.0001	0.0000	0.0000	0.0000
	min	dlc6.2	1.1	0.0000	-0.0000	0.0000	0.0000	-0.0000	-0.0000	-0.0000
$M_z$	max	dlc1.3	1.35	-0.0000	0.0000	0.0002	0.0001	0.0000	0.0000	0.0000
	min	dlc1.3	1.35	-0.0000	-0.0000	0.0000	0.0000	-0.0000	0.0000	-0.0000
$M_{\text{res}}$	max	dlc1.3	1.35	-0.0000	0.0000	0.0002	0.0001	0.0000	0.0000	0.0000